LIFE-CYCLE ESTIMATES OF STRUCTURES SUBJECTED TO SEISMIC LOADS

A Dissertation

Presented to the Faculty of the Graduate School

of Cornell University

in Partial Fulfillment of the Requirements for the Degree of

Doctor of Philosophy

by

Alin Constantin Radu

January 2015

LIFE-CYCLE ESTIMATES OF STRUCTURES SUBJECTED TO SEISMIC LOADS

Alin Constantin Radu, Ph.D.

Cornell University 2015

The overall objective of the current research is the development of a computationally efficient, conceptually simple, easy-to-use method providing loss estimates and other performance metrics for structural systems subjected to seismic loads. The method is based on (1) a novel probabilistic site-specific seismological model, (2) an efficient algorithm for calculating response statistics and (3) probabilistic models for life-cycle structural performance.

The proposed seismic-hazard model uses earthquake records at the site of interest and the specific barrier seismological model to provide a more realistic representation of site seismic hazard. The information provided by records and the specific barrier model is aggregated in a Bayesian framework and used subsequently to simulate ground-motion samples as a function of the moment magnitude m and source-to-site distance r. Structural response statistics to simulated ground acceleration records are obtained by a novel efficient, non-intrusive method that resembles the Monte Carlo approach. Like Monte-Carlo, the method calculates structural responses to samples of the ground-motion process. Unlike Monte-Carlo, which uses a large number of samples selected at random, the proposed method uses a small number of samples selected in an optimal way. The efficiency of the proposed method allows calculation of distributions, rather than just mean values, for downtime cost, damage, and other metrics. Probability distributions can be used in insurance applications to

calculate premiums to cover cost of damage. They are also essential tools for assessing tail risk, a quantity which accounts for low-probability events with high impact, used for transferring risk to reinsurance markets. These capabilities are particularly important when dealing with extreme events. Numerical results are presented for linear and non-linear systems. Life-cycle scenarios for seismic events are simulated and used to estimate life-cycle cost and damage.

BIOGRAPHICAL SKETCH

Alin Radu hails from Braila, Romania, where he lived until the age of nineteen. After a one-year stint as an Erasmus exchange scholar in England, he completed his undergraduate education at the Technical University of Civil Engineering in Bucharest, in 2009. He then went on to earn his M.Sc. degree in Analysis and Design of Structures for Hazards at the City University in London, UK, in 2010. At the end of that year, Alin began his doctoral studies in structural engineering, at Cornell University, under the supervision of Professor Mircea Grigoriu. He has recently accepted a job offer from AIR Worldwide in San Francisco, California. AIR is a leader in the field of risk modeling for natural and man-made catastrophes. Alin will begin his professional career as a research engineer in September 2014.

To my mother Aureliana and my father Constantin

ACKNOWLEDGEMENTS

I could not have completed my doctoral studies without the support of many faculty members at Cornell, friends and family. First of all, I would like to thank Professor Mircea Grigoriu for his unconditional support and patience. Not only has he provided me with remarkable technical and theoretical advice, but he has also become my mentor and friend, guiding me in the search for a career path in the years to come. I would also like to thank my other committee members Dr. Chris Earls, Dr. Sidney Resnick and Dr. Derek Warner for their remarks and suggestions regarding my research. Lastly, thanks are due to Dr. Cagdas Kafali and Dr. Rowena Lohman for their helpful and insightful comments on my work.

Special thanks go to Sepehr Saroukhani with whom I shared my office during the toughest and longest year of my doctoral studies and to Haoran Zhao for bearing with me during stressful days during my last couple of years at Cornell. I would also like to thank my Dynamics TA and officemate Dr. Changhoon Lee for teaching me many useful things and for his continuous technical support and patience.

My life outside the office wouldn't have been as fun without the friends who have accompanied me throughout my career at Cornell. I would like to thank Patty Chuang and Dr. Geoffrey Bomarito for hosting many game nights and for countless happy moments shared on campus. I would also like to extend special thanks to my very good friend Matt Higgins for introducing me to the American life and for sharing long work hours in Hollister, and to my housemate, neighbor and exceptional friend David Israelachvili for cheering me up every day, for the endless, and often, pointless conversations, for daily English lessons and many fun moments at Cornell. And the list of friends could go on

and on with many names, among which I will mention a few: Alexander, Cathy, Christina, Cristina, Ishan, Jacqueline, Jeffrey, Nick, Qing etc.

Finally, I would like to extend many thanks to my parents Aureliana and Constantin Radu for their patience and understanding despite the difficulties involved in not seeing one another but for once a year. I am very grateful to my sister Dr. Alexandra Radu and my cousin Mihaela Pologescu for their constant support, care and advice. Most importantly, I would like to send many thanks to my beloved girlfriend Irina Lazar who has encouraged me every day of my doctoral studies, accepted me in my worst moments and made our Ithaca summers unforgettable.

My work was financially supported primarily by the National Science Foundation under NSF Award Number CMMI-0925714. This support is gratefully acknowledged.

TABLE OF CONTENTS

LIST OF TABLES

LIST OF FIGURES

CHAPTER 1

INTRODUCTION

Performance-based seismic design philosophy provides a rational balance between, safety, economy and functionality, by explicitly considering performance objectives which define acceptable damage levels for a structural system subjected to earthquakes of specified intensities. Designs based on a single performance criteria could lead to unsatisfactory results. For example, if the objective of the design is safety alone, then the functionality requirements might not be fulfilled and the economic interests of the owner might not be served. If the design objective is the structure remaining operational irrespective of the ground motion intensity, the resulting design might be costly and unacceptable for most structural system.

Practical implementation of performance-based seismic design can be achieved by reaching four main objectives: (1) development of novel probabilistic models for site-specific seismic hazard based on all available information and capable of capturing accurately essential features of seismic loads; (2) development of highly efficient, non-intrusive, accurate and conceptually simple methods for calculating response statistics for linear and non-linear structural systems subjected to seismic loads consistent with the hazard models; (3) critical overview and improvement of current methods used in earthquake engineering in vulnerability analyses and (4) estimation of probability distributions, rather than only mean values, for response, life-cycle damage, cost, downtime and other performance measures. This study aims to provide new methodologies to reach these goals and show improvements of the current practice in probabilistic seismic hazard analysis. The current work is structured in four chapters,

which treat the four objectives set to reach the goal of this study.

Chapter 2, *A site-specific seismological model for probabilistic seismic hazard assessment*, develops a seismological model which provides a more realistic characterization of site seismic hazard. The proposed model is a statistical update of a seismological model based on the specific barrier model with actual ground-motion site records. The information provided by records and the specific barrier model are aggregated in a Bayesian framework and used subsequently to simulate ground-motion samples as a function of the moment magnitude m and source-to-site distance r.

Chapter 3, *Stochastic reduced order models (SROM)*, proposes a novel, conceptually-simple, computationally-efficient method, as an alternative to Monte Carlo. Like Monte-Carlo, stochastic reduced order models are constructed using random samples of the ground motion process, but which are selected in an optimal way and are not equally likely. The construction of the SROM involves two main steps. First, a range of ground motion samples is selected based on some heuristic arguments. Secondly, probabilities of the selected records are obtained by solving an optimization problem. The SROMs are used to calculate accurately response statistics for linear and non-linear structural systems subjected to seismic ground-motion samples. The performance of the stochastic reduced order models is shown to be remarkable.

Chapter 4, *Limitations of current approaches and improvements*, discusses the limitations of current intensity measures and methods used in earthquake engineering. Spectral values and peak ground acceleration are commonly used as intensity measures of seismic ground motions in fragility-curves calculations. It is shown that scalar intensity measures may lead to unsatisfactory results, when

they are used to characterize ground motions. Fragility curves are probabilities that responses of structures exceed specified critical limits when subjected to earthquakes of given intensity measures. Since fragility curves are popular elements used in performance-based seismic design, a new method for calculating fragility curves is proposed. The new method is based on selecting sets of ground motion records from large datasets by using stochastic reduced order models.

Chapter 5, *Structural performance by fragility surface for simple systems under non-Gaussian input*, proposes a vector-valued intensity measure with components moment magnitude m and source-to-site distance r to characterize seismic ground motions. Fragility surfaces represent probability that the structural response exceeds a limit state when subjected to an earthquake with (m, r). Fragility surfaces are proposed to characterize the seismic performance of structures, as alternatives to fragility curves. Fragility surfaces are based on response analyses and may be computationally expensive. Therefore, SROMs are proposed as an efficient and accurate method to calculate fragility surfaces. A framework for calculating probability distribution functions for life-cycle estimates of structures subjected to seismic loading is proposed. Several metrics which can evaluate the seismic-performance of structures are calculated based on heuristic cost and damage models.

CHAPTER 2

A SITE-SPECIFIC SEISMOLOGICAL MODEL FOR PROBABILISTIC SEISMIC HAZARD ASSESSMENT

2.1 Introduction

Earthquakes can have a catastrophic impact on human lives, economy and environment. The main goal of earthquake engineering is the development of structures that experience limited damage under moderate seismic events and do not collapse under large events. To achieve this goal, the input characterized by the seismic ground-accelerations, needs to be characterized accurately, particularly when dealing with large events. Such a characterization cannot be obtained solely from data due to the small number of large seismic records at individual sites. Three options are available to enrich the set of records at a site: (1) use data from sites similar to that of interest and scale them to desired intensities (data-based seismic hazard), (2) calibrate probabilistic models for the ground acceleration process to actual records available at a site and view the samples of these models as likely ground accelerations (probability-based seismic hazard), and (3) use the information from site seismic records to calibrate seismological models based on geophysical considerations (physics-based seismic hazard). A comprehensive classification of the seismological models in the literature is presented in [16].

Data-based seismic hazard. Douglas [15] used empirical arguments to select ground-acceleration records. It is popular to select ground-motion records to match a response target acceleration spectrum conditional on the spectral acceleration amplitude at a period of interest [5]. Computational methods for

the conditional spectrum were described in [52] and an efficient selection algorithm was proposed in [42]. A similar approach is introduced in [54], in which a methodology was proposed to select records from a database by matching a target spectral displacement value. The selected seismic records were then scaled to obtain ground motions of various intensities. This procedure is of questionable value since it only changes the amplitude of the motion, but not its frequency content [30, 44].

Probability-based seismic hazard. Postulated mathematical models are calibrated to actual records and used to produce artificial records. For example, Zentner and Poirion [76] developed a model to produce ground-acceleration samples using the Karhunen-Loève (K-L) expansion. They estimated the marginal distribution and the second-order properties of the random variables in the K-L expansion using seismic records. Even though this model can be used to produce any number of records, the K-L expansion captures only the second moment properties of the seismic ground-acceleration records used in the calibration. [58] used other models for ground-acceleration simulation. They assumed a log-normal distribution for the P and S pulses in the time domain to model the non-stationary character and use empirical ground motion prediction models to produce a realistic Fourier spectrum for the frequency content of the ground-acceleration process. In a related approach [65], artificial records are used to enrich the existent ground-acceleration records database. They produced synthetic seismic records to enrich the dataset of ground motion records selected empirically from a global dataset. Records selected from large datasets, as done in [5] and [54] may not necessarily be representative for a particular site.

Physics-based seismic hazard. Physical models incorporating seismological

characteristics of earthquakes are calibrated to ground-acceleration records usually obtained over broad regions. The specific barrier model (SBM) [55, 56] is a seismic-source model, which has been calibrated to regional data, e.g. Eastern U.S., and was put forward as part of a seismological model in [37]. The SBM's calibration to the NGA dataset was further confirmed in [18]. The seismological model with SBM describes the frequency content of ground motions and its scaling with magnitude, source-to-site distance and site classification. The model delivers information about the frequency content of the ground motion in the form of a power spectral density function. The model with SBM provides generic site amplification functions for rock and soil sites and does not capture detailed seismic properties at particular sites. A recent study introduces a more general form of the SBM, which shows how to incorporate additional source characteristics in the model [38, 39].

The main goal of this chapter is to develop a seismological model which can produce any number of ground-motion samples that are consistent with seismological models and the records at a site. We will use all the available information, that is, a seismological model to account for the physics in the seismic phenomenon, and available records at a specified site to capture features of ground accelerations specific to that site. This information will be aggregated in a Bayesian framework. The site data consists of all site earthquake-records and earthquake statistics. The seismological model used is built on the basis of the SBM [37]. The model is statistically updated by using site-specific seismic records. Our previous efforts to update the model were presented in [59, 60]. The newly proposed model is used to calculate statistics for intensity measures, such as the peak ground acceleration and the spectral response accelerations, and generate synthetic records by employing Monte Carlo simulations.

2.2 Site Data

Site data used for the statistical update of the seismological model consists of earthquake records and earthquake statistics at the site of interest. Records at a site are obtained from the Incorporated Research Institutions for Seismology (IRIS), which provides time series of earthquakes recorded at stations located throughout the United States.

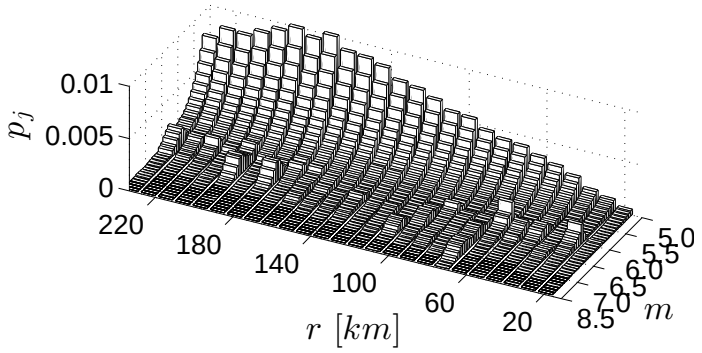

Figure 2.1: Seismic activity matrix for the USC in Los Angeles.

The United States Geological Survey (USGS) provides the mean annual rate of earthquake occurrence for every zip code in the United States. The rates λ_j are calculated as a function of the vector $(m, r)_j$ for a specified range of m. They are obtained by using various models that account for the uncertainty in the seismic sources [19] and consider all seismic sources in a circular area of radius $\mathcal{R}$ centered at the site under consideration. By normalizing these rates, we can construct a two-dimensional histogram, which represents the probabilities of occurrence of earthquakes characterized by $(m, r)_j$, i.e. $p_j = \mathbb{P}[(M, R) = (m, r)_j] = \lambda_j / \sum_i \lambda_i$. This two-dimensional histogram is referred to as the seismic activity matrix. It defines the multinomial probability mass function for the two-dimensional discrete random vector (M, R), where M

is a random variable for the moment magnitude and R is the random variable for the source-to-site distance. We will refer to each point of the matrix with coordinates $(m, r)_j$ as cell j with probability $p_j,\ j = 1, ..., N$, where N is the total number of cells.

2.2.1 Site Data for Numerical Example

University of Southern California (USC) in Los Angeles is chosen as an example to show numerical results for the model proposed. Table 2.1 provides the moment magnitude m and the source-to-site distance r, for all 21 seismic ground motion records available from IRIS at the USC station.

Records 11 and 12, are aftershocks of the main earthquake 10. However, we view them as all the other records in the table, that is, independent samples of the stochastic process describing the seismic ground accelerations at the USC. This assumption is reasonable since each event is initiated in a slightly different location and the seismic waves travel on different paths from the source to the site. The use of earthquakes aftershocks is also common in the development of attenuation models. It has been observed [1] that including the aftershock in the analysis increases the number of low-magnitude events and the variability in the dataset, which, in our case, helps accurately capture site characteristics in the spectral density model.

Figure 2.1 shows the seismic activity matrix for the USC site. We select an area of radius $\mathcal{R} = 240\ km$ to construct the seismic activity matrix, but custom radii can be used depending on the user's need.

Table 2.1: Earthquake Records

Record	m	$r\,[km]$	Lat.	Long.	Date
1	5.2	145	35.15	-119.10	05/28/1993
2	5.0	181	34.03	-116.32	08/21/1993
3	5.0	46	34.38	-118.56	01/18/1994
4	5.3	55	34.38	-118.71	01/19/1994
5	5.4	41	34.31	-118.58	01/29/1994
6	5.3	28	34.23	-118.47	03/20/1994
7	5.0	111	34.19	-117.10	04/06/1994
8	5.3	176	34.27	-116.40	06/16/1994
9	5.0	185	33.90	-116.29	05/07/1995
10	7.1	196	34.59	-116.29	10/16/1999
11	5.8	198	34.68	-116.27	10/16/1999
12	5.7	193	34.44	-116.28	10/16/1999
13	5.0	196	34.86	-116.25	10/22/1999
14	5.3	127	34.29	-116.41	02/10/2001
15	5.1	173	33.51	-116.95	10/31/2001
16	5.2	136	34.31	-116.51	02/22/2003
17	5.1	190	32.22	-117.92	06/15/2004
18	5.1	154	35.39	-116.85	09/29/2004
19	5.5	49	33.95	-117.76	07/29/2008
20	5.1	193	34.81	-116.42	12/06/2008
21	5.5	179	33.42	-116.49	07/07/2010

* Table contains information about the earthquakes recorded at University of Southern California between 1993 and 2010: moment magnitude m, source-to-site distance r, location by geographical coordinates, i.e., latitude and longitude, and date of event.

2.3 Seismological Model

We have selected the SBM-based seismological model [37] to characterize the physics of our model since the SBM is a physically consistent earthquake-source

model that can account for any source complexity and source-site geometry. In addition, the SBM is applicable both in the near-fault and far-field regions. Our objective is to statistically update this seismological model with records available at a particular site.

2.3.1 The Specific Barrier Model

The SBM is a seismic-source model constructed by using physical approaches and has been calibrated to large sets of regional ground acceleration records consistent with certain tectonic characteristics. The SBM, as part of a seismological model [37], gives the power spectral density function $g(f; m, r)$ for the seismic ground acceleration process as a function of frequency f. It depends on the moment magnitude m, the source-to-site distance r and other parameters related to the soil conditions and the type of tectonic region. We consider only dependence on (m, r) which is sufficient when dealing with a single site, if we consider that the soil conditions and tectonic regime are fixed.

The positive one-sided spectral density function as derived from the seismological model with the SBM has the form

$$g(f; m, r) = \frac{1}{2\pi\tau_f}|a(f; m, r)|^2, \ f \geq 0 \tag{2.1}$$

where τ_f is the duration of the earthquake,

$$a(f; m, r) = cS(f; m, \Delta\sigma_L)F(f)Q(f; r)G(f), \tag{2.2}$$

is the Fourier amplitude spectrum, in which c is a scaling factor, $S(f; m)$ is the source spectrum, $F(f)$ is a high-frequency diminution function, $Q(f; r)$ is a wave-path attenuation function and $G(f)$ is a function which accounts for the

site response and local soil properties. Technical details on this seismological model can be found in [55, 56, 37]. We will refer to the spectral density in (2.1) as the SBM spectral density.

2.3.2 Surrogate Model

The SBM spectral density function in (2.1) is available in an algorithmic form and can be calculated for each cell $(m, r)_j,\ j = 1, ..., N$, of the seismic activity matrix. Since our goal is to update statistically this model by using seismic records, we need a parametric model for $g(f; (m, r)_j)$. For simplicity we use the notation $g_j(f) := g(f; (m, r)_j),\ j = 1, ..., N$.

The singular value decomposition method [13] is used to construct a parametric model for $g_j(f)$. The spectral density functions for all cells N are arranged in a matrix G with dimension $n_f \times N$, where n_f is the number of equally spaced discrete frequencies, selected in the frequency range of $g_j(f)$, i.e. $[0, \overline{f}]$ where a cut-off frequency $\overline{f} = 30\ rad/s$ is used. The limit value of $30\ rad/s$ chosen for the range of frequencies is sufficiently large for earthquake engineers' interests, but the spectral density model is not limited to this value. The singular value decomposition of G is

$$G = USV^T = \sum_{k=1}^{d} s_k(u_k v_k^T) \tag{2.3}$$

where U and V are $n_f \times n_f$ and $N \times N$ orthogonal matrices, respectively. Notation V^T stands for the transpose of matrix V. Vectors u_k and v_k are the k-th columns of matrices U and V, respectively. They are called singular vectors of G. Matrix S is a $n_f \times N$ matrix with zero off-diagonal elements. The diagonal elements of S, $s_k = S_{k,k},\ k = 1, ..., d = \min(n_f, N)$ are called the singular values of G.

It is common to arrange s_k in descending order. Each j-th column of G is the spectral density $g_j(f)$ in cell j.

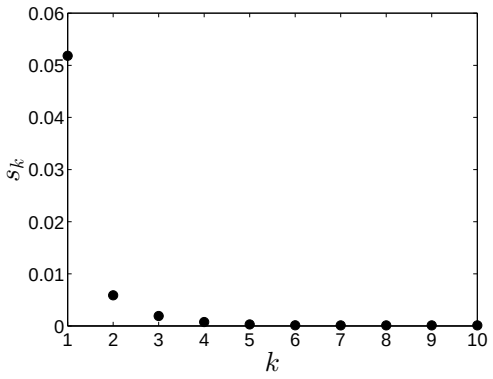

Figure 2.2: Singular values $s_k,\ k = 1, ..., 10$.

Figure 2.2 shows the first ten singular values of G. Since over 90% of the contribution in the spectral density function is concentrated in just the first two singular modes, an approximation of G can be obtained by truncation, i.e., we approximate G by

$$G_0 = \sum_{k=1}^{d_0} s_k(u_k v_k^T), \tag{2.4}$$

where $d_0 < d$. However, G_0 may not be satisfactory for some cells j. For example, the solid and dashed lines in Figure 2.3 are the spectral densities in (2.1) and its approximation in (2.4) with $d_0 = 3$ for cell $(m = 5,\ r = 100\ km)$.

Therefore, we will use all $d = 601$ modes in the representation of $g_j(f)$, so that we have

$$g_j(f) = s_1\phi_{1,j}(f) + s_2\phi_{2,j}(f) + \sum_{k=3}^{d} s_k\phi_{k,j}(f) = \sum_{i=1}^{3} \varphi_{i,j}(f), \tag{2.5}$$

where the k-th singular mode of G in cell j, $\phi_{k,j}(f)$, is the j-th column of the matrix $u_k v_k^T$. The latter equality holds with the notation $\varphi_{i,j}(f) = s_i\phi_{i,j}(f),\ i = 1, 2$

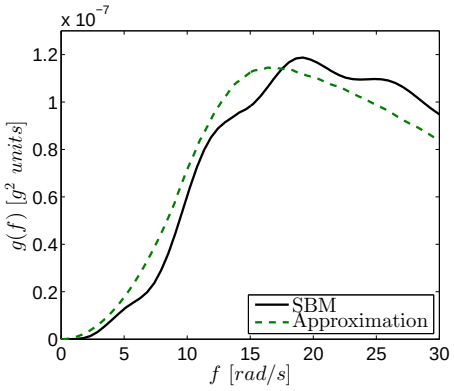

Figure 2.3: Target (solid line) and approximate by the first 3 singular modes (dashed line) power spectral density functions for cells $(m, r)_j = (5, 100\ km)$.

and $\varphi_{3,j}(f) = \sum_{k=3}^{d} s_k \phi_{k,j}(f)$, referred to as basis functions of $g_j(f)$. The basis $\varphi_{3,j}(f)$ is a cumulative function of all the high-order singular modes. The representation in (2.5) is identical with (2.3), but written in a different form to be used in the following development. Figure 2.4 shows the basis functions $\varphi_{i,j}(f),\ i = 1, 2, 3$ for cells $(m, r)_j = (5,\ 100\ km)$ and $(m, r)_j = (8,\ 200\ km)$, respectively. A computer script which delivers the basis functions $\varphi_{i,j}(f)$ is available in the electronic supplement to this article.

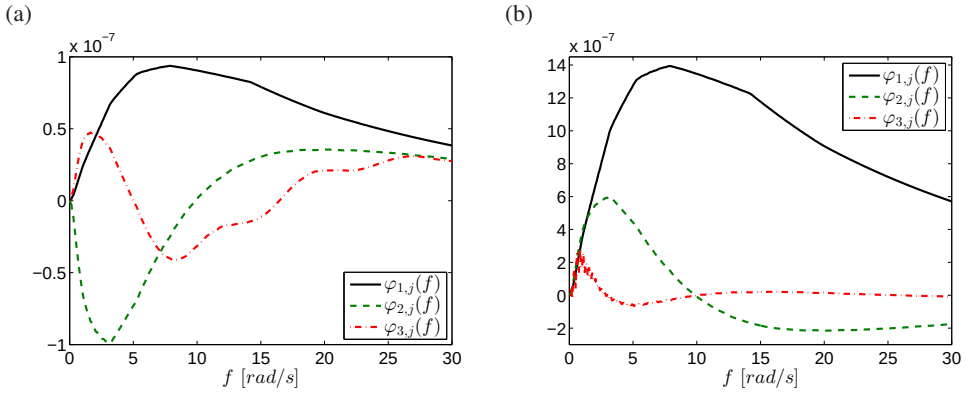

Figure 2.4: Spectral density modes $\varphi_{i,j}(f),\ i = 1, 2, 3$ for (a) $(m = 5, r = 100\ km)$ and (b) $(m = 8, r = 200\ km)$.

2.3.3 Stochastic Surrogate Model

The construction of the stochastic surrogate model involves the following three steps. First, the modes $\varphi_{i,j}(f)$ of the spectral density in (2.5) are weighed by random coefficients $\Theta_i,\ i = 1, 2, 3$. Second, we calibrate the probability distribution of the random coefficients $\Theta_i,\ i = 1, 2, 3$ to ground motion records in a Bayesian framework. Third, the model in (2.6) with posterior distributions of Θ_i, updated with site data, is used to sample spectral densities which capture seismic characteristics at the site of interest.

As previously stated, our objective is to update statistically the spectral density in (2.1) by using records of a single site. To reach this goal, the model in (2.5) is rewritten in the form

$$\tilde{g}_j(f;\Theta) = \sum_{i=1}^{3} \Theta_i \varphi_{i,j}(f), \tag{2.6}$$

where $\{\Theta_i,\ i = 1, 2, 3\}$ are scale factors for the modes in (2.5) and $\tilde{g}_j(f;\Theta)$ is the stochastic version of the surrogate model $g_j(f)$. We assume that $\{\Theta_i,\ i = 1, 2, 3\}$ are independent random variables which must satisfy the following conditions: (a) function $\tilde{g}_j(f;\Theta)$ must be positive, since, by definition, the spectral density is as a Fourier transform of the correlation function [33] and (b) $\tilde{g}_j(f;\Theta)$ should be centered around the spectral density produced by the seismological model with SBM since the proposed model is just a perturbation of the original one due to records at a single site. We select the range Ψ of the random vector $\Theta = [\Theta_1, \Theta_2, \Theta_3]$ to be as large as possible such that: (a) the spectral density function exists, that is, $\tilde{g}_j(f;\theta) \geq 0, \forall f \geq 0,\ \forall j = 1, ..., N$ and $\forall \theta = [\theta_1, \theta_2, \theta_3] \in \Psi$, and (b) the mean of the parametric model in (2.6) is the SBM spectral density, that is, $\mathbb{E}[\tilde{g}_j(f;\Theta)] = g_j(f)$, which holds if $\mathbb{E}[\Theta] = \mathbf{1}$, where $\mathbf{1} = [1, 1, 1]$.

For some cells, the condition (a) is satisfied only if Ψ is a small vicinity of $\mathbf{1}$. For example, in cell $(m,r)_j = (5, 100\ km)$ with the modes shown in the left panel of Figure 2.4, $\sum_{i=2}^{3} \varphi_{i,j}(f) \simeq -\varphi_{1,j}$ at low frequencies. We denote by $\mathcal{C} = \{j : \exists\ f \in [0, f^*]$ s.t. $\sum_{i=1}^{3} \Theta_i \varphi_{i,j}(f) < 0\}$ the set of cells for which $\tilde{g}_j(f;\Theta)$ is negative in a range $[0, f^*]$, with $f^* > 0$ selected to assure a sufficiently large range Ψ. For the cells in $\mathcal{C}$ we modify the representation in (2.6) as follows

$$\tilde{g}_j(f;\Theta) = \mathbb{1}_{\mathcal{C}} \left(\mathbb{1}_{f \leq f^*} \tilde{g}_j^*(f;\Theta) + \mathbb{1}_{f > f^*} \sum_{i=1}^{3} \Theta_i \varphi_{i,j}(f) \right) + \mathbb{1}_{\overline{\mathcal{C}}} \left(\sum_{i=1}^{3} \Theta_i \varphi_{i,j}(f) \right), \tag{2.7}$$

where $\overline{\mathcal{C}}$ denotes the complement set of $\mathcal{C}$, $\tilde{g}_j^*(f;\Theta)$ is an approximation of $\tilde{g}_j(f;\Theta)$ on $[0, f^*]$ and $\mathbb{1}$ denotes the indicator function. The spectral density in (2.7) is used in our analysis.

We select Hermite polynomials to construct $\tilde{g}_j^*(f;\Theta)$ with the constraint $\tilde{g}_j^*(f;\Theta) \geq 0$ for $\forall f \in [0, f^*]$, since they provide a piece-wise monotonically increasing function to which we can impose boundary conditions at 0 and f^*, respectively. For a partition $\Pi : 0 = f_1 < f_2 ... < f_{n_f} = f^*$ on the interval $[0, f^*]$, the function $\tilde{g}_j^*(f;\Theta)$ in each subinterval $[f_i, f_{i+1}]$ is an increasing cubic polynomial of the form

$$\tilde{g}_j^*(f;\Theta) = g_i H_1(f) + g_{i+1} H_2(f) + g_i' H_3(f) + g_{i+1}' H_4(f), \tag{2.8}$$

where $\{g_i = \tilde{g}_j(f_i;\Theta),\ i = 1, 2, ..., n_f\}$, $g_i' = (d\tilde{g}(f;\Theta)/df)|_{f_i}$ and n_f is the number of discrete frequencies. Functions $H_k(f)$ are the first four Hermit polynomials. We impose two boundary conditions, that is, (B1) $\tilde{g}_j^*(f;\Theta) = \tilde{g}_j(f;\Theta)$, and (B2) $d\tilde{g}_j^*(f;\Theta)/df = d\tilde{g}_j(f;\Theta)/df$, at $f = 0$ and $f = f^*$. Figure 2.5 shows the approximation of the SBM spectral density $\tilde{g}_j^*(f;\theta = \mathbf{1})$ of $\tilde{g}_j(f;\theta = \mathbf{1})$ for $f \leq f^*$, for cell $(m,r)_j = (5, 100\ km)$ and $f^* = 9\ rad/s$.

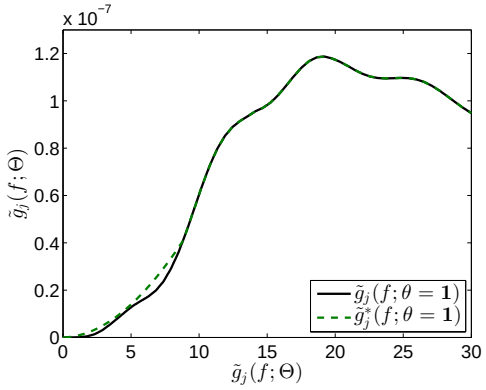

Figure 2.5: Approximation $\tilde{g}_j^*(f)$ of $\tilde{g}_j(f)$ for $(m,r)_j(5, 100\ km)$ and $f < f^* = 9\ rad/s$.

Since $\tilde{g}_j^*(f;\Theta)$ is a polynomial in f, function $\tilde{g}_j^*(f;\Theta)$ is also linear in Θ, i.e.,

$$\tilde{g}_j^*(f;\Theta) = \sum_{i=1}^{3} \Theta_i \varphi_{i,j}^*(f),\ 0 \le f \le f^* \tag{2.9}$$

where $\varphi_{i,j}^*(f)$ are the corresponding modes of $\tilde{g}_j^*(f;\Theta)$ on $[0, f^*]$. More details about the approximation and the numerical algorithm for the interpolation can be found in [20].

2.4 Bayesian Analysis

The stochastic surrogate model in equation (2.7) and the records at the USC site in Table 2.1 are combined within a Bayesian framework to obtain a statistically-updated model for the spectral density. Bayes' theorem states that the posterior density $p(\theta|X(t))$ of the unknown parameters $\theta = [\theta_1, \theta_2, \theta_3] \in \Psi$ is

$$p(\theta|X(t)) \propto f(\theta) l(X(t)|\theta) \tag{2.10}$$

where $f(\theta)$ is the postulated prior density for Θ and $l(X(t)|\theta)$ is the likelihood function, which accounts for the significance of the observed data $X(t)$ in the

distribution of Θ [25]. The prior distribution for Θ may influence significantly the result if the number of records at a single site is small. The prior distribution is usually selected to reflect experts' opinions or historical data. In the current study we only use a non-informative uniform prior, which assumes that all values of Θ in the range Ψ are equally likely before the update. Numerical results are shown for the records in Table 2.1 for the USC.

2.4.1 Prior-Posterior Analysis

Let $X_j(t)$ be the strong motion part of the ground acceleration process in cell j. The strong motion part of the earthquake is the part of the record in which most of its energy is released. A quantitative definition of the strong motion part in terms of the Arias intensity is given in [71]. Following common approaches adopted in [77] (Chap.7), [48] (Sect. 3.2) and [63], we assume that $X_j(t)$ is a zero-mean, stationary, Gaussian process with one-sided power spectral density $\tilde{g}_j(f;\Theta)$. The discrete version of $X_j(t)$ is denoted by $Y_j = [X_j(t_1), ..., X_j(t_{n_t})] \sim N(\mathbf{0}, C_j(\Theta))$, where $t_1 = 0 \leq t_u \leq t_{n_t} = \tau_f$, $u = 1, ..., n_t$, τ_f is the duration of the process $X_j(t)$ and $N(\mathbf{0}, C_j(\Theta))$ denotes the multivariate normal distribution with zero mean $\mathbf{0}$ and covariance matrix $C_j(\Theta)$. A number n of independent samples of $X_j(t)$ yield n independent record samples $\{y_{j,i}\}$ $i = 1, ..., n$ of Y_j. Under this assumption, the logarithmic likelihood function as given by Gelman et al. in [25] (Sect. 3.6) calculated with records from the $j-th$ cell of the seismic activity matrix has the form

$$\log(l(y_j|\theta)) \propto -\frac{n}{2}\log(|C_j(\theta)|) - \frac{1}{2}\sum_{i=1}^{n} y_{j,i}^T C_j(\theta)^{-1} y_{j,i}, \tag{2.11}$$

where $|C_j(\theta)|$ is the determinant of the covariance matrix $C_j(\theta)$ and $y_j = \{y_{j,i},\ i = 1, ..., n\}$ denotes the set of samples from Y_j. The components of the covariance matrix are calculated using the inverse Fourier transform of the approximate spectral density as described by [33] in (Sect. 3.6):

$$c^j_{u,v}(\Theta) := c^j(t_u - t_v; \Theta) = \sum_{h=1}^{n_f} \tilde{g}_j(f_h; \Theta) \cos(f_h(t_u - t_v))\Delta f \ . \tag{2.12}$$

Using equations (2.7) and (2.9) in (2.12), the covariance matrix takes the form

$$C_j(\Theta) = \sum_{k=1}^{3} \Theta_k \left(\mathbb{1}_{\mathcal{C}} Q^{(j,k)} + \mathbb{1}_{\overline{\mathcal{C}}} O^{(j,k)} \right) \ , \tag{2.13}$$

where $Q^{(j,k)}$ and $O^{(j,k)}$ are deterministic matrices with components

$$q^{(j,k)}_{u,v} := q^{(j,k)}(t_u - t_v) = \sum_{h=1}^{n_f} \left(\mathbb{1}_{f_h \leq f^*} \varphi^*_{k,j}(f_h) + \mathbb{1}_{f_h > f^*} \varphi_{k,j}(f_h) \right) \cos(f_h(t_u - t_v))\Delta f \tag{2.14}$$

$$o^{(j,k)}_{u,v} := o^{(j,k)}(t_u - t_v) = \sum_{h=1}^{n_f} \varphi_{k,j}(f_h) \cos(f_h(t_u - t_v))\Delta f, \tag{2.15}$$

respectively, and $f_0 = 0 \leq f_h \leq f_{n_f} = \overline{f},\ h = 1, ..., n_f$ are discrete frequencies equally spaced at $\Delta f = 0.02\ rad/s$ with a cut-off frequency $\overline{f} = 30\ rad/s$.

A computer code which calculates the posterior distribution $p(\theta|X(t))$ for custom prior distributions $f(\theta)$ is available in the electronic supplement to this article.

2.4.2 Model Properties

The results in this section show that the proposed model for the spectral density deviates from the SBM spectral density model by capturing information from the records at a single site. We show analytically and numerically that the

posterior version of the power spectral density converges to the SBM spectral density if seismic ground-acceleration records are samples from the SBM spectral density and the sample size goes to infinity.

One-cell Seismic Activity Matrix.

For an arbitrary cell j of the seismic activity matrix we will use n independent samples of the Gaussian process with power spectral density $g_j(f)$ given in (2.5), i.e., $y_{j,i} \sim N(\underline{0}, C_j(\mathbf{1})),\ i = 1, ..., n$ to update the posterior density $p(\theta|y_j)$. Note that the covariance matrix $C_j(\mathbf{1})$ is calculated with the SBM spectral density since $g_j(f) = \tilde{g}_j(f; \theta = \mathbf{1})$.

The convergence theorem in [25] in Chap. 4 states that under some regularity conditions (notably $\theta_0 \in \Psi$, but not on the boundary of Ψ), as the number of samples $n \to \infty$, the posterior distribution $p(\theta|y_j)$ of Θ approaches normality with mean θ_0 and variance $(nJ(\theta_0))^{-1}$, where θ_0 is the value that minimizes the Kullback-Leibler information in Eq. (2.18) and J is the Fisher information in Eq. (2.16). A rigorous proof of this theorem is provided in [47].

The Fisher information for the case of a vector of unknown parameters is a square matrix $J = \{J_{uv}\}$ of dimension equal to the length of the vector Θ and whose elements are calculated as

$$J_{uv}(\Theta) = \mathbb{E}\left[\left(\frac{\partial \log(l(y_j|\Theta))}{\partial \theta_u}\right)\left(\frac{\partial \log(l(y_j|\Theta))}{\partial \theta_v}\right)\right],\ u, v = 1, 2, 3 \tag{2.16}$$

in which the factors under the expectation operator are independent of each other since the likelihood function $l(y_j|\Theta)$ is linearly dependent on Θ and the random vector Θ has independent components. Thus, the Fisher information

can be written as $J_{uv} = \rho_u \rho_v$ with

$$\rho_\alpha = \mathbb{E}\left[\frac{\partial \log(l(y_j|\Theta))}{\partial \theta_\alpha}\right] = -\frac{n}{2}\mathbb{E}\left[\text{tr}\left(C_j(\Theta)^{-1}\Omega^{(j,\alpha)}\right) - y_{j,1}^T C_j(\Theta)^{-1}\Omega^{(j,\alpha)}C_j(\Theta)^{-1}y_{j,1}\right], \tag{2.17}$$

where $\Omega^{(j,\alpha)} = \mathbb{1}_{\mathcal{C}}Q^{(j,\alpha)} + \mathbb{1}_{\overline{\mathcal{C}}}O^{(j,\alpha)}$ and $\alpha = 1, 2, 3$. In equation (2.17) we used two properties from linear algebra, that is, for a parametric matrix $A(\alpha)$ with parameter α, $\frac{\partial A^{-1}}{\partial \alpha} = -A^{-1}\frac{\partial A}{\partial \alpha}A^{-1}$ and $\frac{\partial (det(A))}{\partial \alpha} = \det(A)\text{tr}\left(A^{-1}\frac{\partial A}{\partial \alpha}\right)$, where $\det$ and tr denote the determinant and the trace of a matrix, respectively.

The Kullback-Leibler information measures the similarity between the likelihood function and the true distribution $f(y_j)$ of the ground-acceleration samples y_j. It is calculated as

$$H(\Theta) = \mathbb{E}\left[\log\left(\frac{f(y_j)}{l(y_j|\Theta)}\right)\right] \propto \mathbb{E}\left[\log\left(\frac{|C_j(\mathbf{1})|^{-\frac{n}{2}}\exp\{-\frac{n}{2}y_{j,1}^T C_j(\mathbf{1})^{-1}y_{j,1}\}}{|C_j(\Theta)|^{-\frac{n}{2}}\exp\{-\frac{n}{2}y_{j,1}^T C_j(\Theta)^{-1}y_{j,1}\}}\right)\right], \tag{2.18}$$

since $y_{j,i}$ are independent, identically distributed samples of $Y_j \sim N(\mathbf{0}, C_j(\mathbf{1}))$. The Kullback-Leibler information is non-negative and its minimum is reached when $H(\theta) = 0$ for $\theta_0 = \mathbf{1}$ [46].

Finally, according to the convergence theorem, the posterior density for $\Theta|y_j$, at the limit $n \to \infty$, is

$$\Theta|y_j \sim N\left(\mathbf{1}, \lim_{n\to\infty}\left(nJ(\mathbf{1})\right)^{-1}\right) \tag{2.19}$$

where $J(\mathbf{1})$ is calculated as shown in equation (2.16) and

$$\lim_{n\to\infty}\left(nJ(\mathbf{1})\right)^{-1} = \lim_{n\to\infty}\frac{1}{n}\begin{pmatrix}\rho_1^2 & \rho_1\rho_2 & \rho_1\rho_2\\ \rho_2\rho_1 & \rho_2^2 & \rho_2\rho_3\\ \rho_3\rho_1 & \rho_3\rho_2 & \rho_3^2\end{pmatrix}^{-1}. \tag{2.20}$$

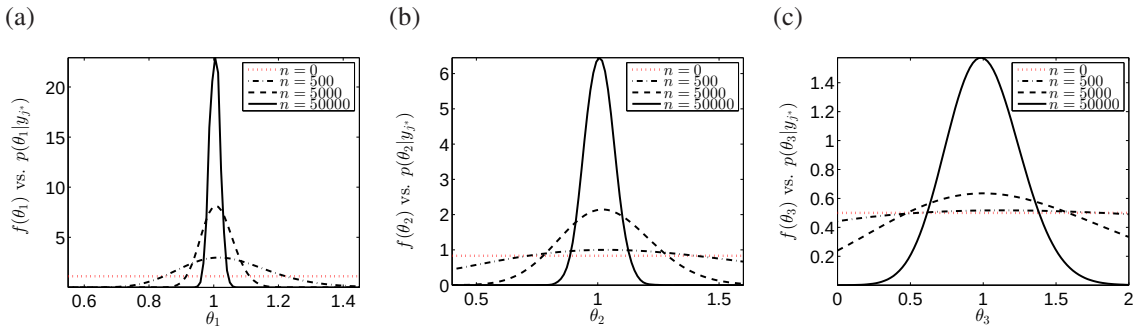

Figure 2.6: Marginal prior density $f(\theta_i)$ vs. marginal posterior density $p(\theta_i|y_{j^*}),\ i = 1, 2, 3$ updated with (a) $n = 500$, (b) $n = 5000$ and (c) $n = 50000$ samples generated from the SBM spectral density.

Thus, the posterior of Θ converges to the target $\mathbf{1}$ when a single cell j is updated with $n \to \infty$ samples generated from the SBM spectral density since all terms $\rho_\alpha,\ \alpha = 1, 2, 3$ depend linearly on n.

Figure 2.6 shows the prior densities $f(\theta)$ and the posterior marginal densities $p(\theta|y_{j^*})$ of $\Theta = [\Theta_1, \Theta_2, \Theta_3]$ calculated for an increasing number $n = 500$, $n = 5000$ and $n = 50000$ of samples y_{j^*}, in cell j^* with $(m, r)_{j^*} = (8, 200\, km)$. We use a uniform prior density on Θ as $f(\theta)$ with a range $\Psi = [0.55, 1.45] \times [0.4, 1.6] \times [0, 2]$.

The posterior probability density concentrates around the mean $\mathbf{1}$ as the number of samples n increases. For a better image of the convergence, Figure 2.7 shows the 95% confidence intervals for the power spectral density $\tilde{g}_{j^*}(f; \Theta)$ for increasing number of samples.

Multiple-cell Seismic Activity Matrix.

We show that the posterior model converges to the target SBM spectral density when samples from all cells of the seismic activity matrix are used in the anal-

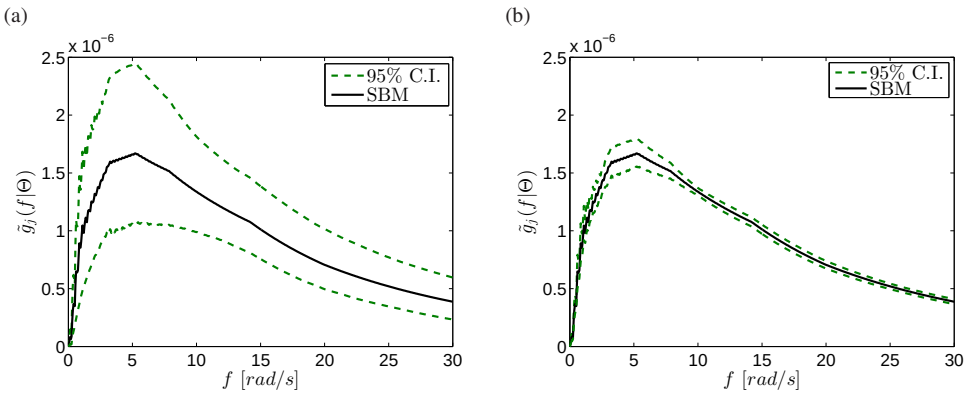

Figure 2.7: 95% confidence intervals for the power spectral density in cell $(m,r)_{j^*} = (8, 200\ km)$ updated with (a) $n = 500$ and (b) $n = 50000$ samples of $Y_{j^*} \sim N(\mathbf{0}, C_{j^*}(\mathbf{1}))$.

ysis. A number n_j of independent samples $y_{j,i} \sim N(\mathbf{0}, C_j(\mathbf{1}))$ with $i = 1, ..., n_j$ are used in each cell $j = 1 \cdots N$. The total number of samples in the statistical update is $n = \sum_{j=1}^{N} n_j$. For all cells of the seismic activity matrix with positive probability $p_j > 0$,

$$\lim_{n\to\infty} \frac{n_j}{n} = p_j, \tag{2.21}$$

as $n \to \infty$ and, implicitly, $n_j \to \infty$.

The Fisher information and the Kullback-Leibler information are calculated as before. The components of the Fisher information $J_{uv} = \rho_u \rho_v$ have the form

$$\rho_\alpha = \mathrm{E}\left[\frac{\partial \log(l(y|\Theta))}{\partial \theta_\alpha}\middle|\Theta = \theta\right] = -\sum_{j=1}^{N} \frac{n_j}{2} \mathbb{E}\left[tr\left(C_j(\Theta)^{-1}\Omega^{(j,\alpha)}\right)\right]$$
$$-\sum_{j=1}^{N} \frac{n_j}{2} \mathbb{E}\left[y_{j,1}^T C_j(\Theta)^{-1}\Omega^{(j,\alpha)} C_j(\Theta)^{-1} y_{j,1}\right], \tag{2.22}$$

where

$$\log(l(y|\Theta)) \propto -\frac{n}{2}\log(|C_j(\Theta)|) - \frac{1}{2}\sum_{j=1}^{N}\sum_{i=1}^{n_j} y_{j,i}^T C_j(\Theta)^{-1} y_{j,i} \tag{2.23}$$

and $y = \{y_{j,i},\ i = 1, ..., n_j,\ j = 1, ..., N\}$ contains all samples of Y_j for all cells j.

Taking the limit $n \to \infty$, equation(2.22) becomes

$$\rho_\alpha = -\frac{1}{2} \lim_{n\to\infty} n \sum_{j=1}^{N} 1_{(p_j>0)} p_j \Big(\mathbb{E}\big[tr\left(C_j(\Theta)^{-1} \Omega^{(j,\alpha)} \right) + y_{j,1}^T C_j(\Theta)^{-1} \Omega^{(j,\alpha)} C_j(\Theta)^{-1} y_{j,1} \big] \Big) \tag{2.24}$$

where $\alpha = 1, 2, 3$. Consequently, at limit the covariance matrix converges to zero as shown in (2.20). The minimum value for the Kullback-Leibler information is also reached at $\theta_0 = \mathbf{1}$. We conclude that the posterior $\Theta|y$ converges to the unit vector $\mathbf{1}$, that is, the posterior spectral density converges to the SBM spectral density, as the number of samples increases to infinity.

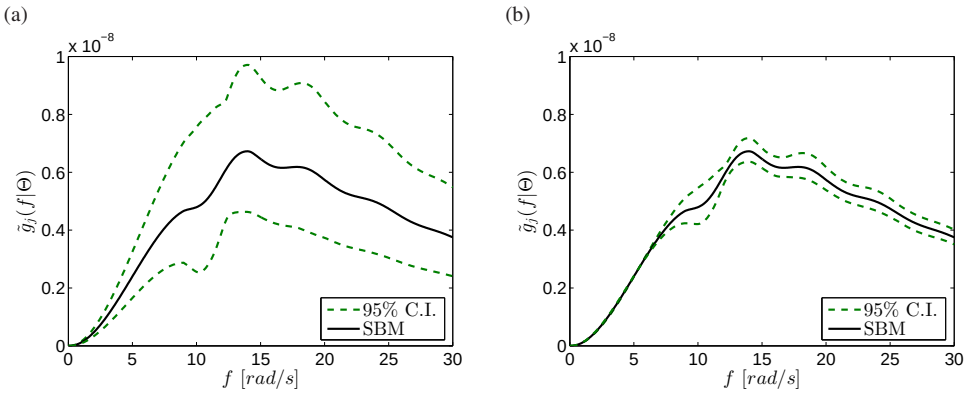

Figure 2.8: 95% confidence intervals for the power spectral density in cell $(m, r)_j = (5, 100\ km)$ updated with (a) $n = 500$ and (b) $n = 50000$ samples of $Y_{j^*} \sim N(\mathbf{0}, C_{j^*}(\mathbf{1}))$.

Due to the high computational effort required to show this result numerically, we perform calculations for a hypothetical seismic activity matrix with two cells $(m, r)_j = (5.4, 240\ km)$ and $(m, r)_{j^*} = (8, 200\ km)$. Only records from cell j^* are used in the statistical update.

The convergence results for marginal densities of Θ and the spectral density for cell j^* are identical with the ones shown in Figure 2.6 and Figure 2.7,

respectively. Figure 2.8 shows the 95% confidence intervals for the marginal posterior densities of Θ in cell $(m, r)_j = (5.4, 240\ km)$. As expected, the spectral density model converges to the target SBM spectral density in any cell as long as the samples used for the statistical update are generated from the SBM density, since Θ is defined as a global parameter for all cells of the seismic activity matrix.

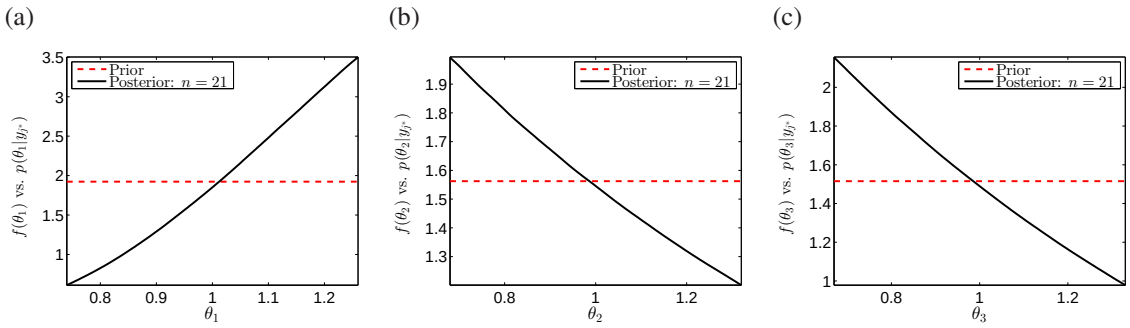

Figure 2.9: Marginal prior density $f(\theta_i)$ vs. marginal posterior density $p(\theta_i|y_{j^*}),\ i = 1, 2, 3$ updated with $n = 21$ records from the USC.

Figure 2.9 shows the uniform prior and the posterior marginal densities of Θ for the statistically-updated model with the records from the USC site, summarized in Table 2.1. The tendency of these densities to converge to a fixed value is very weak in this case due to the small number of samples used in the analysis. The convergence results shown for the two cells in Figure 2.7 and Figure 2.8 are independent on the choice of the prior density $f(\theta),\ \theta \in \Psi$ due to the large number of samples used in the statistical update. For the analysis with the 21 records in Table 2.1 we chose again a non-informative uniform prior on Θ with a range $\Psi = [0.74, 1.26] \times [0.68, 1.32] \times [0.67, 1.33]$.

Figure 2.10 shows the 95% confidence intervals for the spectral density function in cell $(m, r)_{j^*} = (8, 200\ km)$ calculated with the prior density of theta $f(\theta)$ in (a) and with the posterior model $p(\theta|y)$ statistically updated with the $n = 21$

records from the USC in (b). The difference between the two confidence intervals is hardly noticeable due to the small number of records. However, for a fixed frequency $f = 10\ rad/s$ we can see a significant difference in the distributions of $g_{j^*}(f = 10; \Theta)$ shown as histograms for the prior and the posterior distributions of Θ, respectively. The differences in the distributions of the prior and posterior models for the spectral densities is an evidence on how the local data affect the frequency of the ground motion at a site.

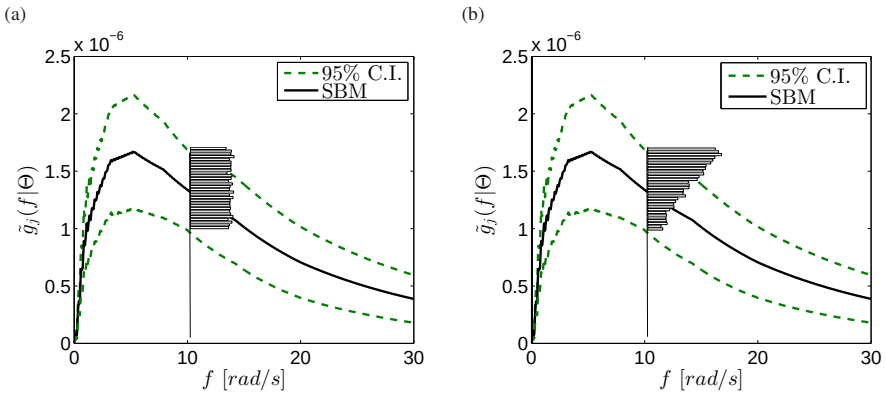

Figure 2.10: 95% confidence intervals for the power spectral density $g_{j^*}(f; \Theta)$ with (a) $f(\theta)$ and (b) $p(\theta|y_{j^*})$ updated with $n = 21$ records from the USC and the corresponding histograms of $\tilde{g}_{j^*}(f = 10; \Theta)$.

2.5 Seismic Hazard Analysis

Two intensity measures IM of the seismic ground acceleration are commonly calculated in probabilistic seismic hazard analysis: the peak ground acceleration ($IM = PGA$) and the response spectral acceleration ($IM = PSa$). Two methods are employed to calculate statistics for the PGA and the PSa: crossing theory described by Grigoriu [69] in (Sect. 7.3) and Monte Carlo simulations. Crossing

theory has a simple form for Gaussian processes as shown in the Appendix. Numerical results are shown for cell $(m, r)_{j^*} = (8, 200\, km)$ for different posterior distributions on Θ, statistically updated with samples simulated from the SBM spectral density and the ground accelerations recorded at the USC, respectively.

2.5.1 Peak Ground Acceleration

Let $\mathcal{D} = [-x, x]$ be a safe set and let $X_j(t)$ be the ground-acceleration process in cell j. The mean rate at which $X_j(t)$ exits $\mathcal{D}$, referred to as the mean $\mathcal{D}$-outcrossing rate, has the expression

$$\eta_j(x;\Theta) = \frac{\dot{\sigma}(\Theta)}{\pi\sigma_j(\Theta)} \exp\left\{-\frac{x^2}{2\sigma_j(\Theta)}\right\}, \tag{2.25}$$

where $\dot{\sigma}_j(\Theta)$ and $\sigma_j(\Theta)$ are the standard deviations for $\dot{X}_j(t)$ and $X_j(t)$, respectively. They are calculated using the spectral density model in (2.7) as

$$\sigma_j(\Theta) = \left(\int_0^{\overline{f}} \tilde{g}_j(f;\Theta)df\right)^{1/2} \tag{2.26}$$

$$\dot{\sigma}_j(\Theta) = \left(\int_0^{\overline{f}} f^2\tilde{g}_j(f;\Theta)df\right)^{1/2}. \tag{2.27}$$

The probability that the PGA of $X_j(t)$, with duration τ_j, exceeds a level $x > 0$ can be approximated by

$$\overline{F}_{PGA_j}(x;\Theta) = \mathbb{P}(\max_{0\le t\le\tau_j}\{|X_j(t)|\} > x|\Theta) \simeq 1 - \exp\{-\eta_j(x;\Theta)\tau_j\}. \tag{2.28}$$

For all our calculations we assume a duration of the strong motion part of $\tau_j = 10\ s$ for all cells j. The probability density function of the PGA for cell j may also be calculated, by integrating out the random vector Θ

$$f_{PGA_j}(x) = \frac{d(\exp\{\eta_j(x|\theta)\tau_j\})}{dx} p(\theta|y_j), \tag{2.29}$$

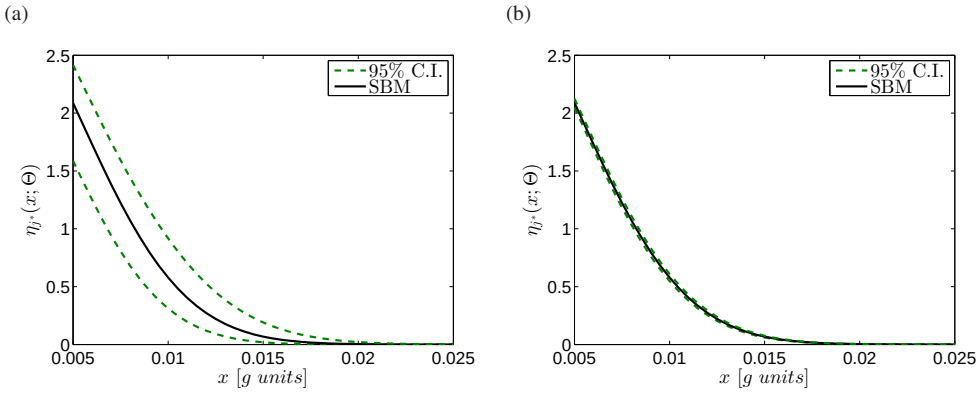

Figure 2.11: 95% confidence intervals for the PGA mean crossing rates $\eta_{j^*}(x;\Theta)$ in cell j^* for (a) $n = 500$ and (b) $n = 50000$ samples generated from the SBM spectral density $\tilde{g}_{j^*}(f;\mathbf{1})$.

where $p(\theta|y_j)$ is the posterior density of Θ as calculated in (2.10) using independent samples y_j of the process $Y_j = [X_j(t_1), ..., X_j(t_{n_t})]$.

Figures 2.11 and 2.12 show the 95% confidence intervals for the crossing rates $\eta_{j^*}(x;\Theta)$ and the tail distribution functions $\overline{F}_{PGA_{j^*}}(x;\Theta)$ for the peak ground accelerations in cell j^*, for the posterior density of Θ updated with $n = 500$ and $n = 50000$ samples generated from the SBM spectral density, respectively (see Figure 2.6).

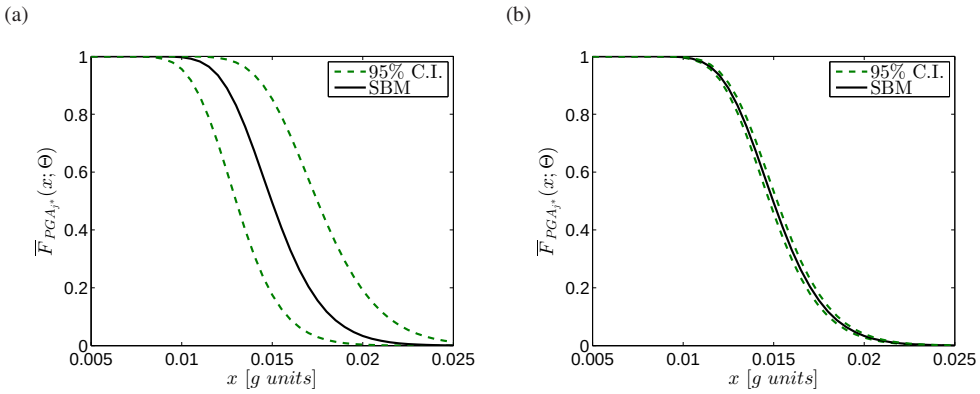

Figure 2.12: 95% confidence intervals for the PGA tail distribution function $\overline{F}_{PGA_{j^*}}(x;\Theta)$ in cell j^* for (a) $n = 500$ and (b) $n = 50000$ samples generated from the SBM spectral density $\tilde{g}_{j^*}(f;\mathbf{1})$.

The statistics in Figure 2.11 and Figure 2.12 show that $\eta_{j^*}(x;\Theta)$ and $\overline{F}_{PGA_{j^*}}(x;\Theta)$ converge to the target mean crossing rates and the tail distribution function calculated with the target SBM spectral density, as the number n of samples, generated from the SBM spectral density, increases. Figure 2.13 illustrates the evolution of the probability density function of PGA, $f_{PGA_{j^*}}(x)$, for increasing number of samples n. The tails of the density are lighter for increasing n. Similar statistics are shown again for cell j^* in Figure 2.14 for the posterior density of Θ updated with all the records available at the USC site. Due to the small number of records, the confidence intervals are wide but a minor shift in the density of the PGA can be noticed.

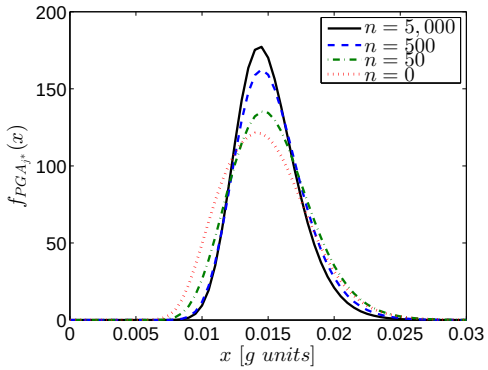

Figure 2.13: Probability density functions $f_{PGA_{j^*}}(x)$ in cell j^* for $n = 0$, $n = 50$, $n = 500$ and $n = 5000$ samples generated from the SBM spectral density $\tilde{g}_{j^*}(f;\mathbf{1})$.

Figure 2.15(a) shows the mean for the 95% peak ground acceleration percentile, that is, the value $PGA_{0.95,j}$ for which $\mathbb{P}(PGA_j \leq PGA_{0.95,j}|\Theta) = 0.95$ for all cells $j = 1, 2, ..., N$. Figure 2.15(b) shows a section through the graph in (a), which illustrates the 95% confidence intervals and the mean of $PGA_{0.95}$ for a fixed $r = 200\ km$.

Figures 2.16 (a) and (b) illustrate the 95% confidence intervals and the mean

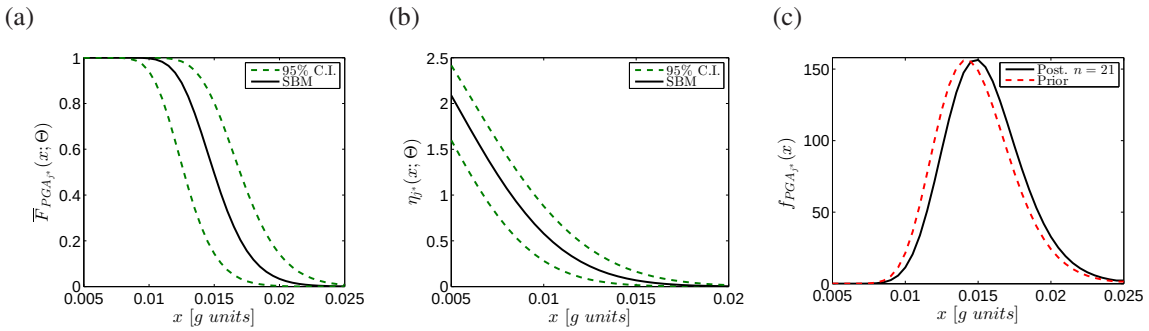

Figure 2.14: 95% confidence intervals for (a) PGA mean crossing rates $\eta_{j^*}(x;\Theta)$, (b) the PGA tail distribution $\overline{F}_{PGA_{j^*}}(x;\Theta)$ and (c) the PGA probability density $f_{PGA_{j^*}}(x)$ for the prior and the posterior spectral density $\tilde{g}_{j^*}(f;\Theta)$ update with $n = 21$ records from the USC.

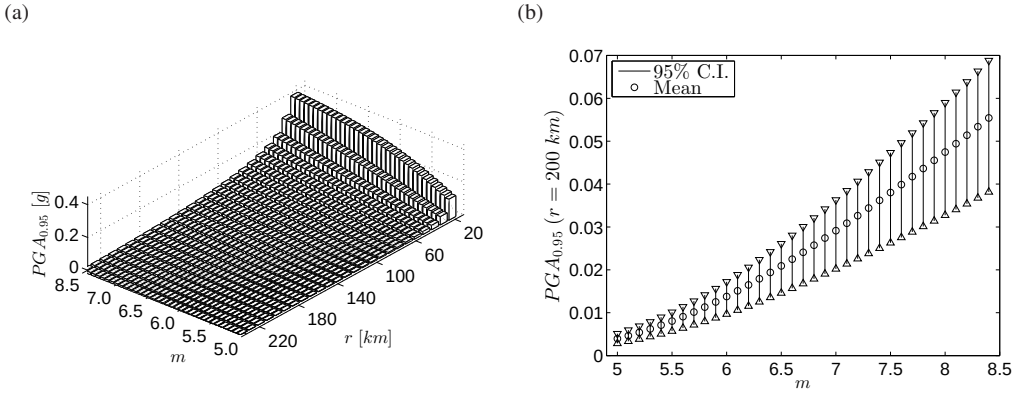

Figure 2.15: (a) Mean values for $PGA_{0.95}$ calculated for all cells j of the seismic activity matrix; (b) Mean and the 95% confidence intervals for $PGA_{0.95}$ for fixed $r = 200$ km.

of $PGA_{0.95}$ for a fixed moment magnitude $m = 8$ in linear and logarithmic scales, respectively.

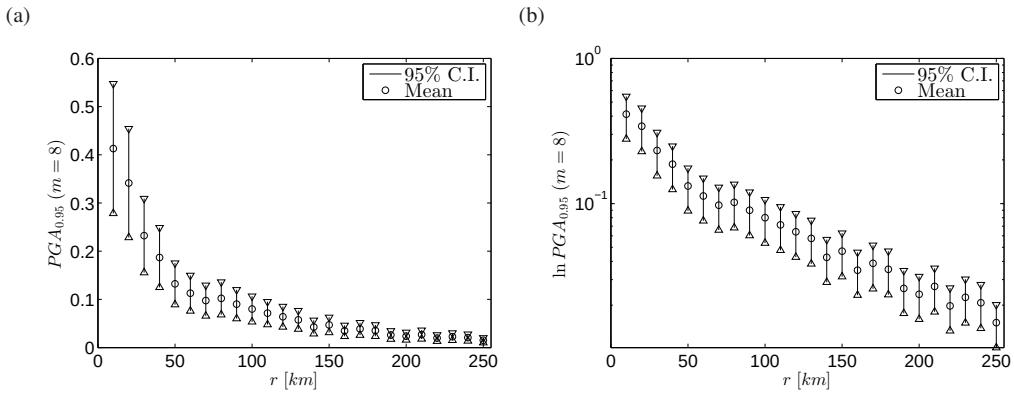

Figure 2.16: Mean and the 95% confidence intervals of the quantile $PGA_{0.95}$ for fixed $m = 8$ in (a) linear and (b) logarithmic scales.

2.5.2 Response Spectral Acceleration

The spectral response is calculated using a single-degree-of-freedom (SDOF) system subjected to the ground-acceleration process $X_j(t)$ in cell j

$$\ddot{Z}_j(t) + 2\omega\zeta\dot{Z}_j(t) + \omega^2 Z_j(t) = X_j(t) \tag{2.30}$$

where $Z_j(t)$ is the displacement process of the SDOF system with natural frequency ω and damping ratio ζ. We define the pseudo-spectral acceleration as

$$PSa(\omega;\zeta) = \omega^2 \max_{0\le t\le\tau_j}\{|Z_j(t;\omega,\zeta)|\}. \tag{2.31}$$

The probability

$$\mathbb{P}\left(PSa(\omega;\zeta) > x\right) = \mathbb{P}\left(\max_{0\le t\le\tau_j}\{|Z_j(t)|\} > \frac{x}{\omega^2}\right). \tag{2.32}$$

can be obtained by following the procedure used for PGA. The probability of exceedance of the PSa can be approximated by

$$\overline{F}_{PSa_j}(x;\Theta) = \mathbb{P}\left(\max_{0\le t\le\tau_j}\{|Z_j(t)|\} > \frac{x}{\omega^2}\right) \simeq 1 - \exp\left\{-\eta_{Z_j}\left(\frac{x}{\omega^2};\Theta\right)\tau_j\right\}, \tag{2.33}$$

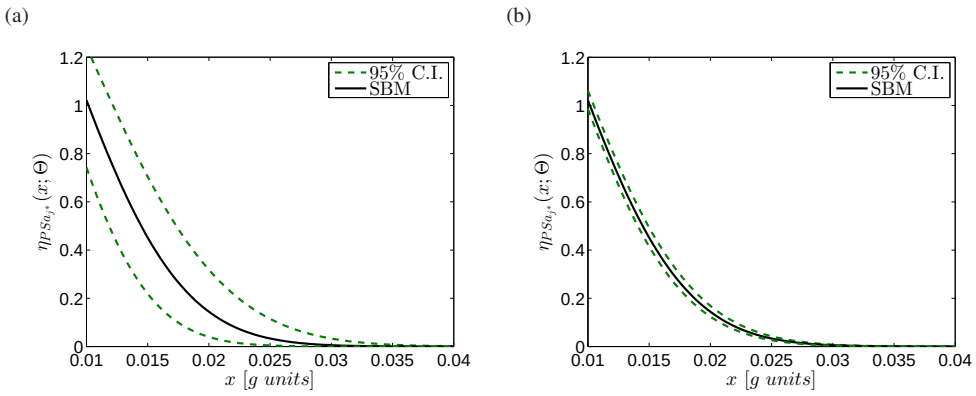

Figure 2.17: 95% confidence intervals for the PSa mean crossing rates $\eta_{PSa_{j^*}}(x;\Theta)$ in cell j^* for (a) $n = 500$ and (b) $n = 50000$ samples generated from the SBM spectral density $\tilde{g}_{j^*}(f;\mathbf{1})$.

where

$$\eta_{Z,j}(z;\Theta) = \frac{\dot{\sigma}_{Z,j}(\Theta)}{\pi\sigma_{Z,j}(\Theta)} \exp\left\{-\frac{z^2}{2\sigma_{Z,j}(\Theta)^2}\right\} \tag{2.34}$$

is the mean crossing rate for the displacement process $Z_j(t)$ with $z = x/\omega^2$ and $\dot{\sigma}_{Z,j}$ and $\sigma_{Z,j}$ are the standard deviations for the displacement $Z_j(t)$ and the velocity $\dot{Z}_j(t)$ processes and can be obtained by (2.26) and (2.27), respectively, with

$$g_{Z,j}(f;\Theta) = |h_Z(f)|^2 \tilde{g}_j(f;\Theta), \tag{2.35}$$

in place of $\tilde{g}_j(f;\Theta)$. The function

$$|h_Z(f)| = \frac{1/\omega^2}{\left[(1-(f/\omega)^2)^2 + (2\zeta\omega)^2\right]^{1/2}} \tag{2.36}$$

is the transfer function between $X_j(t)$ and $Z_j(t)$. The mean crossing rates can also be expressed in terms of acceleration if we use the change of variable $z = x/\omega^2$, and we denote it by $\eta_{PSa_j}(x;\Theta)$. The probability density function $f_{PSa_j}(x)$ of PSa can be calculated as shown in equation (2.29) by replacing the tail distribution $\overline{F}_{PGA_j}(x;\Theta)$ with $\overline{F}_{PSa_j}(x;\Theta)$ in (2.33).

Figures 2.17 and 2.18 show the 95% confidence intervals for the mean crossing rates $\eta_{PSa_j}(x;\Theta)$ and the tail distribution functions $\overline{F}_{PSa_j}(x;\Theta)$ for the

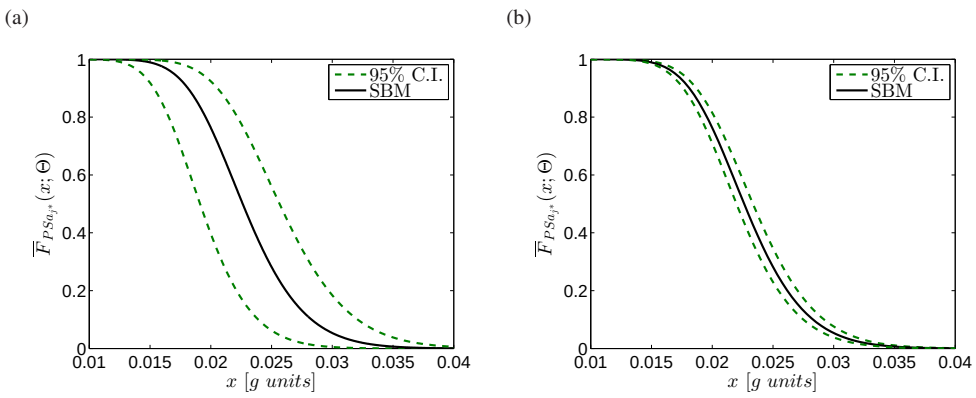

Figure 2.18: 95% confidence intervals for the PSa tail distribution function $\overline{F}_{PSa_{j^*}}(x;\Theta)$ in cell j^* for (a) $n = 500$ and (b) $n = 50000$ generated from the SBM spectral density $\tilde{g}_{j^*}(f;\mathbf{1})$.

pseudo-spectral acceleration $PSa(\omega;\zeta)$ calculated at $\omega = 2\pi\ rad/s$ for $\zeta = 10\%$. The two figures show how the 95% confidence intervals for $\eta_{PSa_j}(x;\Theta)$ and $\overline{F}_{PSa_j}(x;\Theta)$, in cell j^*, narrow down as $n = 500$ and $n = 50000$ SBM-samples are used to calculate the posterior of Θ, respectively (see Figure 2.6).

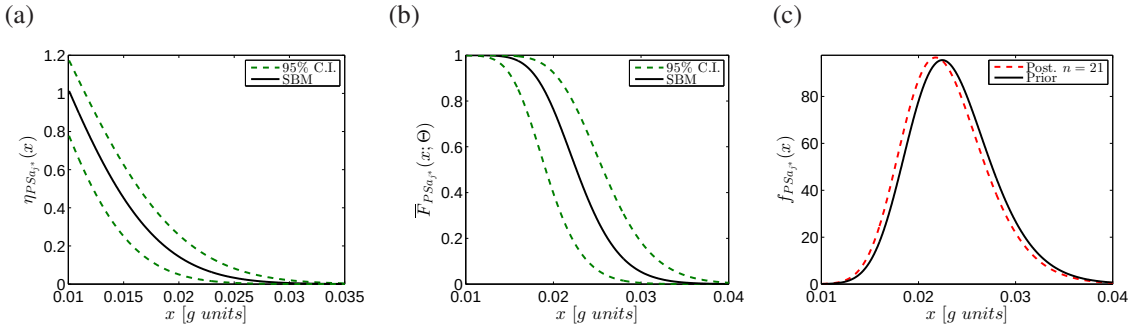

Figure 2.19: 95% confidence intervals for (a) PSa mean crossing rates $\eta_{PSa_{j^*}}(x;\Theta)$, (b) the PSa tail distribution $\overline{F}_{PSa_{j^*}}(x;\Theta)$ for cell j^* and (c) the PSa probability density $f_{PSa_{j^*}}(x)$, for the prior and the posterior spectral density $\tilde{g}_{j^*}(f;\Theta)$ update with $n = 21$ records from the USC.

Similar statistics for the same parameters ω and ζ are calculated for the spectral acceleration at cell j^* and shown in Figure 2.19 for the posterior of Θ updated with the 21 records in Table 2.1. As in the case of the PGA, the confidence

intervals for these statistics on the PSa are wide for the model statistically updated with the actual records due to the small number of records available.

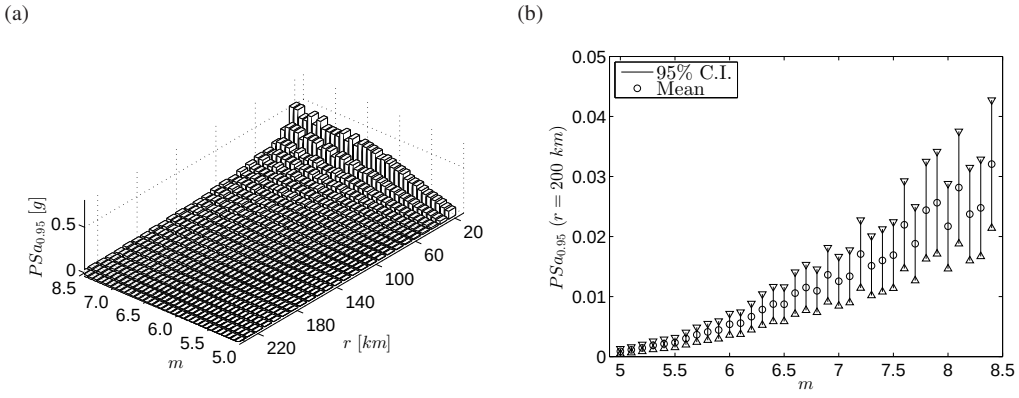

Figure 2.20: (a) Mean values for $PSa_{0.95}$ calculated for all cells j of the seismic activity matrix; (b) Mean and the 95% confidence intervals of $PSa_{0.95}$ for fixed $r = 200\ km$.

Figure 2.20 (a) shows the mean of the 95% response spectral acceleration percentile, that is, the value $PSa_{0.95,j}$ such that $\mathbb{P}(PSa_j(\omega;\zeta) \leq PSa_{0.95,j}|\Theta) = 0.95$ for all cells $j = 1, 2, ..., N$. Figure 2.20 (b) is a section through the graph n (a) for a fixed $r = 200\ km$. Figures 2.21 (a) and (b) show a section through the graph in Figure 2.20, for a fixed $m = 8$ and the corresponding 95% confidence intervals for the $PSa_{0.95}$, in linear and logarithmic scales, respectively.

2.5.3 PSHA Example

The mean annual rates $\nu(x)$ at which an intensity measure IM exceeds a value x constitutes one of the main outputs of the traditional probabilistic seismic hazard analysis (PSHA). It has the expression

$$\nu(x) = \sum_{j=1}^{N} \lambda_j \mathbb{P}(IM > x|(m,r)_j)p_j, \tag{2.37}$$

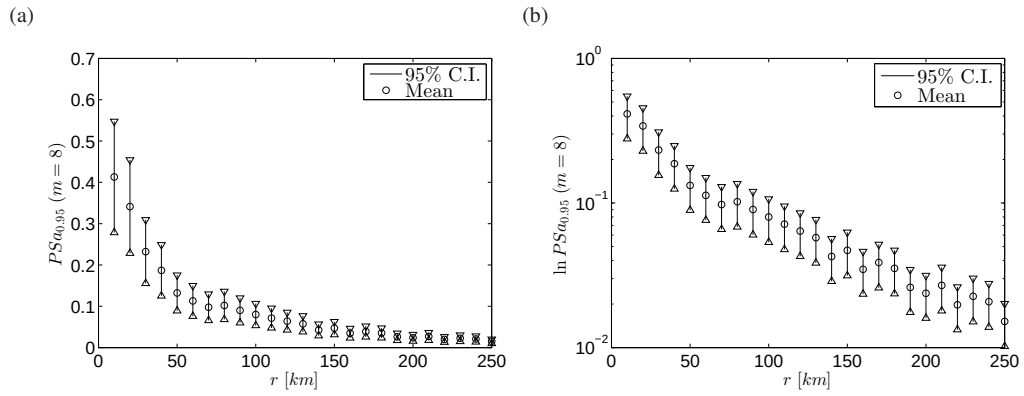

Figure 2.21: Mean and the 95% confidence intervals of the quantile $PSa_{0.95}$ for fixed $m = 8$ in (a) linear and (b) logarithmic scales.

where N is the total number of cells in the seismic activity matrix and λ_j and p_j are the mean annual rate and the probability of occurrence of an earthquakes characterized by $(m, r)_j$ [2]. In classical PSHA, the probability $\mathbb{P}(IM > x|(m, r)_j)$ is calculated by assuming that the logarithm of IM is normally distributed with mean $\overline{\ln(IM)}$ and standard deviation $\sigma_{\ln(IM)}$ obtained from a ground motion prediction model for given $(m, r)_j$ [7]. For the numerical example of the classical PSHA, we use the ground motion prediction model developed by [12] to calculate the parameters $(\overline{\ln(IM)}, \sigma_{\ln(IM)})$ for the distribution of $\ln(IM)$.

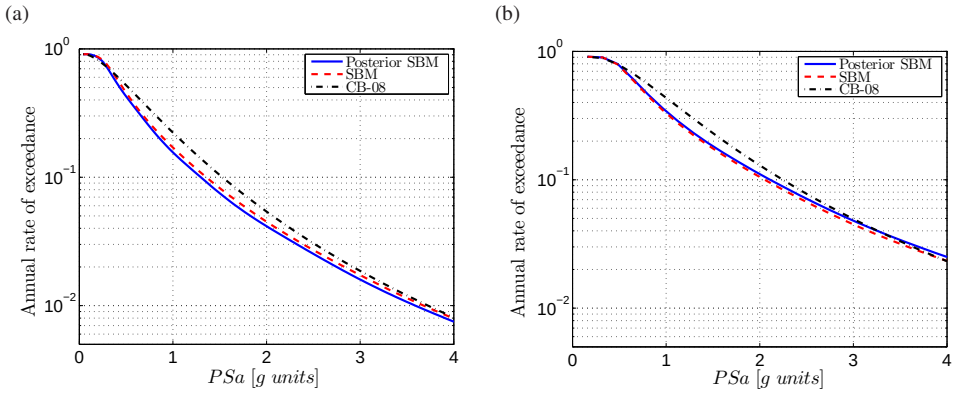

Figure 2.22: Hazard curves for (a) $PSa(T = 1s; \zeta = 5\%)$ and (b) $PSa(T = 0.5s; \zeta = 5\%)$.

In our approach, in which we use the statistically-updated spectral density, the mean annual rate $\nu(x)$ is calculated by rewriting equation (2.37) as

$$\nu(x) = \sum_{j=1}^{N} \lambda_j p_j \int_{\Psi} \overline{F}_{IM_j}(x;\Theta) d\Theta, \tag{2.38}$$

where $\overline{F}_{IM}(x;\Theta)$ is the tail distribution function for the intensity measure IM, as it was calculated in (2.28) and (2.33) directly from data and the seismological model with SBM. No additional assumption on the distribution of the intensity measure is required in this approach. Graphical representations of $\nu(x)$ are known as hazard curves. Figure 2.22 shows the hazard curves calculated by using the classical PSHA and the proposed model before and after statistically updating it with the records from the USC site the intensity measure IM (a) $PSa(T = 1s; \zeta = 5\%)$ and (b)$PSa(T = 0.5s; \zeta = 5\%)$. Differences are noticed between the hazard curves for the proposed model before and after the statistical update, but they can be continuously updated as more records become available at the site.

2.5.4 Deaggregation of (M, R)

The goal of this section is to find a collection of cells for which an intensity measure IM exceeds a threshold x. We refer to the conditional probability

$$\mathbb{P}\left\{(M,R) = (m,r)_j | IM \geq x; \Theta\right\} = \frac{\mathbb{P}\left\{IM \geq x | (M,R) = (m,r)_j; \Theta\right\} p_j}{\mathbb{P}\left\{IM \geq x | \Theta\right\}}, \tag{2.39}$$

as the deaggregation of (M, R), where the probability $p_j = \mathbb{P}\left\{(M,R) = (m,r)_j\right\}$ is the probability of cell j as given by the seismic activity matrix and IM is the intensity measure. Deaggregation of (M, R) represents the probability that an earthquake with magnitude m and source-to-site distance r occurs, under the condition $IM \geq x$ [53, 11].

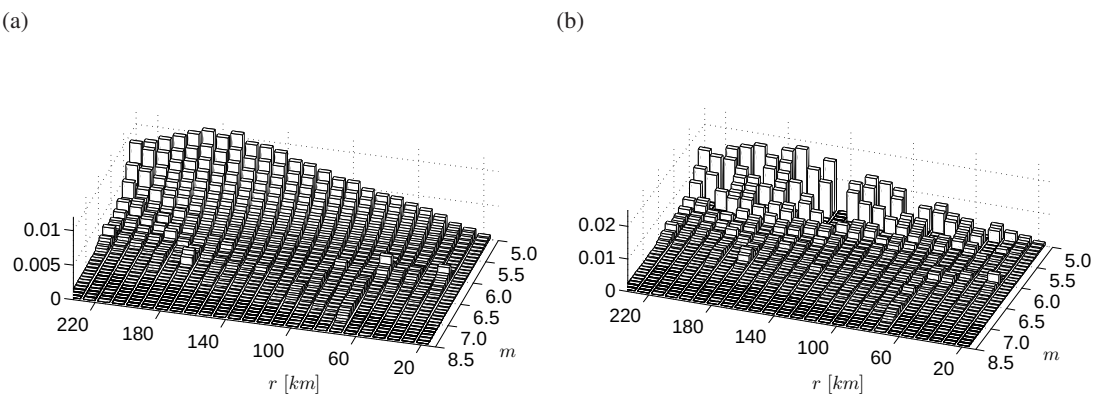

Figure 2.23: Means for the joint conditional random vectors (a) $(M, R)|PGA > 0.02\ g$ and (b) $(M, R)|PGA > 0.20\ g$.

Figure 4.6 shows the conditional probability in equation (2.39) for $IM = PGA$ and levels (a) $x = 0.02\ g$ and (b) $x = 0.20\ g$.

From the definition in (2.39), the conditional probability $\mathbb{P}\{(M, R) = (m, r)_j | IM \geq x; \Theta\}$ converges to p_j in the seismic activity matrix, as the threshold of the IM, $x \to 0$. Figure 2.24 shows the discrete mean and the 95% confidence intervals' bounds for the marginal densities $\mathbb{P}\{M = m | IM \geq x\}$ and $\mathbb{P}\{R = r | IM \geq x\}$, given a $PGA > 0.20\ g$.

The deaggregation gives information about the types of seismic sources which are likely to produce ground motions with $IM > x$. This measure solves at some extent the limitation of the model to statistically update the spectral density in (2.7) with the records available at a single site irrespective of their producing seismic sources.

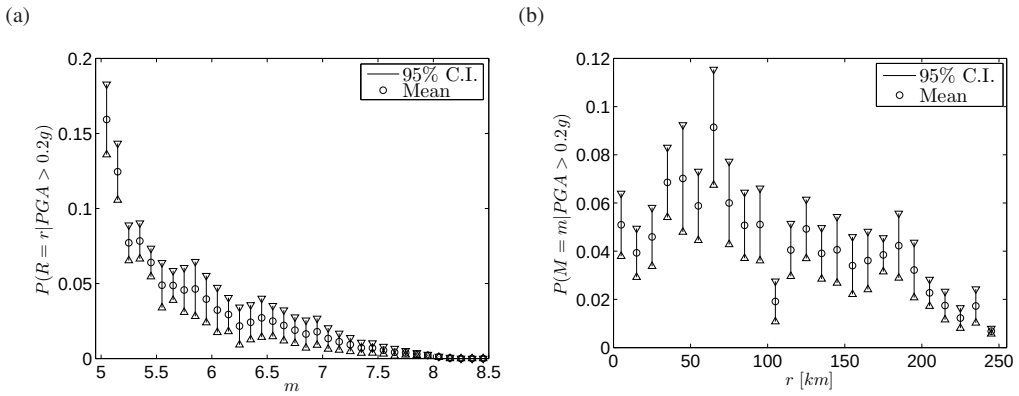

Figure 2.24: Marginal distributions of (a) $(M = m|PGA > 0.20\ g)$ and (b) $(R = r|PGA > 0.20\ g)$.

2.5.5 Ground Motion Simulation

Monte-Carlo simulation is used to produce samples at the USC site after the spectral density model has been statistically updated with the records at a single site. The following algorithm is used to generate samples of the ground-acceleration process at the USC site.

Step 1: Select n samples $(m, r)^{(k)},\ k = 1, ..., n$ from the multinomial distribution of (M, R) given by the seismic activity matrix;

Step 2: Count the number of occurrences of each cell, i.e.,

$$n_j = \sum_{k=1}^{n} \mathbb{1}\{(m, r)^{(k)} = (m, r)_j\}, \tag{2.40}$$

where $n = \sum_{j=1}^{N} n_j$ and N is the number of cells $(m, r)_j$ in the seismic activity matrix;

Step 3: Generate n_j samples $\theta^{(k)} = [\theta_1^{(k)}, \theta_2^{(k)}, \theta_3^{(k)}],\ k = 1, ..., n_j$ of Θ from the posterior density $p(\theta|y)$ and calculate the corresponding spectral density $\tilde{g}_j(f; \theta^{(k)})$ for each cell $j = 1, 2, ..., N$;

Step 4: Generate samples of the ground-acceleration process $X_j(t)$ for each sample $\theta^{(k)}$ in each cell j with $n_j > 0$ by using the spectral representation method described in [33] in (Sect. 3.6), i.e.

$$x_j(t) = \sum_{i=1}^{n_f} \sigma_{j,i}(A_i \sin(f_i t) + B_i \cos(f_i t)) \tag{2.41}$$

where $A_i,\ B_i \sim N(0,1)$, $f_0 = 0 < f_1 < ... < f_{n_f} = \overline{f}$, and $\sigma_{j,i}^2 = \int_{f_{i-1}}^{f_i} \tilde{g}_j(f;\theta^{(k)})df$.

We note that the stationary samples $\{x_j(t)\}$ in equation (2.41) can be modulated to describe approximately the non-stationary character of ground motions, i.e., sample $x_j(t)$ becomes $h(t)x_j(t)$, where $h(t) > 0$ is a deterministic modulation function defined over the earthquake duration [77]. Features and limitations of non-stationary models obtained in this manner are discussed in [35].

An estimator for the cumulative distribution for the PGA using Monte-Carlo simulations is

$$\tilde{\overline{F}}_{PGA}(x) = \mathbb{P}(PGA > x) = \frac{1}{n}\sum_{j=1}^{N}\sum_{i=1}^{n_j} \mathbb{1}\{\max_{0\le t\le \tau_j}(|x_{j,i}(t)|) > x\}, \tag{2.42}$$

where τ_j is the duration of the process $X_j(t)$ samples. The probability density function is then equal to

$$\tilde{f}_{PGA}(x) = \frac{d\left(1 - \tilde{\overline{F}}_{PGA}(x)\right)}{dx}. \tag{2.43}$$

Figure 2.25(a) shows the analytical average PGA probability density function at the USC site, calculated by crossing rates, and the approximate one estimated by using the samples produced. The average analytical density f_{PGA_j} for the entire site is calculated from equation (2.29) by integrating $(m,r)_j$ out. The approximate density estimator from the Monte Carlo samples is given in (2.43)

and it is represented as a histogram.

Similarly, the analytical and the numerical density functions for the $PSa(\omega;\zeta)$ are calculated and plotted in Figure 2.25(b) for $\omega = 2\pi$ and $\zeta = 10\%$. The estimator for the distribution function for the spectral acceleration is

$$\tilde{\overline{F}}_{PS_a(\omega;\zeta)}(x) = \mathbb{P}(PSa(\omega;\zeta) > x) = \frac{1}{n}\sum_{j=1}^{N}\sum_{i=1}^{n_j} \mathbb{1}\{\max_{0\le t\le \tau_{j,i}} (|\ddot{z}_{j,i}(t;\omega,\zeta)| > x)\}, \tag{2.44}$$

where $\ddot{z}_{j,i}(t;\omega,\zeta)$ is a sample of the acceleration process $\ddot{Z}_j(t;\omega,\zeta)$ defined by (2.30). For the numerical calculation of these statistics, $n = 10000$ ground-motion samples were generated.

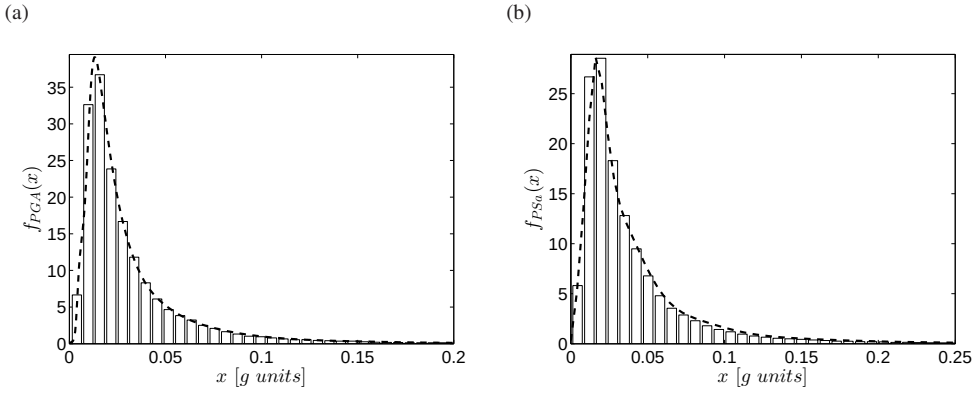

Figure 2.25: The average probability density function calculated by mean crossing rates (dashed line) and by simulation (histogram) for (a) PGA and (b) PSa at the USC site.

2.6 Conclusions

A statistically-updated version of the specific barrier model (SBM) which accounts for all the hazard information available at a site was developed. A stochastic parametric model of the SBM spectral density function was proposed

using the singular value decomposition method. Updating the random unknown parameters in a Bayesian framework with the site ground-acceleration records, the posterior versions of the SBM spectral density were obtained. The statistically-updated model provides probability distributions of the up-to-date, site-specific spectral-density functions. It was shown that the model converges to the spectral density of site ground accelerations, e.g., the SBM if the ground records are produced by this model. Moreover, the distribution of the unknown parameters approaches a Gaussian distribution with specified mean and covariance matrices. Numerical examples which use ground-motion records generated using the SBM spectral density, showed that the confidence interval of the spectral densities converges to the SBM spectral density as the number of samples in the analysis increases.

The posterior model for the spectral densities at University of Southern California in Los Angeles is obtained by statistically updating the SBM with all ground-acceleration records available at that site. The crossing theory for the ground-acceleration process is used to calculate statistics on the peak ground acceleration and the spectral acceleration. The methodology proposed allows the calculation of all quantities considered in the classical probabilistic seismic hazard analysis, e.g. probability of exceedance, quantiles of specified intensity measures etc. In addition, the probability distribution of all these quantities is also known. A Monte Carlo simulation algorithm is proposed for generating samples of the ground acceleration process at a site.

2.7 Data and Resources

The seismograms used in this study were recorded at the University of Southern California station and they were downloaded from the database provided by the Incorporated Research Institutions for Seismology (IRIS) at www.iris.edu. The dataset was downloaded using the MATLAB script provided by IRIS at http://www.iris.edu/dms/nodes/dmc/software/downloads/irisfetch.m/, last accessed in August 2013. The mean annual rates of earthquake occurrences for Los Angeles were obtained by using the 2009 Earthquake Probability Mapping tool available through the United States Geological Survey website https://geohazards.usgs.gov/eqprob/2009/index.php, last accessed in August 2013.

CHAPTER 3

STOCHASTIC REDUCED ORDER MODELS (SROM)

3.1 Introduction

Calculation of response statistics of structures subjected to seismic loads is an essential tool in performance-based seismic design. Monte Carlo is the only general and reliable method to calculate these types of statistics. However, the method is computationally impractical for realistic structural systems since it involves repeated deterministic dynamic analyses for randomly selected samples of seismic load processes. Repeated response analyses for complex structural systems may be costly, which makes Monte Carlo method computationally expensive and therefore impractical.

The framework of linear/nonlinear random vibration is also inadequate for constructing fragility surfaces. Classical theory of linear random vibration provides efficient tools for calculating the first two response moments for linear systems. Unless the input is Gaussian or the output can be assumed to be Gaussian, the first two response moments are insufficient for calculating fragilities ([33], Sect. 7.2). This is a significant limitation since structural systems behave nonlinearly under strong seismic loads.

The main goal of this chapter is to propose a novel, conceptually simple, accurate, non-intrusive, computationally efficient method for calculating response statistics for structures subjected to seismic loads. The method is based on stochastic reduced order models (SROMs) [28], i.e. stochastic processes that have a finite number of samples selected in an optimal manner from the samples

of the target process. Like Monte Carlo simulation, the method uses samples of seismic load processes to characterize structural response and is non-intrusive in the sense that its construction uses deterministic solutions that can be obtained with available software. However, the proposed method uses a small number of load samples selected in an optimal manner. In contrast, Monte Carlo simulation uses a large number of samples selected at random. The use of optimally selected samples allows one to reduce the number of simulations required by the Monte Carlo method by one or two orders of magnitude while retaining accuracy. The method has been originally developed for dynamic response [29]. Recently, it has been shown that for static problems the SROM-based method can be improved significantly [31]. Preliminary studies indicate that similar improvements will provide accurate solutions for random vibration problems [32]. Optimization algorithms have been developed for constructing SROMs for random random vectors [28, 74].

3.2 Stochastic Reduced Order Models

This chapter proposes a model which can capture essential properties of random variables, vectors and random functions with just a few of their samples. The method is an alternative to Monte Carlo and it is useful for solving efficiently differential equations with random coefficients or random input.

3.2.1 SROM for random variables

We consider a real-valued random variable X with a Gamma distribution $F(x),\ x > 0$ with shape and scale parameters parameters $a = 2$ and $b = 0.5$. The set $\{x_i,\ i = 1, ..., n\}$ is composed of n samples of X. We construct a model $\tilde{X}$ with $\tilde{n} << n$ independent samples $\{\tilde{x}_k,\ k = 1, ..., \tilde{n}\}$ of X with weights $\{p_k,\ i = 1, ..., \tilde{n}\}$ such that $\sum_{k=1}^{\tilde{n}} p_k = 1$. The pairs $(\tilde{x}_k, p_k)$ define a stochastic reduced order model $\tilde{X}$ for the random variable X. We select samples $\tilde{x}_k$ of X at random and we choose their corresponding weights p_k such that X and $\tilde{X}$ have similar statistics. In other words, we approximate the distribution of X with a discrete distribution with a given finite number of atoms $\tilde{x}_k,\ k = 1, ..., \tilde{n}$ and weights p_k.

Our goal is to find an optimal vector $\mathbf{p}^{opt} = (p_k^{opt},\ k = 1, ..., \tilde{n})$ of $\mathbf{p} = (p_k,\ k = 1, ..., \tilde{n})$ for the set of samples $\{\tilde{x}_k,\ k = 1, ..., \tilde{n}\}$ which minimizes the differences between the probability laws of X and $\tilde{X}$, measured by the following metric

$$h(\mathbf{p}) = e_1 h_1(\mathbf{p}) + e_2 h_2(\mathbf{p}), \tag{3.1}$$

where $h_1(\mathbf{p}) = \sum_{q=1}^{n_q} w_q(\mu(q) - \tilde{\mu}(q))^2$ measures the differences between the moments $\mu(q)$ and $\tilde{\mu}(q)$ of up to order q of X and $\tilde{X}$, respectively and $h_2(\mathbf{p}) = \int (F(x) - \tilde{F}(x))^2 dx$ measures the differences between the cumulative distributions $F(x)$ and $\tilde{F}(x)$ of X and $\tilde{X}$, respectively, where n_q is the number of moments considered. Coefficients w_q are relative weights between moments and $e_1,\ e_2 > 0$ are some weights which measure the relative contribution of each component in the objective function $h(\mathbf{p})$. The moments of order $q > 0$ and the

distribution for the real-valued variable X are calculated as

$$\mu(r) = \mathbb{E}[X^r] \tag{3.2}$$

$$F(x) = \mathbb{P}(X \leq x), \tag{3.3}$$

where $x > 0$ is the argument of function $F(x)$. The same statistics for the SROM $\tilde{X}$ are evaluated as follows:

$$\tilde{\mu}(q) = \mathbb{E}[\tilde{X}^q] = \sum_{k=1}^{\tilde{n}} p_k \tilde{x}_k^q \tag{3.4}$$

$$\tilde{F}(x) = \mathbb{P}(\tilde{X} \leq x) = \sum_{k=1}^{\tilde{n}} p_k \mathbb{1}\{\tilde{x}_k \leq x\}, \tag{3.5}$$

where $\mathbb{1}$ denotes the indicator function.

Numerical results are shown for $\tilde{n} = 10$, $w_q = 1,\ q = 1, ..., n_q = 5$ and various values of e_1 and e_2. Figure 3.1 shows the actual moments and cumulative distribution function for the Gamma random variable X and the SROM $\tilde{X}$ when only the first $n_q = 5$ moments are considered in the optimization, i.e., $e_1 = 1$ and $e_2 = 0$. The SROM-estimated moments are within an error of 0.24% of the real moments of X, while the mean error between the distribution functions F and $\tilde{F}$ is 4.5%. Figure 3.2 shows the estimated moments and distribution function of X by SROM for the case $e_1 = 0$ and $e_2 = 1$. In this case only the distribution is considered in the objective function $h(\cdot)$ and the error in the estimated moments are up to 53.46%. The heavy-dotted line in Figure 3.3 (a) shows the SROM-estimated first 5 moments of X. These approximate first 5 moments of X delivered by SROM with $\tilde{n} = 10$ samples for $e_1 = 1$ and $e_2 = 1$ are in an error less than 1%. In contrast, Monte Carlo estimates based on the same length as that of $\tilde{X}$can be inaccurate, as illustrated by the one hundred thin lines representing estimates of the first 5 moments of X corresponding to 100 sets of 10 independent samples of X each. The heavy-dotted lines in Figure 3.3 (b) show

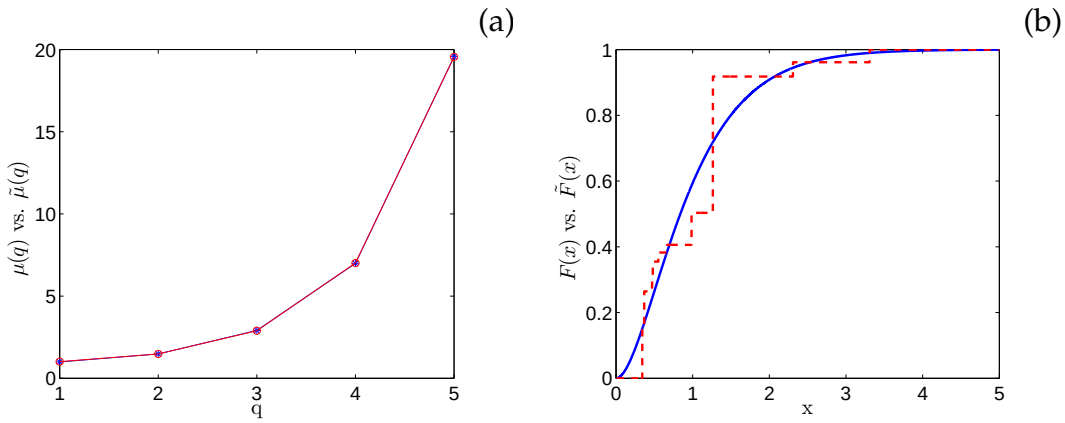

Figure 3.1: (a) Moments and (b) cumulative distribution functions of a Gamma random variable for X (solid blue line) and $\tilde{X}$ (red dashed line) for $e_1 = 1$ and $e_2 = 0$.

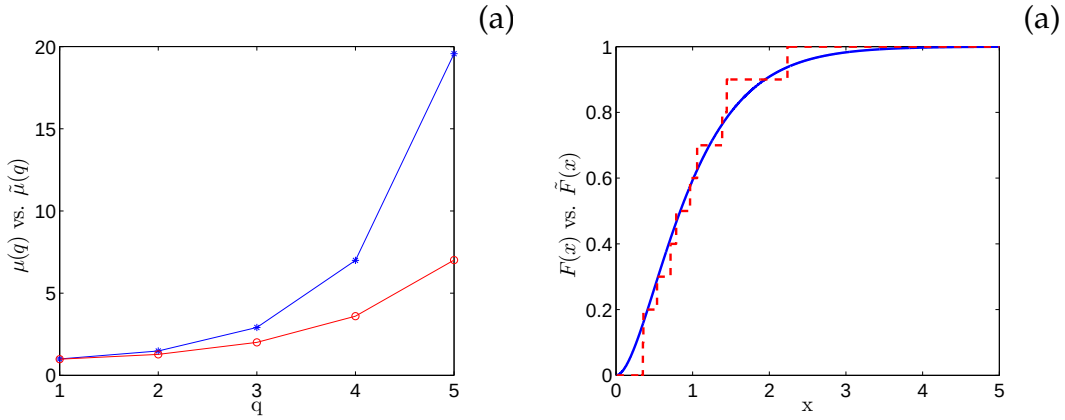

Figure 3.2: (a) Moments and (b) distribution functions of a Gamma random variable for X (solid blue line) and $\tilde{X}$ (red dashed line) for $e_1 = 0$ and $e_2 = 1$.

the SROM estimated and the exact distribution functions of X. The approximate distribution function of X delivered by SROM with $\tilde{n} = 10$ samples for $e_1 = 1$ and $e_2 = 1$ is in an error less than 3%. Similarly, Monte Carlo estimates based on the same length as that of $\tilde{X}$ estimate inaccurately the distributions shown by the 100 thin lines, each corresponding to a set of 10 independent samples of X each.

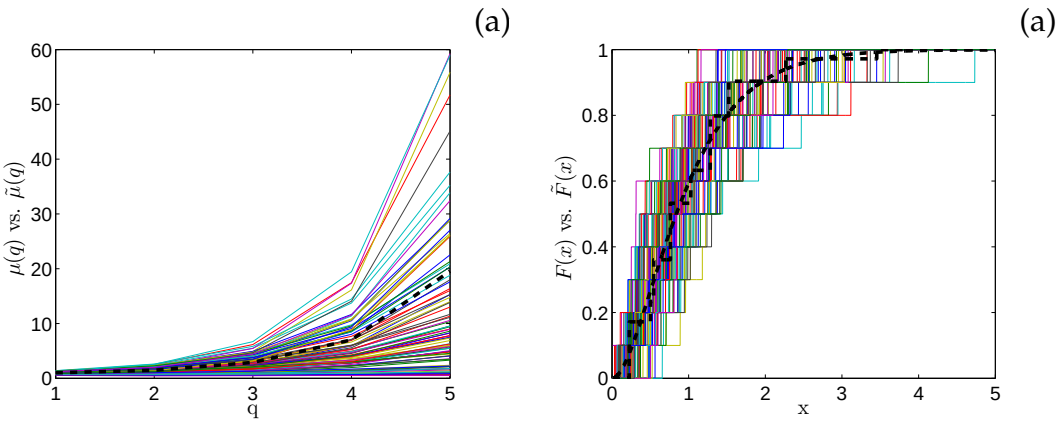

Figure 3.3: Estimates of (a) the first 5 moments and (b) cumulative distribution functions of a Gamma random variable

3.2.2 SROM for stochastic processes

The same method described above can be applied to stochastic processes with direct applications in earthquake engineering. SROMs can be developed for the seismic ground motion acceleration processes.

A new, highly-efficient method is proposed for calculating response statistics. The method is based on stochastic reduced order models (SROMs) and can be viewed as a smart Monte Carlo simulation. The following are the basic steps of the proposed SROM-based method for calculating response statistics.

The stochastic reduced order model is defined directly for the samples of the input process $X(t)$. Any number $\tilde{n}$ of samples $\{\tilde{x_k}(t),\ k = 1, ..., \tilde{n}\}$ of $X(t)$ and probabilities $\{p_k \geq 0,\ k = 1, ..., \tilde{n}\}$ such that $\sum_{k=1}^{\tilde{n}} p_k = 1$ define a stochastic reduced order model. We denote the SROM as $\tilde{X}(t) = \{(\tilde{x}_k, p_k),\ k = 1, ..., \tilde{n}\}$. It has been shown [28] that it is possible to find a selection of $\{(\tilde{x_k}(t), p_k),\ k = 1, ..., \tilde{n}\}$ such that $X(t)$ and $\tilde{X}(t)$ have similar probability laws in terms of cumulative distributions, moments and correlations for $\tilde{n} << n$.

We are looking for a SROM $\tilde{X}(t)$ with a range $\{\tilde{x_k}(t),\ k = 1, ..., \tilde{n}\}$ of independent samples of $X(t)$, a relatively small $\tilde{n}$. Our objective is to find an optimal vector $\mathbf{p}^{opt} = (p_k^{opt},\ k = 1, ..., \tilde{n})$ that minimizes the discrepancies between the probability laws of $X(t)$ and $\tilde{X}(t)$. We obtain $\mathbf{p}^{opt}$ by solving an optimization problem with an objective function which measures differences between various statistics of $X(t)$ and $\tilde{X}(t)$. It is suggested in [28] to use an objective function of the form

$$h(\mathbf{p}) = \sum_{i=1}^{3} e_i h_i(\mathbf{p}), \tag{3.6}$$

where $h_1(\mathbf{p}),\ h_2(\mathbf{p}),\ h_3(\mathbf{p})$ measure the differences between the moments of order q, distributions and correlation functions of $X(t)$ and $\tilde{X}(t)$, respectively, where $(e_i \geq 0,\ i = 1, 2, 3)$ are some weights and $\mathbf{p} = (p_k,\ k = 1, ..., \tilde{n})$.

Statistics of both $X(t)$ and $\tilde{X}(t)$ may be estimated from their samples. Thus, the moments of order q are

$$\mu(t; q) = \mathbb{E}[X^q(t)] = \frac{1}{n} \sum_{i=1}^{n} x_i^q(t), \tag{3.7}$$

$$\tilde{\mu}(t; q) = \sum_{k=1}^{\tilde{n}} p_k \tilde{x}_k^q(t), \tag{3.8}$$

the marginal distributions are

$$F(x; t) = \mathbb{P}(X(t) \leq x) = \frac{1}{n} \sum_{i=1}^{n} \mathbb{1}\left\{x_i(t) \leq x\right\}, \tag{3.9}$$

$$\tilde{F}(x; t) = \sum_{k=1}^{\tilde{n}} p_k \mathbb{1}\left\{\tilde{x}_k(t) \leq x\right\},\ j = 1, ..., n_F \tag{3.10}$$

and, finally, the correlation functions can be calculated as

$$\rho(t,s) = \mathbb{E}[(X(t)-\mu(t,1))(X(s)-\mu(s,1))] \tag{3.11}$$
$$= \frac{1}{n-1}\sum_{i=1}^{n}(x_i(t)-\mu(t,1))(x_i(s)-\mu(s,1))$$
$$\tilde{\rho}(t,s) = \sum_{k=1}^{\tilde{n}} p_k(\tilde{x}_k(t)-\tilde{\mu}(t,1))(\tilde{x}_k(s)-\tilde{\mu}(s,1)). \tag{3.12}$$

Components of the objective function in Eq.(3.6) are calculated using the statistics estimated above.

$$h_1(\mathbf{p}) = \max_{0\le t\le\tau}\left\{\sum_{q=1}^{n_q} w_\mu(t,q)\,|\mu(t;q)-\tilde{\mu}(t;q)|\right\} \tag{3.13}$$
$$h_2(\mathbf{p}) = \max_{0\le t\le\tau}\left\{\int\int w_F(x,t)\left|F(x;t)-\tilde{F}(x;t)\right|dxdt\right\} \tag{3.14}$$
$$h_3(\mathbf{p}) = \max_{0\le t,s\le\tau}\left\{\int\int w_\rho(t,s)\,|\rho(t,s)-\tilde{\rho}(t,s)|\,dtds\right\}, \tag{3.15}$$

where $w_\mu, w_F, w_\Sigma \ge 0$ are weighing functions. Minimizing the objective function in Eq. (3.6) results in obtaining the vector $\mathbf{p}^{opt}$. The optimization problem is repeated for a number of independent sets of $\tilde{n}$ samples of $X(t)$, $\{\tilde{x_k},\ k=1,...,\tilde{n}\}$ and the minimum value of $h(\mathbf{p}^{opt})$ indicates the optimum solution $\mathbf{p}^{opt}$. Note that this is a sub-optimal solution since it involves an iterative procedure repeated for a specified number of times.

3.3 Problem Definition

An application in earthquake engineering is developed to show the efficiency of the SROMs for stochastic processes. We assume $X(t)$ to be a real-valued stochastic process which represents the ground motion acceleration process. In addition to the construction of the SROM, we will also show the advantages of using SROM in response analyses

3.3.1 Ground-Acceleration Process

We use a physical seismological model, called the specific barrier model [37], to describe the probability law of the ground acceleration process $X(t)$. The strong-motion part of the ground motion acceleration at a site located at a distance r from a seismic source producing earthquakes of magnitudes m is assumed to be a zero-mean, stationary, Gaussian process $X(t)$ with one-sided spectral density $g(\nu; m, r)$. The spectral density and the duration of the process t_f are given by the specific barrier model [37] and are depend on (m, r). Figure 5.1 shows an example of the one-sided spectral density for $(m, r) = (7.5, 100\,km)$

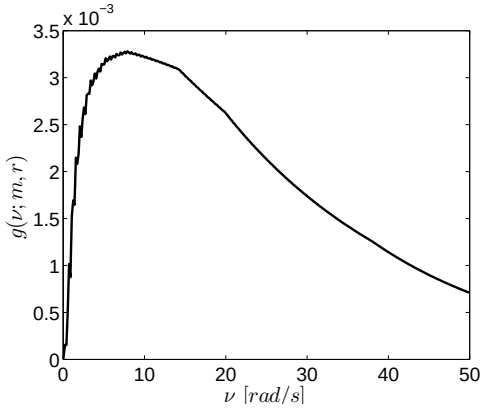

Figure 3.4: Power spectral density for $(m, r) = (7.5, 100\,km)$.

3.3.2 Dynamic Systems

We will use three simple linear and non-linear models for the structural models. The vector process $Y(t)$ satisfies equations

$$\text{Linear: } M\ddot{Y}(t) + C\dot{Y}(t) + KY(t) = -M\underline{1}X(t) \tag{3.16}$$

$$\text{Duffing: } M\ddot{Y}(t) + C\dot{Y}(t) + K(Y(t) + \epsilon Y^3(t)) = -M\underline{1}X(t) \tag{3.17}$$

$$\text{Bouc-Wen: } M\ddot{Y}(t) + C\dot{Y}(t) + K(\xi_1 Y(t) + (1-\xi_1)W(t)) = -M\underline{1}X(t) \tag{3.18}$$

$$\dot{W}(t) = \xi_2\dot{Y}(t) - \xi_3|\dot{Y}(t)||W(t)|^{\xi_5 - 1}W(t) - \xi_4\dot{Y}(t)|W(t)|^{\xi_5},$$

for the linear, Duffing and Bouc-Wen dynamic systems, where M, C and K are the mass, the damping and the stiffness matrices, $\underline{1}$ is a $(N, 1)$ unit vector and $\epsilon, \xi_1, ..., \xi_5$ are parameters for the nonlinear systems. For $N = 1$, M, C and K are scalars and we use the notations $\nu_0^2 = K/M$ and $2\zeta\nu_0 = C/M$. We use $\nu_0 = 2\pi\ rad/s$, $\zeta = 0.02$, $\epsilon = 20$ and $[\xi_1, ..., \xi_5] = [0.5, 0.5, 15, -2.5, 1]$ for the numerical results. Figure 3.5 (a) shows the behavior of the linear and the Duffing oscillators, while Figure 3.5 (b) shows the hysteretic behavior of a Bouc-Wen oscillator subjected to a sample of $X(t)$.

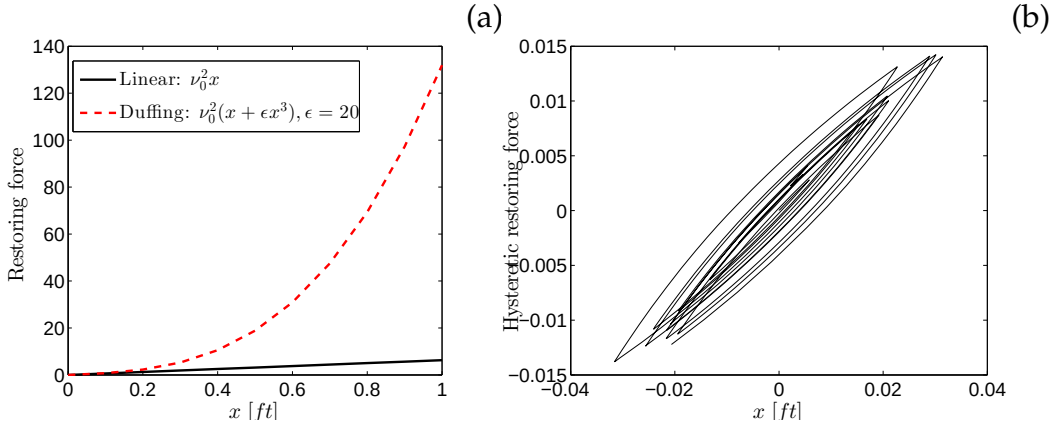

Figure 3.5: Restoring force vs. displacement for (a) linear and Duffing oscillators, and (b) Bouc-Wen oscillator.

For the 2DOF systems we use the previous non-linear parameters and we assume a shear-beam model with masses, stiffnesses and damping coefficients: $M_1 = 10^3\ kg,\ M_2 = 0.75 \times 10^3\ kg, K_1 = 90\ kN/m, K_2 = 65\ kN/m, C_1 = 0.25\ kN.s/m, C_2 = 0.55\ kN.s/m$.

3.4 Solution by Stochastic Reduced Order Models

We develop a SROM $\tilde{X}(t)$ for the stochastic process $X(t)$. The stochastic process $\tilde{X}(t)$ of $X(t)$ is defined by $\tilde{n}$ independent samples $\{x_1(t), ..., x_{\tilde{n}}(t)\}$ of $X(t)$. Samples $\{x_k(t),\ k = 1, ..., \tilde{n}\}$ are usually not equally likely and the probabilities $\mathbf{p} = \{p_k,\ k = 1, ..., \tilde{n}\}$ with $\sum_{k=1}^{\tilde{n}} p_k = 1$ define completely the probability law of $\tilde{X}(t)$. The set of probabilities is obtained by minimizing the objective function defined in Eq. 3.6. The marginal distribution $F(x)$ the moments of order q $\mu(q)$ and the correlation function $\rho(\tau)$ for the ground motion process $X(t)$ are defined by

$$F(x) = \int_{-\infty}^{x} \phi(u)du \tag{3.19}$$

$$\mu(q) = \int_{-\infty}^{\infty} x^q \phi(x)dx \tag{3.20}$$

$$\rho(\tau) = \mathbb{E}[Y(t), Y(t+\tau)] = \int_0^{\overline{\nu}} g(\nu; m, r)\cos(\nu\tau)d\nu, \tag{3.21}$$

where $\phi(x) = (2\pi\sigma^2)^{-0.5}\exp\{-x^2/(2\sigma^2)\}$ is the probability density function for the zero-mean normal distribution with variance $\sigma^2 = \int_0^{\overline{\nu}} g(\nu; m, r)d\nu$ and $\overline{\nu}$ is the cut-off frequency for the spectral density function $g(\nu; m, r)$. The the moments of order q, the marginal density and the correlation function for process $\tilde{Y}(t)$ are defined as shown in Eqs. (3.8), (3.10) and (3.12), respectively. Figure 3.6 shows the target marginal distribution $F(x)$ and the marginal $\tilde{F}(x; t)$ calculated

for $\tilde{n} = 20$ samples and averaged over time. Figure 3.7 (a) shows the moments $\mu(q)$ and $\tilde{\mu}(q;t),\ q = 1, ..., n_q = 5$, averaged over time, and Figure 3.7 (b) shows the correlation functions $\rho(\tau)$ and $\tilde{\rho}(\tau)$ for the first $10\ s$.

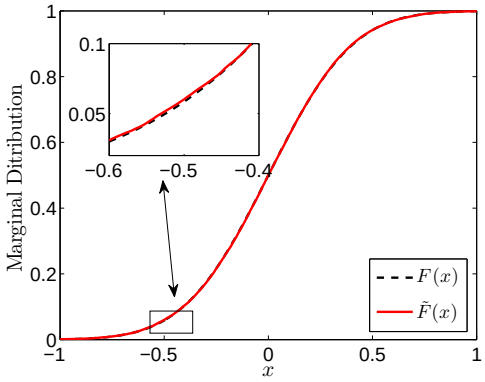

Figure 3.6: Average cumulative distribution function for the stationary ground-acceleration process.

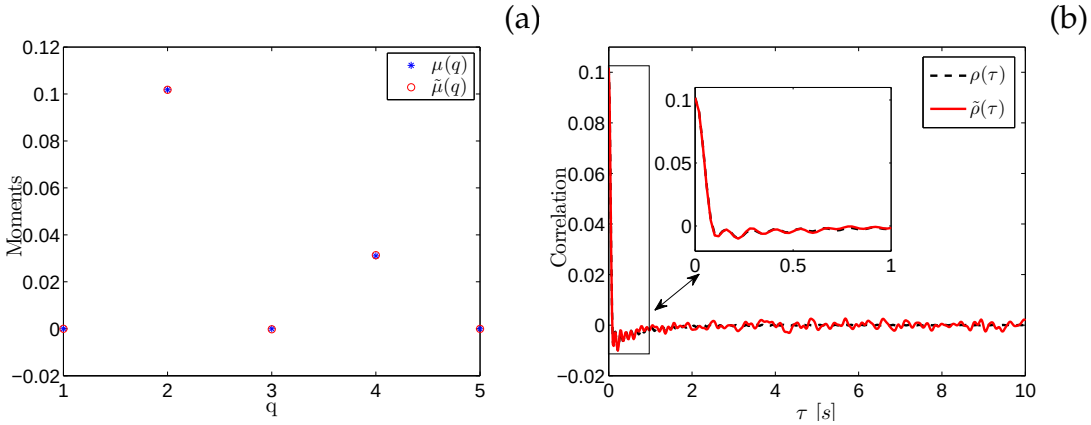

Figure 3.7: (a) Moments and (b) correlation function for the stationary ground-acceleration process $X(t)$.

3.4.1 Response Analysis

Let $Y(t) = \{Y_1(t), .., Y_N(t)\}$ be the relative displacement of a N-degree-of-freedom system subjected to the ground acceleration $X(t)$, as shown in Eqs. (3.16)-(3.18). We calculate the displacement response $Y(t)$ for single-degree-of-freedom (SDOF, $N = 1$) and two-degree-of-freedom (2DOF, $N = 2$) systems.

We calculate response statistics on $Y(t)$ using both Monte-Carlo (MC) simulations and SROM in order to show the efficiency of the proposed method without loss of accuracy. We will calculate the probabilities that the maximum displacement of the SDOF systems and that the maximum inter-storey drift of the 2DOF systems exceed a critical value x_0, that is,

$$\text{SDOF: } P_f(x_0) = \mathbb{P}\left(\max_{0\leq t\leq t_f} |Y(t)| > x_0\right) \tag{3.22}$$

$$\text{2DOF: } P_f(x_0) = \mathbb{P}\left(\max_{0\leq t\leq t_f} |Y_2(t) - Y_1(t)| > x_0\right). \tag{3.23}$$

Numerical evaluation of equation (3.22) using the MC and SROM methods is done as follows:

$$\text{MC: } P_f^{MC}(x_0) = \frac{1}{n}\sum_{k=1}^{n} \mathbb{P}\left(\max_{0\leq t\leq t_f} |x_k(t)| > x_0\right) \tag{3.24}$$

$$\text{SROM: } P_f^{SROM}(x_0) = \sum_{k=1}^{\tilde{n}} p_k \mathbb{P}\left(\max_{0\leq t\leq t_f} |x_k(t)| > x_0\right),\ \tilde{n} << n, \tag{3.25}$$

where $\tilde{n}$ is the number of samples $\{(x_k, p_k),\ k = 1, ..., \tilde{n}\}$ used to construct the range of the SROM $\tilde{X}(t)$ and n is the number of samples of $X(t)$ used in the Monte Carlo analysis. Usually $n >> \tilde{n}$. For each sample $y_k(t)$, the displacement response $x_k(t)$ is calculated by solving the differential equations (3.16-3.18). Probabilities that the response exceeds a critical value x_0, i.e., $P_f^{MC}(x_0)$ and $P_f^{SROM}(x_0)$ are calculated for the SDOF and the 2DOF systems described,

by using $n = 10000$ samples for the MC method and $\tilde{n} = 20, 50, 100$ samples for SROM. Resulting probabilities of failure are shown in Fig. 3.8-3.13.

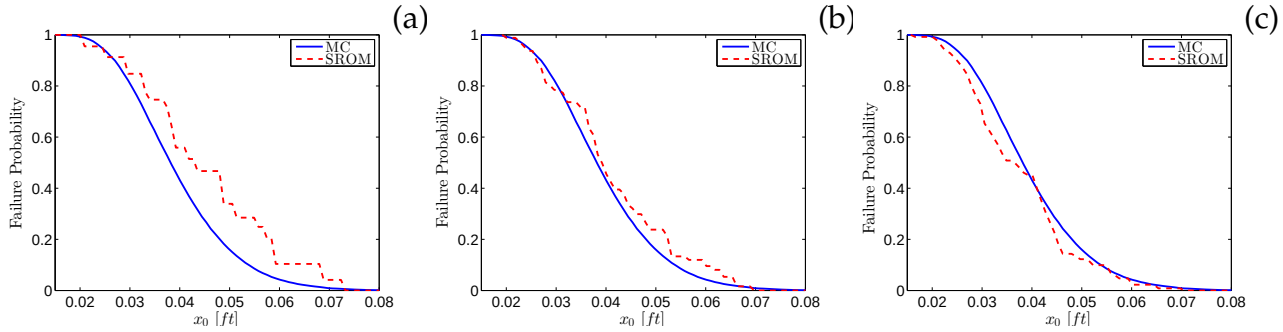

Figure 3.8: SDOF linear system - MC analysis with $n = 1000$ vs. SROM analysis with (a) $\tilde{n} = 20$, (b) $\tilde{n} = 50$, (c) $\tilde{n} = 100$ non-stationary samples

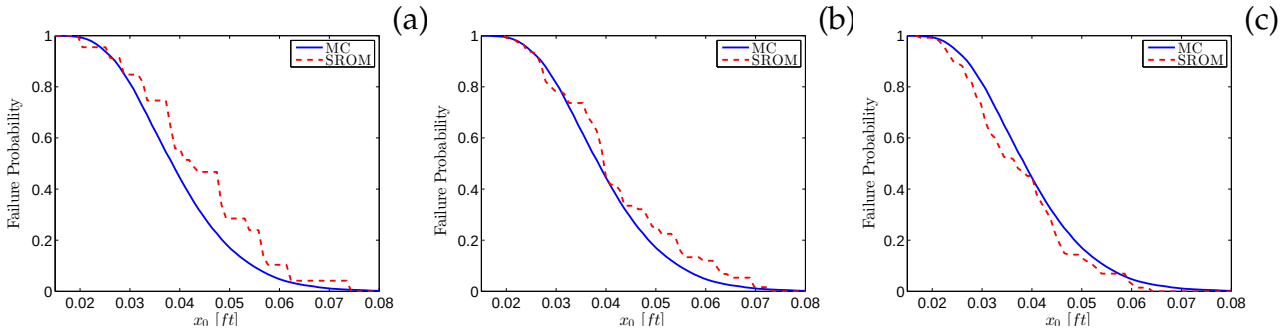

Figure 3.9: SDOF Duffing system - MC analysis with $n = 1000$ vs. SROM analysis with (a) $\tilde{n} = 20$, (b) $\tilde{n} = 50$, (c) $\tilde{n} = 100$ non-stationary samples

The relative error between the probabilities of failure calculated using the MC and the SROM methods is defined as

$$err = \frac{\int (|P_f^{SROM}(x_0) - P_f^{MC}(x_0)| dx_0)}{\int P_f^{MC}(x_0) dx_0} \times 100 \tag{3.26}$$

and it is calculated for all systems considered and summarized in Table 3.1. The relative error between the probabilities of failure calculated using the Monte Carlo and the stochastic reduced order models methods decreases as the number of samples $\tilde{n}$ in the SROM range increases. The improvement in the results

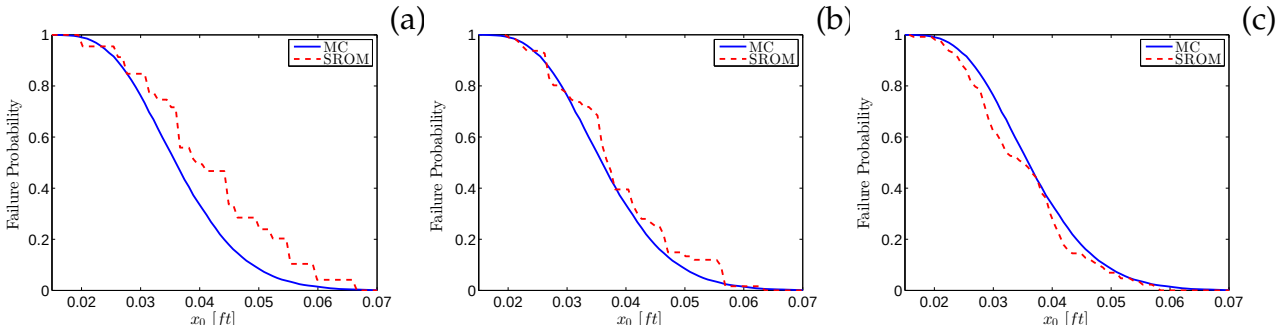

Figure 3.10: SDOF Bouc-Wen system - MC analysis with $n = 1000$ vs. SROM analysis with (a) $\tilde{n} = 20$, (b) $\tilde{n} = 50$, (c) $\tilde{n} = 100$ non-stationary samples

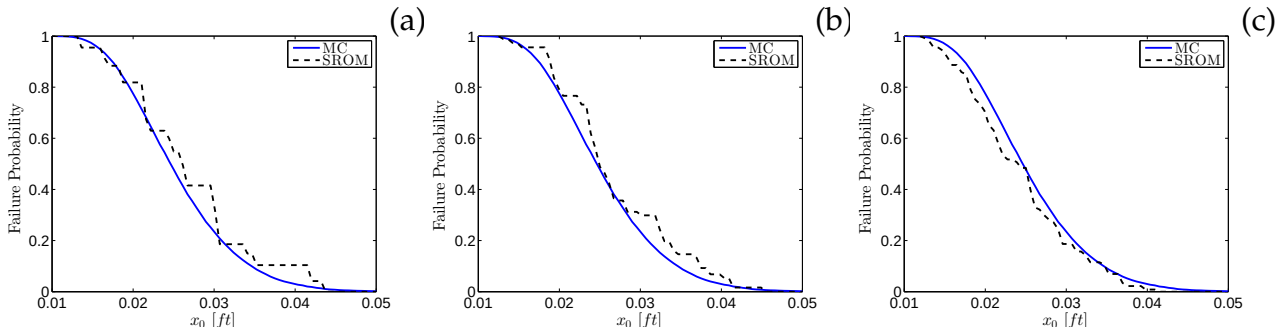

Figure 3.11: 2DOF linear system - MC analysis with $n = 1000$ vs. SROM analysis with (a) $\tilde{n} = 20$, (b) $\tilde{n} = 50$, (c) $\tilde{n} = 100$ non-stationary samples

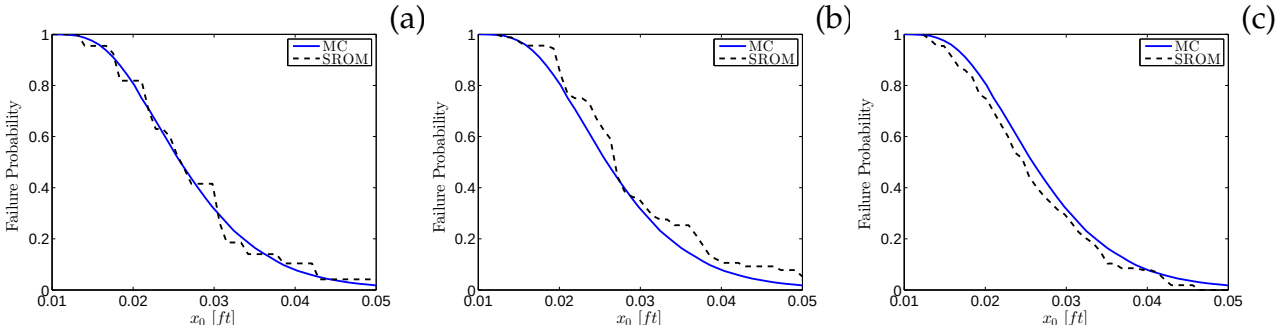

Figure 3.12: 2DOF Duffing system - MC analysis with $n = 1000$ vs. SROM analysis with (a) $\tilde{n} = 20$, (b) $\tilde{n} = 50$, (c) $\tilde{n} = 100$ non-stationary samples

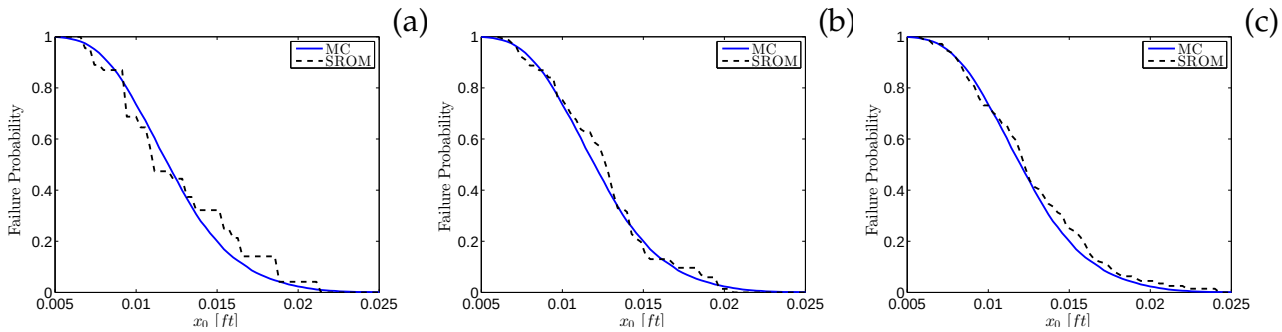

Figure 3.13: 2DOF Bouc-Wen system - MC analysis with $n = 1000$ vs. SROM analysis with (a) $\tilde{n} = 20$, (b) $\tilde{n} = 50$, (c) $\tilde{n} = 100$ non-stationary samples

Table 3.1: Relative errors

System	20 samples	50 samples	100 samples
SDOF linear	14.29	5.50	5.31
SDOF Duffing	10.78	6.46	5.95
SDOF Bouc-Wen	13.22	4.99	4.86
2DOF linear	6.02	5.62	4.89
2DOF Duffing	3.82	7.28	5.59
2DOF Bouc-Wen	6.14	3.14	3.56

obtained by increasing the number of samples from $\tilde{n} = 50$ to $\tilde{n} = 100$ is insignificant. We can conclude that the new method is highly efficient and with less effort we can produce approximate results that are within a relative error of $3 - 8\%$ from the Monte-Carlo results.

3.5 Conclusions

A new, highly efficient method has been proposed to calculate response statistics for structural systems subjected to seismic loads. The method is based on the stochastic reduced order models that can be viewed as a smart Monte Carlo simulation. Unlike the Monte Carlo method which uses a large number of samples selected at random, the new method uses a much smaller number of samples that are selected in optimal manner. The method is implemented to calculate probabilities of failure for linear and nonlinear, single-degree-of-freedom and multiple- degree-of-freedom systems subjected to earthquakes characterized by a selected moment magnitude and source-to-site distance . The SROM estimates of failure probabilities match satisfactorily the Monte-Carlo estimates of these probabilities although they are based on a small number of seismic ground acceleration samples.

CHAPTER 4

LIMITATION OF CURRENT APPROACHES AND IMPROVEMENTS

4.1 Introduction

Fragility curves are plots of probabilities that structural systems enter specified damage states as functions of measures of seismic ground intensity, e.g., peak ground acceleration [45, 66] or selected ordinate(s) of response spectra [23, 49]. They are commonly used in performance-based seismic design of structural and non-structural systems to assess their performance under seismic loads. The construction of fragility curves requires large numbers of ground acceleration records particularly when dealing with highly reliable structures. Since the number of ground motions is rather small even in highly seismic regions, methods have been proposed to overcome the shortage of available site records.

The methods for calculating fragility curves use various procedures for augmenting site records. These methods can be divided in three groups. The first class of methods for calculating fragility curves, known as multiple stripes analysis [50, 6], uses selected ground motion records from a large datasets, e.g., the PEER NGA Database, recorded at various sites. The records are selected to match the response spectrum conditioned on some target spectral ordinate [54, 9] and then used to calculate probabilities of exceeding specified damage states [50, 51]. In [5, 42], the response acceleration spectrum used is conditioned on a given value of the spectral acceleration $PSa^{target}(T_0;\zeta_0)$ at a period of interest T_0 and damping ratio ζ_0. The conditioning spectral ordinate $PSa^{target}(T_0;\zeta_0)$ corresponds to a certain exceedance probability at a given site. We will refer to this method as conditional-spectrum ground-motion selection method (CS-

GMS).

The second class of methods, known as incremental dynamic analysis (IDA), involves repeated scaling of the same set of available seismic ground motions to increasing intensity measures until the specified damage state is reached [73, 75, 26]. Scaling ground motions is conceptually simple and, therefore, attractive, but it may lead to unsatisfactory results since scaling does not change the frequency content. Thus, ground motions used to construct fragilities have the same frequency content irrespective of their intensity, an assumption that is at variance with observations [30, 44].

Finally, the third class of methods is less used in practice, but used in this chapter as a reference result to compare the performance of the first two methods. The method involves repeated dynamic analyses for either all available records in a dataset or large number of artificial ground motion records produced by Monte Carlo simulations. Usually, postulated probabilistic and/or physical models calibrated to actual seismic records [76, 37] are used to produce artificial ground acceleration records. The usefulness of the method depends on the quality of the ground motion models and the set of available site records used for model calibration. One of these methods uses a seismological model based on the specific barrier model [37] and site records to update the seismic ground acceleration process at a site, depending on moment magnitude m and site-to-source distance r [62]. Another method which uses artificial ground-motion records to enrich an existent dataset of ground-motion records is presented also in [65].

This chapter has two main objectives: (1) show limitations of current methods for fragility analysis and (2) propose an improved alternative for calculat-

ing fragility curves similar to the first class of methods (CS-GMS), also based selecting ground motion records from large datasets. Important drawbacks of fragility curves are due to the characterization of ground motions by a single intensity measure parameter, which may provide unsatisfactory results [44]. Moreover, the methods used for fragility-curves calculations have their own limitations. Scaling ground motion records only changes the amplitudes of ground motions and not their frequency content. Also, current practices select ground motion records based on the response of linear single-degree-of-freedom oscillators, even though they are used for further analyses of nonlinear or multi-degree-of-freedom systems. Since fragility curves are traditionally used as a common tool in performance-based seismic design, we will propose calculating fragility curves using multiple stripes analysis based on a novel method for selection of ground motion records. The proposed method is based on stochastic reduced order models (SROM) and selects records based on the probability law of the ground motion process rather than the response of single-degree-of-freedom systems.

The first part of this chapter shows numerical examples which point out limitations of using scalar intensity measures for fragility analysis. Then, fragility curves as functions of spectral acceleration are calculated using the multiple stripes analysis (CS-GMS) and incremental dynamic analyses(IDA) and compared with the third class of methods, i.e. the reference method, based on all ground motion records available. The second part of the paper presents a new method for calculating fragility curve. The method is similar with the multiple stripes analysis but uses ground motions selected by SROM. We will refer to this method as SROM-based ground motion selection method (SROM-GMS).

4.2 Problem Definition

For the purpose of this paper we will construct fragility curves for linear and non-linear structural systems subjected to simulated and actual records from PEER NGA database. Governing equations of the systems and full description of the ground-motion datasets are presented in this section.

4.2.1 Structural systems

Let $X(t) = [X^{(1)}(t), X^{(2)}(t), ..., X^{(N_{DOF})}(t)]^T$ be the relative displacement process of a N_{DOF}-degree-of-freedom systems subjected to the ground acceleration process $Z(t)$. Then the process $X(t)$ satisfies Eq. (4.1) for a linear system

$$M\ddot{X}(t) + C\dot{X}(t) + KX(t) = -M\underline{1}Z(t) \tag{4.1}$$

and the differential Eq. (4.2) for a Bouc-Wen non-linear system

$$M\ddot{X}(t) + C\dot{X}(t) + K(\rho X(t) + (1-\rho)W(t)) = -M\underline{1}Z(t), \tag{4.2}$$

where

$$\dot{W}^{(i)}(t) = a\dot{X}^{(i)}(t) - b|\dot{X}^{(i)}(t)||W^{(i)}(t)|^{n-1}W^{(i)}(t) - c\dot{X}^{(i)}(t)|W^{(i)}(t)|^n \tag{4.3}$$

and M, C, K are the mass, the damping and the stiffness matrices, $\underline{1}$ is a $(N_{DOF} \times 1)$ unit vector, ρ, a, b, c, n are the non-linear parameters and $X^{(i)}$ and $W^{(i)}$ are the relative and hysteresis displacement of degree of freedom $i = 1, 2, ..., N_{DOF}$.

For the case of single-degree-of-freedom (SDOF) systems, i.e., $N_{DOF} = 1$, we use the following notations $T_0^2 = 4\pi^4 M/K$ and $4\pi\zeta_0/T_0 = C/M$. Numerical results are shown for a linear SDOF system and a Bouc-Wen system with $T_0 = 1\ s$, $\zeta_0 = 5\%$.

We will also consider one two-degree-of-freedom linear system (2DOF), i.e., $N_{DOF} = 2$ and one 2DOF Bouc-Wen system. We use a shear-beam model to calculate the mass, stiffness and damping matrices

$$M = \begin{pmatrix} M_1 & 0 \\ 0 & M_2 \end{pmatrix}, \; K = \begin{pmatrix} K_1 + K_2 & -K_2 \\ -K_2 & K_2 \end{pmatrix}$$
$$C = \begin{pmatrix} C_1 + C_2 & -C_2 \\ -C_2 & C_2 \end{pmatrix}, \tag{4.4}$$

where $M_1 = 10^3 \; kg$, $M_2 = 750 \; kg$, $K_1 = 245 \; kN/m$, $K_2 = 35 \; kN/m$, $C_1 = 0.63 \; kNs/m$, $C_2 = 1.45 \; kNs/m$ for the linear and the Bouc-Wen 2DOF systems. The parameters of the systems are chosen such that the first modal period and damping ratios to be similar to the ones of the linear SDOF system, i.e., $T_0 \simeq 1 \; s$ and $\zeta_0 \simeq 5\%$. The non-linear parameters for both SDOF and 2DOF Bouc-Wen systems are $\rho = 0.5, \; a = 0.5, \; b = 15, \; c = -2.5, \; n = 1$.

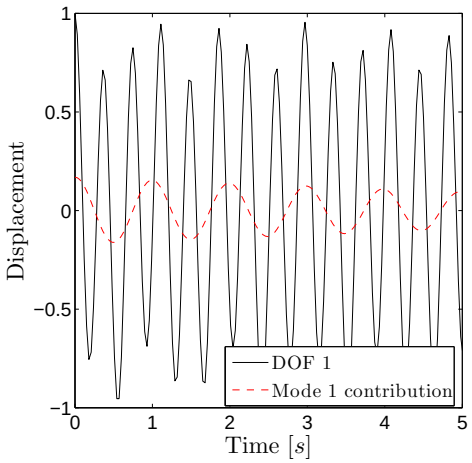

Figure 4.1: 2DOF linear system - displacement of the first degree-of-freedom and first-mode contribution.

The 2DOF linear system is chosen such that both modes of vibration have comparable contributions. Figure 4.1 shows the displacement of the first degree-

of-freedom and the corresponding first-mode contribution in the response.

4.2.2 Ground motion datasets

We use two datasets of ground motions in this study: (1) a dataset with $N = 5000$ artificial ground motion samples and (2) the PEER dataset, composed of a collection of approximately $N = 3500$ ground-motion records from 147 earthquakes. We will use the artificial ground-motion dataset for showing limitations of the current methods used in practice and the PEER dataset to validate a newly proposed ground-motion-selection method.

For the artificial dataset, we assume that the ground motion process $Z(t)$ is a zero-mean, non-stationary, Gaussian process defined by

$$Z(t) = f(t)Y(t),\ 0 \leq t \leq \tau, \tag{4.5}$$

where τ is the total duration of the ground motion,

$$f(t) = \alpha t^{\beta} \exp\{-\gamma t\} \tag{4.6}$$

is a deterministic modulation function, in which α, β, γ are constants and $Y(t)$ is a zero-mean, stationary, Gaussian process with one-sided spectral density $g(\nu; m, r),\ \nu \geq 0$ depending on the moment magnitude m and the source-to-site distance r. The spectral density function $g(\nu; m, r)$, the sample duration τ and constants $\alpha,\ \beta,\ \gamma$ are results of the specific barrier model [37]. The specific barrier model is a source model, as part of a seismological model, which gives the spectral density function of $Z(t)$ in (4.5) as a function of (m, r), tectonic properties and soil conditions. We use $(m = 6.85, r = 8\ km)$, a inter-plate tectonic regime and a shear velocity in the top $30\ m$ of soil of $v_{30} = 620\ m/s$ for which

$\tau = 14.3\ s$ and $\alpha = 0.2787,\ \beta = 1.2531$ and $\gamma = 0.1663$, to construct the artificial samples in the dataset.

Figure 4.2 shows the spectral density $g(\nu; m = 6.85, r = 8\ km)$ and a sample of the process $Z(t)$ with the corresponding modulation function $f(t)$, respectively.

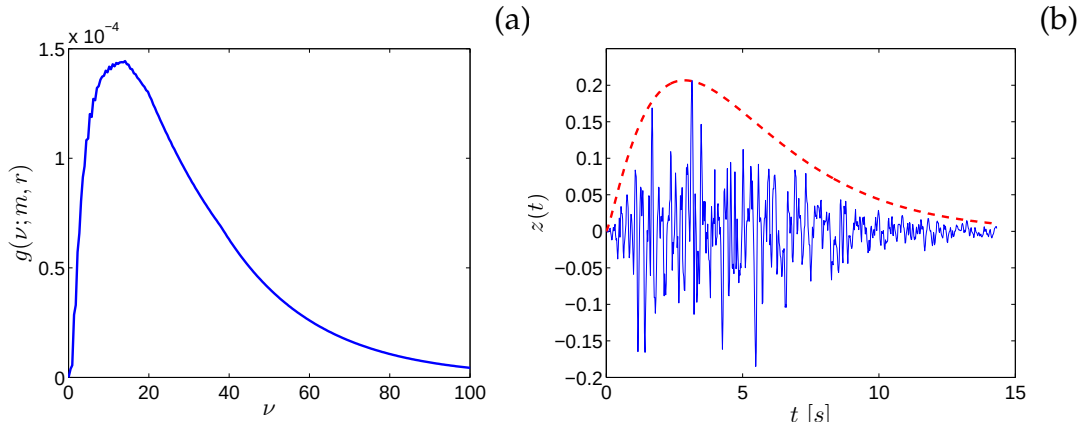

Figure 4.2: (a) One-sided spectral density $g(\nu; m = 6.85, r = 8\ km)$; (b) Sample of the ground motion process $Z(t)$ and corresponding modulation function $f(t)$.

4.3 Limitations of Current Methods for Fragility Analysis

Limitations of current methods for fragility analyses are due to (1) the use of scalar intensity measures to characterize the ground motion process and (2) the scaling of ground motion records and the heuristic methods for selecting records.

4.3.1 Scalar Ground-Motion Intensity Measures

Intensity measures currently used for constructing fragility curves quantify properties of seismic ground acceleration records by, e.g., peak ground acceleration (PGA) or ordinate(s) of response acceleration spectra (PSa). Conceptual simplicity is the main features of these seismic intensity measures. A notable drawback is the lack of uniqueness, i.e., ground motions with rather different features may have similar intensity measures. Fragilities corresponding to motions with similar intensity measures may differ significantly, particularly when dealing with nonlinear structures.

Let $\{Z_k(t)\}$, $k = 1, \ldots, m$, be competing probabilistic models for the seismic ground acceleration at a site. These models are assumed to be stationary, mean-square-differentiable Gaussian processes with mean zero, one-sided spectral density $g_k(\nu)$, $\nu \geq 0$, and duration τ. We show that these processes can have the same intensity measures but very different spectral properties so that systems subjected to these models can have rather different responses and, therefore, different fragilities. These observations imply that (1) the probabilistic models $\{Z_k(t)\}$ are indistinguishable if current intensity measures are used for model selection and (2) the fragility for a nonlinear system may be inaccurate if, e.g., $Z_1(t)$ provides a realistic representation of site seismicity and $Z_2(t)$ with the same intensity measure as $Z_1(t)$ but significantly different frequency content are used to construct fragilities. These statements are supported by the following theoretical considerations and numerical illustrations.

The distribution $F_k(z) = P\big(\max_{0\leq t\leq \tau} |Z_k(t)| \leq z\big)$, $z > 0$, of the peak ground

acceleration $\max_{0\leq t\leq\tau}|Z_k(t)|$ under model $Z_k(t)$ can be approximated by

$$F_k(z) \simeq \exp\big\{-\nu_k(z)\,\tau\big\} = \exp\left\{-\frac{\dot\sigma_k\,\tau}{\pi\,\sigma_k}\,\exp\left(-\frac{z^2}{2\,\sigma_k^2}\right)\right\}, \tag{4.7}$$

where $\sigma_k^2 = \int_0^\infty g_k(\nu)\,d\nu$ and $\dot\sigma_k^2 = \int_0^\infty \nu^2\,g_k(\nu)\,d\nu$ denote the variances of $Z_k(t)$ and $\dot Z_k(t)$. This distribution can be used to calculate the mean, the mode, and any other statistics of $\max_{0\leq t\leq\tau}|Z_k(t)|$. The density $f_k(z) = dF_k(z)/dz$ of $\max_{0\leq t\leq\tau}|Z_k(t)|$ has the expression

$$f_k(z) \simeq \frac{\dot\sigma_k\,\tau\,z}{\pi\,\sigma_k^3}\,\exp\left\{-\frac{\dot\sigma_k\,\tau}{\pi\,\sigma_k}\,\exp\left(-\frac{z^2}{2\,\sigma_k^2}\right)-\frac{z^2}{2\,\sigma_k^2}\right\}. \tag{4.8}$$

Since in our setting the peak ground acceleration $\max_{0\leq t\leq\tau}|Z_k(t)|$ is a random variable, we use as intensity measure the mode of $f_k(z)$, i.e., the value of z that maximizes this density. This is not a standard definition. One can use, for example, the expectation or quantiles of $\max_{0\leq t\leq\tau}|Z_k(t)|$.

Similar considerations apply if ordinates of response spectra are used as intensity measures. These ordinates are maxima $\max_{0\leq t\leq\tau}|R_k(t)|$ of responses $R_k(t)$ of linear oscillators with selected natural frequencies and damping ratios that are subjected to the ground acceleration models $\{Z_k(t)\}$. The response $R_k(t)$ can be the displacement, the velocity or the acceleration of the linear oscillator in Eq. (4.1). The steady-state displacements of the oscillator to ground motions $\{Z_k(t)\}$ are stationary Gaussian processes with mean zero and spectral density $g_{r,k}(\nu) = |h_k(\nu,\zeta)|^2\,g_k(\nu)$, $\nu>0$, where $h_k(\nu,\zeta)$ denotes the oscillator frequency response function. The ordinates of the displacement spectra are the modes of the density of maximum absolute response. This density has the functional form in Eq. 4.8 with σ_k and $\dot\sigma_k$ given by the formulas following this equation in which $g_k(\nu)$ is replaced with $g_{r,k} = |h_k(\nu,\zeta)|^2\,g_k(\nu)$ for the selected a period T_0 and damping ratio ζ_0, as they were defined in Eq. (4.1).

Figure 4.3 shows spectral densities of three ground motion processes indexed by $k = 1, 2, 3$ for Los Angeles that correspond to different moment magnitudes m and site-to-source distances r. These spectral densities are provided

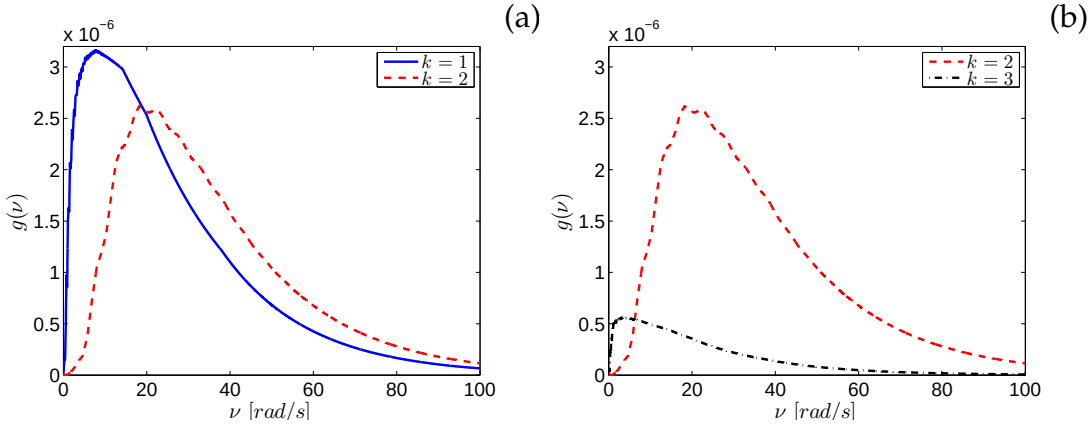

Figure 4.3: Power spectral density for $(m, r)_{k=1} = (7.5, 100\ km)$, $(m, r)_{k=2} = (5.4, 30\ km)$, $(m, r)_{k=3} = (8, 210\ km)$

by a seismological model [37]. According to this model, the strong motion part of ground motion acceleration time histories are samples of stationary Gaussian processes with zero mean and spectral densities shown in this figure. The frequency contents of the three processes differ significantly. Yet, the modes of the densities of peak ground accelerations $\max_{0\le t\le\tau}|Z_k(t)|$ and response maxima $\max_{0\le t\le\tau}|R_k(t)|$, $\tau = 10\ s$, may coincide. For example, the modes of peak ground accelerations $\max_{0\le t\le\tau}|Z_k(t)|$ coincide for processes indexed by $k = 1$ and $k = 2$ coincide, as shown in the left panel of Fig. 4.4. Panel (b) of this figure shows probabilities that maximum response of a Bouc-Wen oscillator whose displacement is the solution of the differential equation (4.2) exceeds a limit displacement x_{cr}, that is

$$P_f(x_{cr}) = \mathbb{P}\{\max_{0\le t\le\tau}|X_k(t)| > x_{cr}\}, \tag{4.9}$$

where $X_k(t)$ satisfies Eqs. (4.2). The probabilities in Fig. 4.4(b) correspond to the ground motion processes $Z_1(t)$ and $Z_2(t)$. The differences between these

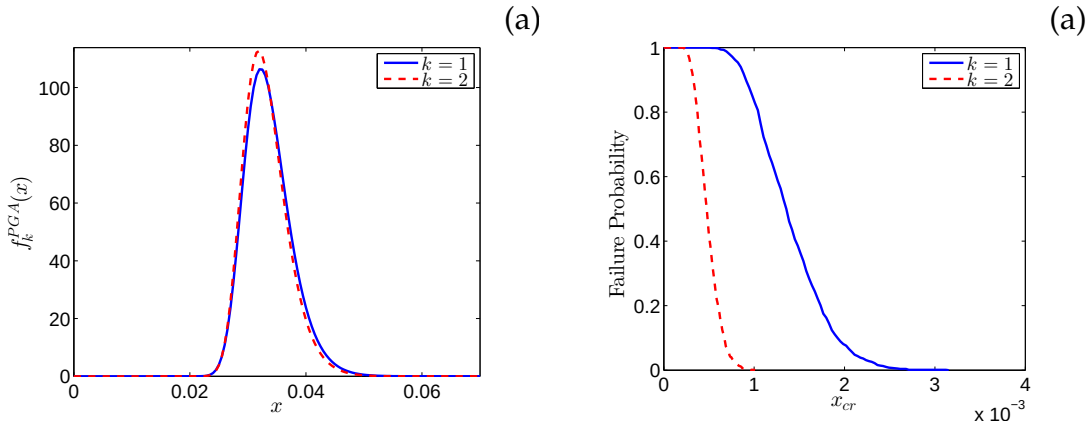

Figure 4.4: PGA probability density function for $k = 1, 2$ (left panel) and $P_f(x_c r)$ using motions from models $k = 1, 2$ (right panel)

probabilities are significant although the ground motions $Z_1(t)$ and $Z_2(t)$ are indistinguishable if characterized by their peak ground accelerations.

The use of ordinates of response spectra as measures of seismic intensity can also be unsatisfactory. Figure 4.5 (a) shows the densities of $\max_{0\le t\le\tau}|R_k(t)|$ for

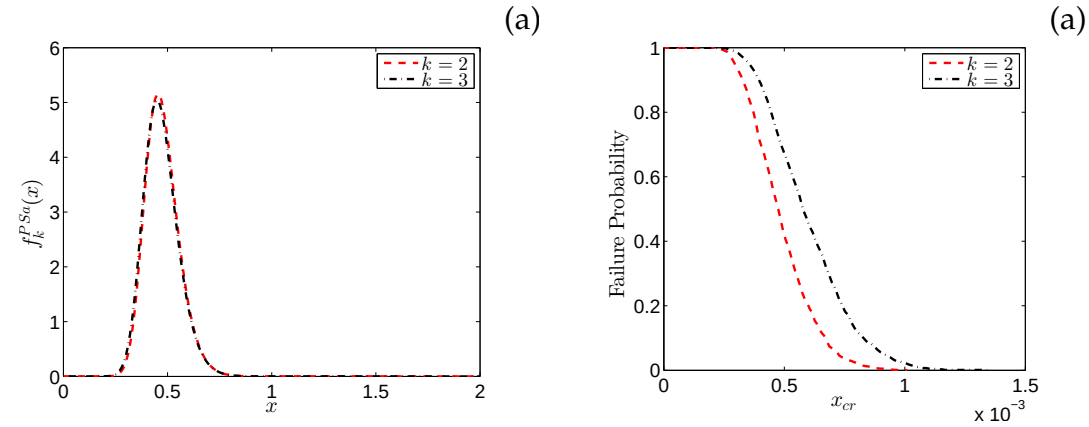

Figure 4.5: PSa probability density function for $k = 2, 3$ (left panel) and $P_f(x_c r)$ using motions from models $k = 2, 3$ (right panel)

$T_0 = 1$ s and $\zeta_0 = 5\%$ under the ground motion processes $Z_2(t)$ and $Z_3(t)$. The modes of the densities of these responses coincide. Yet, the performance of the Bouc-Wen oscillator measured by the probability of exceeding limit displace-

ments x_{cr} differ significantly, as illustrated by Fig. 4.5(b).

4.3.2 Fragility Curves

Our goal in this section is to calculate and compare fragility curves for the systems presented in Eqs. (4.1) and (4.2) using three classes of methods: (I) the multiple stripes analysis by ground-motion selection using the conditional spectrum (CS-GMS), (II) the incremental dynamic analysis (IDA) and (III) reference method whish uses all records available in the dataset. We define failure as the exceedance of a critical value δ_{cr} of an engineering design parameter (EDP). For the SDOF systems, the EDP is defined as the maximum displacement, i.e. $EDP_i = \max_{0\leq t\leq \tau} |x_i(t; T_0, \zeta_0)|$. For the 2DOF systems, the EDP is defined as the maximum inter-storey drift $EDP_i = \max_{0\leq t\leq \tau} |x_i^{(1)}(t; T_0, \zeta_0) - x_i^{(2)}(t; T_0, \zeta_0)|$, where $x_i(t) = [x_i^{(1)}(t)\ x_i^{(2)}(t)]$. In this section we use the artificial ground-motion dataset.

Each method is presented one at a time and algorithms for calculating fragility curves are proposed for each of them in the section belows.

(I) Fragility by Conditional-Spectrum Ground Motion Selection (CS-GMS)

Fragility calculations using this method involve two parts (1) ground motion selection of records to match a response acceleration spectrum conditional on a given level of the spectral acceleration $PSa^*(T_0, \zeta_0)$ and (2) calculation of probabilities of exceedance for multiple values of $PSa^*(T_0, \zeta_0)$.

Ground Motion Selection by Conditional Spectrum We can regard the response acceleration spectrum $PSa^{target}(T, \zeta_0)$ as a stochastic process with argument the period T and a parameter the damping ration ζ_0. The aim of ground motion selection process is to choose a set of ground motions from a large database, that match the second moment properties of the target acceleration spectrum $PSa^{target}(T, \zeta_0)|PSa^*(T_0, \zeta_0)$, conditioned on a spectral acceleration ordinate $PSa^*(T_0, \zeta_0)$ at a period of interest T_0 and damping ratio ζ_0. The value $PSa^*(T_0, \zeta_0)$ may be obtained from codes of practice or probabilistic seismic hazard analyses.

The method for selecting ground motions used in this study is introduced in [52, 42]. A brief description of the method for calculating the target spectrum and selecting the ground motion samples is presented in the following three steps.

Step 1: For a given probability of exceedance of a spectral acceleration, we can calculate a spectral ordinate $PSa^*(T_0, \zeta_0)$ from probabilistic seismic hazard analysis. Furthermore, conditional on the value $PSa^*(T_0, \zeta_0)$ of the spectral acceleration, we can calculate the joint distribution of the random vector $(M, R, \epsilon(T_0))$, where M is the moment magnitude, R is the source-to-site distance. Coordinate $\epsilon(T_0)$ is a standard normally-distributed random variable which accounts for the number of standard deviations between the logarithmic spectral acceleration of an observed record and the mean logarithmic spectral acceleration of a ground motion prediction model (GMPM) [7]. A ground motion prediction model is a statistical model, i.e., a regression model, which provides estimates of intensity measures given the moment magnitude, and source-to-site distance. The

calculations for finding the joint distribution and the marginal distributions of M, R and $\epsilon(T_0))$ is also known as *deaggregation* [11, 53]. The distributions of these three parameters $(M, R, \epsilon(T_0))$ may be obtained from the interactive deaggregation tool available on the United States Geological Survey's (USGS) website [72]. Finally, we can calculate the mean value of the moment magnitude $\overline{m} = \mathbb{E}[M]$ and the mean source-to-site distance $\overline{r} = \mathbb{E}[R]$ which may cause a value of the spectral ordinate $PSa^*(T_0, \zeta_0)$ at a site of interest.

Figure 4.6 shows the results of the deaggregation for Los Angeles, for a shear velocity $v_{30} = 620\ m/s$ in the top $30\ m$ of soil, and a probability of exceedance of $PSa^*(T_0, \zeta_0)$ of 2% in 50 years for $T_0 = 1\ s$ and $\zeta_0 = 5\%$ [72]. Each bar in the deaggregation plot represents the contribution of each combination of (M, R) to exceed $PSa^*(T_0, \zeta_0)$.

Step 2: Use $(\overline{m}, \overline{r})$ in a ground motion prediction model (GMPM) to calculate the mean and the standard deviation of the logarithmic response spectrum $\mu_{\ln PSa}(T, \overline{m}, \overline{r})$ and $\sigma_{\ln PSa}(T)$, respectively. The Campbell-Bozorgnia GMPM [12] was used for these calculations, but an approach on incorporating multiple GMPMs is presented in [52].

Then, under the assumption that the spectral acceleration values are log-normally distributed, the target response spectrum's mean and standard deviation are calculated [5]

$$\mu_{\ln PSa^{target}(T,\zeta_0)|PSa^*(T_0,\zeta_0)} = \mu_{\ln PSa}(T, \overline{m}, \overline{r}) + \rho(T, T_0)\overline{\epsilon}\sigma_{\ln PSa}(T) \tag{4.10}$$

$$\sigma_{\ln PSa^{target}(T,\zeta_0)|PSa^*(T_0,\zeta_0)} = \sigma_{\ln PSa}(T)\sqrt{1 - \rho^2(T, T_0)}, \tag{4.11}$$

where $\rho(T, T_0)$ is the correlation between $\epsilon(T_0)$ and $\epsilon(T)$ and is calculated empirically in [8] and [10].

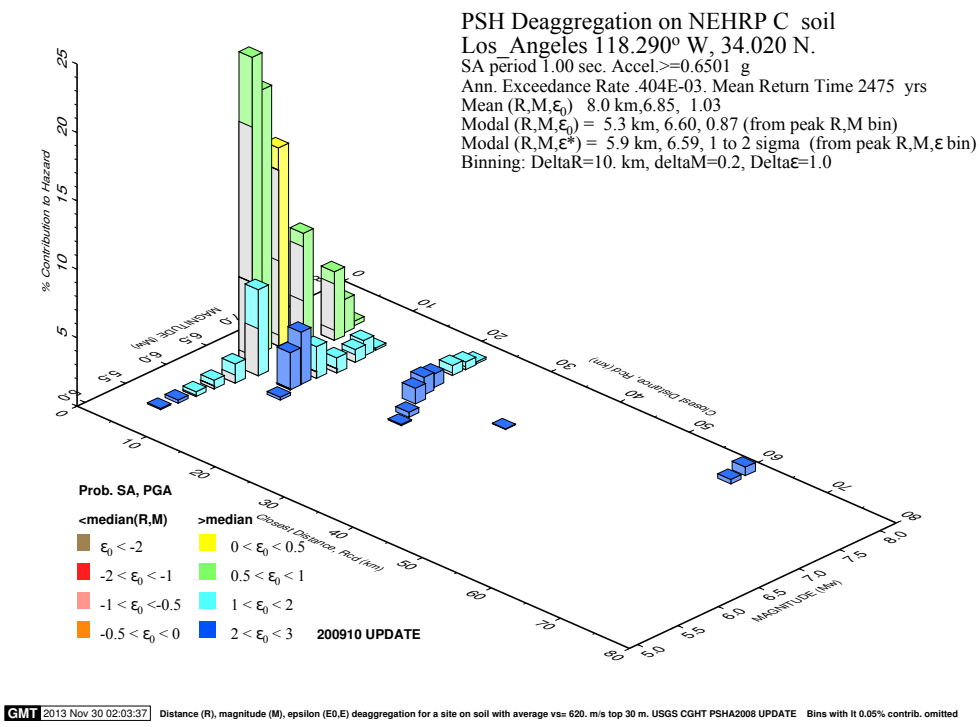

Figure 4.6: Snapshot from the USGS' deaggregation tool results for Los Angeles.

Step 3: Calculate the acceleration spectra for each record in the database, i.e., $PSa_i(T, \zeta_0)$. Select a number $\tilde{n}$ of records such that the differences between the mean and the standard deviation of the selected records' logarithmic response acceleration spectra and the mean and the standard deviation of the logarithmic target response acceleration spectrum $PSa^{target}(T, \zeta_0)|PSa^*(T_0, \zeta_0)$ are minimized.

Supporting software for the construction of the conditional spectrum and the ground motion selection is available at [36] and it was used for the selection of ground motion records in this paper.

Based on the deaggregation results shown in Fig. 4.6, on the value $PSa^*(1s; 5\%) = 0.65g$ and a probability of exceeding $PSa^*(1s; 5\%)$ of 2% in 50

years, $\tilde{n} = 40$ records are selected from the database with $N = 5000$ samples of the process $Z(t)$. The scaled versions of the response spectra $PSa_i(T, \zeta_0)$ for the selected records are shown in Fig. (4.7). Figure (4.8) shows the means and

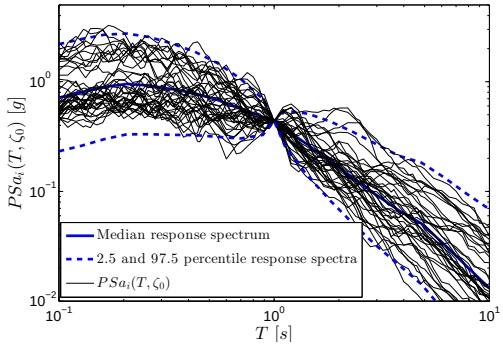

Figure 4.7: Spectral values of the artificial ground motions at $T_0 = 1\ s$ and $\zeta_0 = 0.05$.

the standard deviations of the target $\ln PSa^{target}(T, \zeta_0)|PSa^*(T_0, \zeta_0)$ and the estimated spectrum from the selected ground motions. Figures 4.7 and 4.8) were

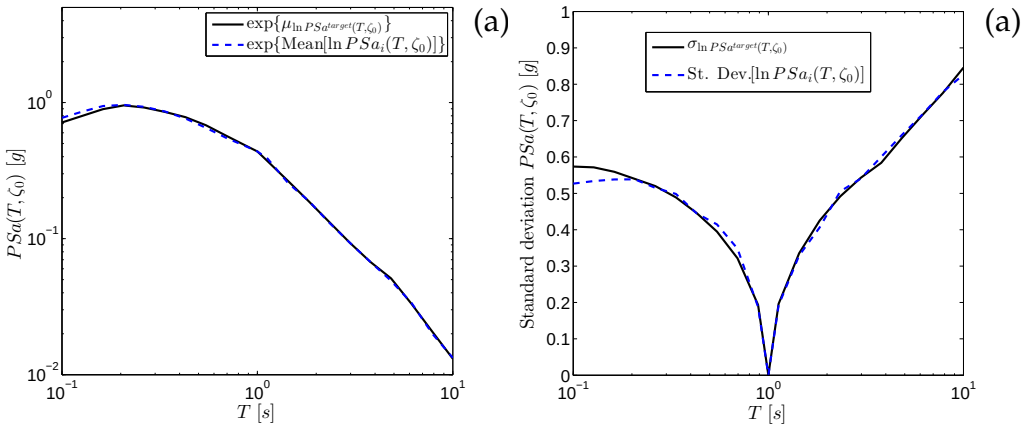

Figure 4.8: Target and estimated (a) mean and (b) standard deviation of the response acceleration spectra.

obtained using the software available on [36].

Fragility curves calculations This method is presented in [50] and the goal is to calculate fragility curves as functions of $PSa^*(T_0, \zeta_0)$. In the current example we use $n_{bin} = 36$ values for the conditioning value $PSa^*_j(T_0, \zeta_0)$, $j = 1, ..., n_{bin}$ corresponding to all values of exceeding probabilities available on the USGS website, that is, 1%, 2%, 5%, 10%, 20%, 50% in 21, 30, 50, 75, 100 and 200 years, respectively. We select sets of $\tilde{n}$ records for each value $PSa^*_j(T_0; \zeta_0)$, to match the response acceleration spectrum $\ln PSa^{target}(T, \zeta_0)|PSa^*(T_0, \zeta_0)$ as shown in the previous algorithm. The following steps are then used to calculate fragility curves.

Step 1: Select $z_{i,j}(t), i = 1, ..., \tilde{n}, \ j = 1, 2, ..., n_{bin}$ records for each $PSa^*_j(T_0, \zeta_0)$ and calculate the response $EDP_{i,j}$ using Eqs. (4.1) and (4.2).

Step 2: Fit a log-normal distribution for each set of $\tilde{n}$ $EDP_{i,j}$, with a cumulative distribution function $\mathbb{P}(EDP \leq \xi) = F_j(\xi; \mu_j, \sigma_j)$, where μ_j and σ_j are the mean and the standard deviation of the log-normal distribution, estimated from the data $EDP_{i,j}$.

Step 3: Approximate the probability of failure by

$$P_f\left(PSa^*_j(T_0, \zeta_0); \delta_{cr}\right) = 1 - F_j(\delta_{cr}; \mu_j, \sigma_j). \tag{4.12}$$

Fragility by Incremental Dynamic Analysis (IDA)

We assume that $\tilde{n}$ records $z_i(t), i = 1, ..., \tilde{n}$ are available at a site or have been selected by heuristic approaches. In the current example we select them by using the ground motion selection procedure presented before for a probability of 2% in 50 years. The scaled acceleration response spectra of these selected motions are shown in Fig. 4.7.

Step 1: Calculate the pseudo-spectral acceleration $PSa_i(T_0;\zeta_0)$ for each $z_i(t), i = 1,...,\tilde{n}$ and scale each record by its $PSa_i(T_0;\zeta_0)$, i.e., $z_i^*(t) = z_i(t)/PSa_i(T_0;\zeta_0), i = 1,...,\tilde{n}$.

Step 2: Multiply each record by increasing values $\xi > 0$ so that all records have the same pseudo-spectral acceleration level ξ.

Step 3: Calculate the response of the systems in Eqs. (4.1) and (4.2) $EDP_i^*(\xi)$ to the scaled ground motion samples $z_i^*(t) = \xi z_i(t)/PSa_i(T_0;\zeta_0), i = 1,...,\tilde{n}$.

Step 4: Estimate the probability of failure as

$$P_f(\xi;\delta_{cr}) = \frac{1}{\tilde{n}}\sum_{i=1}^{\tilde{n}} \mathbb{1}\{EDP_i^*(\xi) > \delta_{cr}\}. \tag{4.13}$$

Fragility by Using All Records Available (MC)

The method presented in this section uses all N samples $z_i(t),\ i = 1,...,N$ of the ground motion process $Z(t)$ in the dataset. The results in this approach are regarded as the reference for the comparison with the other methods. The following algorithm is used to construct the reference fragility curves.

Step 1: Calculate the spectral acceleration of each record, i.e.,$PSa_i(T_0,\zeta_0)$ for sample $z_i(t)$ of $Z(t)$.

Step 2: Divide the set of records in n_{bin} disjoint bins $\Psi_k, k = 1,...,n_{bin}$ according to their response acceleration spectra $PSa_i(T_0,\zeta_0)$. The number of bins is equal to the number of spectral acceleration values $PSa^*(T_0,\zeta_0)$ used for the calculation of the fragility curves using the GMS-CS method. Bins Ψ_k are constructed as a Voronoi tessellation $\{\Psi_k\} = \{z_i : \|PSa_i -$

$PSa_k^*\| \leq \|PSa_i - PSa_l^*\|,\ k \neq l\}$, where $k, l = 1, ..., n_{bin}$ and PSa_k^* correspond to the response spectral accelerations used for calculating the fragility curves with the GMS-CS method. Ordinates PSa_k^* are the nuclei of the Voronoi partitions Ψ_k. All spectral values PSa_i, PSa_k^*, PSa_l^* are calculated at period T_0 and for damping ratio ζ_0, but the notation was dropped for convenience. Figure 4.9 shows an example of the Voronoi cells for $n_{bin} = 11$, where the black circles represent the spectral acceleration values for each record in the dataset and the solid lines mark the boundaries between each cell.

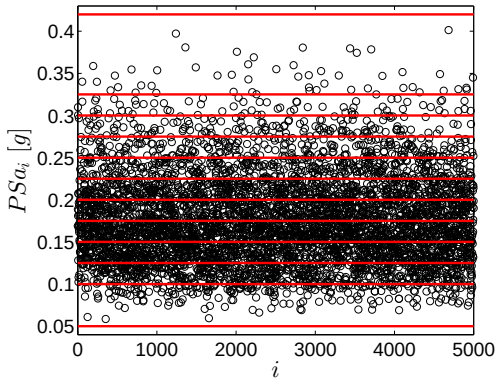

Figure 4.9: Spectral acceleration values $PSa_i(T_0, \zeta_0)$ for all ground motions in the dataset

Step 3: Calculate EDP_i for each record $z_i(t)$ in Ψ_k. Estimate the probability of failure by

$$P_f(PSa_k^*; \delta_{cr}) = \frac{1}{n_k} \sum_{i=1}^{n_k} \mathbb{1}\{EDP_i > \delta_{cr} | z_i(t) \in \Psi_k\}, \tag{4.14}$$

where PSa_k^* is the center of the Voronoi cell Ψ_k and n_k is the number of samples in Ψ_k.

The accuracy of the method increases as the number of samples N increases.

4.3.3 Numerical Results

Fragility curves are calculated using the classes of methods shown above for the structural systems presented in Eqs. (4.1) and (4.2). Results are shown and compared in the following figures. Fragility curves calculated with all three methods are obtained for the same values of the response acceleration spectral ordinates $PSa_j^*(T_0, \zeta_0)$, as defined previously. The reference results are obtained by using all samples N in the dataset. The IDA method uses only $\tilde{n} = 40$ records which are scaled to have common increasing response spectral accelerations $PSa_j^*(T_0, \zeta_0)$. In the case of CS-GMS method we use n_{bin} sets of $\tilde{n} = 40$ records to match the response acceleration spectrum conditioned on $PSa_j^*(T_0, \zeta_0)$. The number of points on the fragility curves is equal to the number of exceeding probabilities available on the USGS' deaggregation tool, which define the values $PSa_j^*(T_0, \zeta_0)$.

Figures 4.10 and 4.11 show fragility curves defined as $\mathbb{P}(EDP > \delta_{cr}|PSa(T_0, \zeta_0))$, where $\delta_{cr} = 2.5 \times 10^{-3}$ is the critical value for the engineering design parameter EDP for the systems described previously.

Figures 4.10 (a) and (b) show fragility curves for the linear systems. All three methods estimate accurately the fragility for the SDOF linear system (Figure 4.10 (a)), which hast the analytical form $P_f(\xi; \delta_{cr}) = \mathbb{1}\{\xi > 4\delta_{cr}\pi^2/T_0^2\} \simeq \mathbb{1}\{\xi > 0.1\}$ [44]. The IDA and CS-GMS methods fail to produce comparable results with the ones obtained by using all records in the cases of the linear 2DOF system shown in Figure (b). The two modes of vibration have comparable distributions in the total response of the 2DOF system and, therefore, the response significantly different than the one of a linear SDOF. The results of the three methods are different of each other for the non-linear systems. Even though the

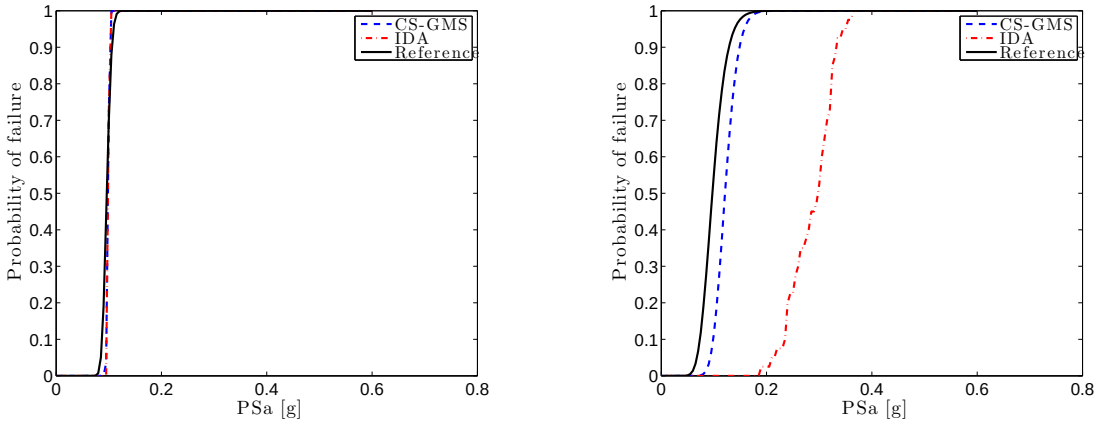

Figure 4.10: Fragility curves for (a) linear SDOF and (b) linear 2DOF systems

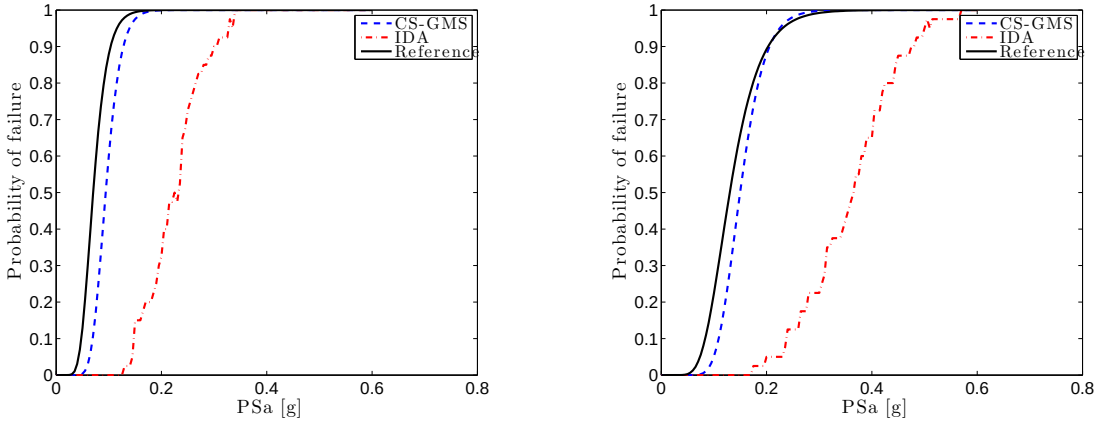

Figure 4.11: Fragility curves for (a) Bouc-Wen SDOF and (b) Bouc-Wen 2DOF systems

fragility curves calculated by the reference method and ground motion selection seem similar in Figure 4.11, the differences are significant. For example, in the case of the SDOF Bouc-Wen, for a fixed value of the $PSa(T_0; \zeta_0) = 0.06\ g$ the probabilities of failure in the Monte-Carlo and ground motion selection methods are approximately 30% and 3%, respectively.

4.4 Fragility Curves by SROM-based Ground Motion Selection

A new methodology is proposed for calculating fragility curves using exclusively actual ground motion records. Ideally, one would calculate fragility curves by using all records available in a dataset, but the procedure would be computationally expensive. Current methods select a limited number of records from large datasets using heuristic methods. The most common method is based on conditional spectrum (CS-GMS) and was presented in the previous section. Unlike The CS-GMS method, which selects ground motion samples by matching a target response spectrum, the methodology proposed selects samples representative for the entire dataset available.

Numerical examples for the ground-motion selection method proposed are shown using the PEER NGA dataset in order to show explicitly how the method can be applied for real records.

4.4.1 Modified PEER NGA Dataset

The methodology proposed selects ground-motion records from a large dataset considering estimates of the probability law of the ground-motion process, rather than just looking at response-spectra values. Large databases, such as PEER NGA, are composed of thousands of ground-motion records $z_i^o(t)$ with different durations, frequency contents and intensities. This large variation of parameters among the records makes unreasonable the assumption that all records are samples of the same ground-motion process.

We propose the following, rather, ad-hoc method to modify the original

samples such that the assumption that they are samples of the same process is reasonable. We assume that the strong motion part of $z_i^o(t)$ has duration $\tau_i,\ i = 1, ..., N$ and is the sample of a stationary process, where N is the total number of records in the dataset. Under this assumption, we can define $z_i(t)$ with duration $\tau = \max_i(\tau_i)$ for each $z_i^o(t)$ by connecting the strong motion part of $z_i^o(t)$ multiple times until it reaches the duration τ, without changing either its intensity or frequency content.

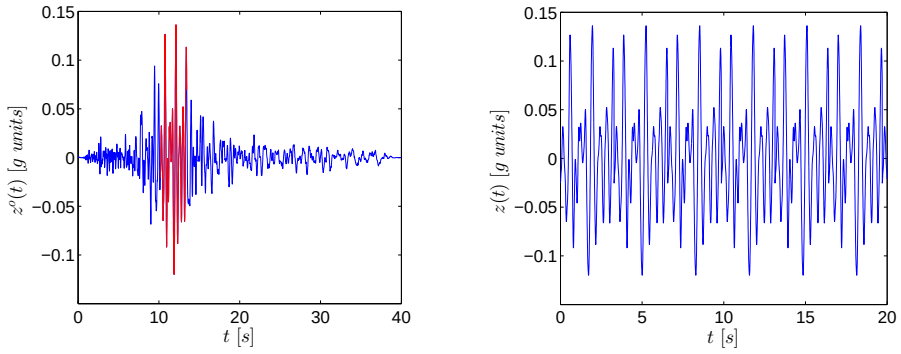

Figure 4.12: (a) Original record from PEER (b) Modified record from PEER

The process of obtaining $z_i(t)$ for each $z_i^o(t)$ is illustrated in Figure 4.12. In part (a) a sample of a record in PEER is shown and its strong-motion part is marked in red. The length of the strong motion part of these records is defined in terms of Arias intensity, i.e. $I_i = \int z_i^o(t)dt$. In this case we consider the length of the strong motion part of $z_i^o(t)$ to be between $20\%I_i$ and $80\%I_i$ as shown in Figure 4.13.

Figure 4.12 (b) shows the resulting $z_i(t)$ obtained by attaching the strong motion part in (a) repeatedly until the duration $\tau = 20\ s$ is obtained.

In order to facilitate the calculation of fragility curves as functions of spectral acceleration PSa_k^*, we split the records $z_i^o(t),\ 0 \leq t \leq \tau_i\ i = 1, ..., n$ in bins Ψ_j

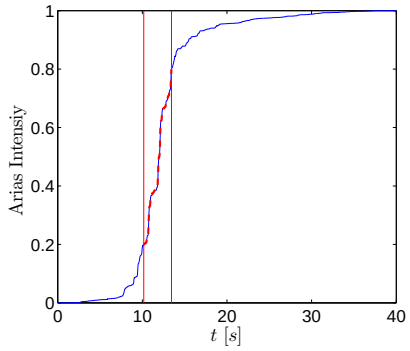

Figure 4.13: Arias intensity and 20% and 80% limits

by using a Voronoi tessellation as done for the reference method previously. A partition $\{\Psi_k\} = \{z_i^o(t) : \|PSa_i - PSa_k^*\| \leq \|PSa_i - PSa_l^*\|,\ k \neq l\}$, where $k, l = 1, ..., n_{bin}$ and PSa_i is the response spectral acceleration at at period T_0 and for damping ratio ζ_0 for record $z_i^o(t)$. Ordinates PSa_k^* are the nuclei of the Voronoi partitions Ψ_k. All spectral values are calculated at period T_0 and for damping ratio ζ_0. Further more, we assume that samples $z_i(t)$ corresponding to records in each cell Ψ_k are samples of the same stationary process. We denote by n_k the number of record in cell k, such that $\sum_k n_k = n$.

4.4.2 Ground motion selection by stochastic reduced order models

We propose an alternative to selecting ground motion records based on the conditional spectrum [50, 5]. The proposed method selects records based on the probability law of the ground motion records in a dataset, and not on the spectral response values. It was shown in the previous section that selecting motions by looking at spectral values of the response of single-degree-of-freedom

systems may lead to unsatisfactory results for multi-degree-of-freedom or non-linear systems. The method proposed assures that the records selected are consistent with the probabilistic characteristics of all records available in the dataset.

Stochastic Reduced Order Models (SROM)

The new method proposed for selecting ground-motion records uses stochastic reduced order models (SROM) [28]. SROM are built with random samples from the dataset selected in an optimal manner. We will use the modified dataset for the selection of ground motions, that is, stationary samples with the same duration.

We assume that records $z_i(t),\ i = 1, ..., n_j$ in bin j, that is, the pseudo-spectral accelerations $PSa_i(T_0, \zeta)0)$ of their original images $z_i^o(t)$ belong to the cell Ψ_j, are samples of the same process $Z_j(t)$. The goal is to select a small number $\tilde{n}$ of records $z_i(t)$ representative for the process $Z_j(t)$. For simplicity we will drop index j. A stochastic process $\tilde{Z}(t)$ with $\tilde{n}$ samples $\{\tilde{z}_k(t),\ k = 1, ..., \tilde{n}\}$ of $Z(t)$ which are weighed by some weights $\{p_k(t),\ k = 1, ..., \tilde{n}\}$ such that $\sum_{k=1}^{\tilde{n}} p_k = 1$ is called a stochastic reduced order model of $Z(t)$. The samples and their probabilities $\{\tilde{z}_k(t), p_k\}$ define completely the probability law of $\tilde{Z}(t)$.

To construct $\tilde{Z}(t)$ we select at specified number $\tilde{n}$ of samples of $Z(t)$ and calculate the differences between probability laws of $Z(t)$ and $\tilde{Z}(t)$. The set of $\tilde{n}$ samples and their probabilities that minimizes these discrepancies define the SROM of $Z(t)$. We define the metric

$$e(\mathbf{p}) = \theta_1 e_1(\mathbf{p}) + \theta_2 e_2(\mathbf{p}) + \theta_3 e_3(\mathbf{p}) \tag{4.15}$$

where (1) function $e_1(\mathbf{p})$ defines the differences between q-th oder moments $\tilde{\mu}(q;\mathbf{p}) = \mathbb{E}[\tilde{Z}(t)]$ and $\mu(q) = \mathbb{E}[Z(t)]$; (2) function $e_2(\mathbf{p})$ defines the differences between the marginal distributions $\tilde{F}(x;\mathbf{p}) = \mathbb{P}[\tilde{Z}(t) \leq x]$ and $F(x) = \mathbb{P}[Z(t) \leq x]$; (3) function $e_3(\mathbf{p})$ defines the differences between the correlation functions $\tilde{\rho}(\tau;\mathbf{p}) = \mathbb{E}[\tilde{Z}(t)\tilde{Z}(t+\tau)]$ and $\rho(\tau) = \mathbb{E}[Z(t)Z(t+\tau)]$ of $\tilde{Z}(t)$ and $Z(t)$, respectively and (4) coefficients $\theta_i,\ i = 1, 2, 3$ are some weights which define the relative importance of e_1, e_2 and e_3. Functions $\tilde{\mu}(q;\mathbf{p})$, $\tilde{F}(x;\mathbf{p})$ and $\tilde{\rho}(\tau;\mathbf{p})$ are estimated from the samples of the SROM, i.e. $\{\tilde{z}_k(t), p_k\}$. Functions $\mu(q)$, $F(x)$ and $\rho(\tau)$ related to the probability law of $Z(t)$ are estimated from all samples available.

For each set of $\tilde{n}$ independent samples of $Z(t)$, a vector $\mathbf{p}$ is calculated to minimize the objective function $e(\mathbf{p})$. The selection is repeated for a specified number of times and the samples and probabilities $\{\tilde{z}_i^{opt},\ p_i^{opt}\}$ for which the minimum value of $e(\mathbf{p^{opt}})$ is obtained are used in the dynamic analysis. The solution of the SROM selection $\{\tilde{z}_i^{opt},\ p_i^{opt}\},\ i = 1, ..., \tilde{n}$ is a sub-optimal solution since the selection is performed for a specified number of times. An optimal solution could be obtained if the objective function $e(\mathbf{p})$ was calculated for all combinations of $\tilde{n}$ independent samples of $Z(t)$ in cell j.

Fragility calculation (SROM-GMS)

The algorithm for calculating fragility curves using the SROM-based ground motion selection is similar to the CS-GMS method presented previously. The only difference relates to the way the ground motions are selected.

Fragility curves calculations The algorithm is presented below for each bin j.

Step 1: Select $z_k^{opt}(t), k = 1, ..., \tilde{n}$ from bin j and calculate their corresponding probabilities $p_k^{opt}(t), k = 1, ..., \tilde{n}$.

Step 2: Perform the dynamic analysis for each ground motion z_k^o corresponding to each sample $z_k^{opt}(t), k = 1, ..., \tilde{n}$ selected by SROM. Calculate the corresponding engineer design parameters EDP_k.

Step 3: Estimate the probability of failure by

$$P_f(PSa_j; \delta_{cr}) = \sum_{k=1}^{\tilde{n}} \mathbb{1}\{EDP_k > \delta_{cr}\} p_k^{opt}, \tag{4.16}$$

where PSa_j is the mean response spectral acceleration of the records in bin j.

Note that even though the method uses just the strong motion part to select the ground motion records from the dataset, we use the corresponding original records for the dynamic analyses.

To validate this newly proposed method, we calculate the fragility curves for the two systems driven by the Eqs. 4.1 and 4.2. Results are calculated using three methods, that is, the reference method and the two methods based on ground motion selection using conditional spectrum (CS-GMS) and stochastic reduced order models (SROM-GMS), respectively. We used all N record in the MC analysis, and equal number of records for the other two methods. For the conditional spectrum selection (CS-GMS) method we used $\tilde{n} = 30$ records selected for 15 distinct values the intensity measure $PSa(T_0, \zeta_0)$, totaling a number of 450 redords. For the SROM selection method we split the records in $n_{bin} = 15$ bins and we selected $\tilde{n} = 30$ records from each of them.

Figure 4.14(a) shows the fragility curves for the SDOF linear system calculated by all three methods. All methods agree with the analytical result, which

is a step function $\mathbb{1}\{\xi > 0.1\}$, as indicated previously. Figure 4.14(b) shows fragility curves for the SDOF Bouc-Wen system. The method proposed matches very well the results provided by the MC method. For the method based on conditional spectrum, we calculated three different fragility curves for different sets of $PSa(T_0, \zeta_0)$ values. All three CS-GMS fragility curves are different than each other and do not match the MC results.

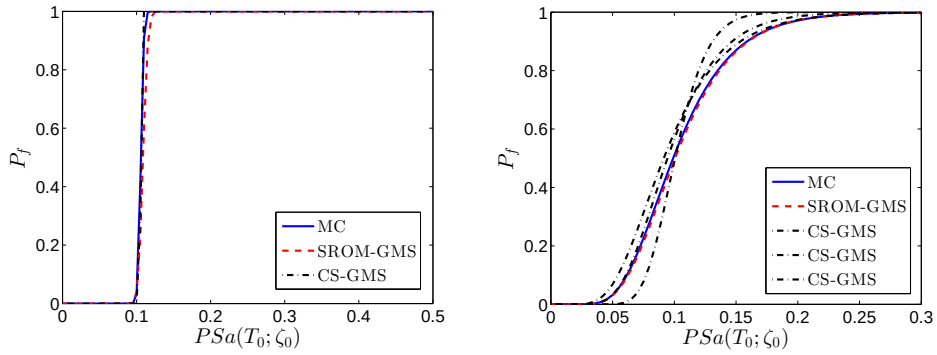

Figure 4.14: Fragility curves for (a) Linear SDOF system and (b) Bouc-Wen SDOF system

4.5 Conclusions

Fragility curves are graphical representations of probabilities that the response of systems exceed critical values, under ground accelerations of specified intensity measures. Two aspects of seismic response of structural systems have been investigated in this paper.

The first relates to limitations to current approaches used in fragility analysis. It was shown that the characterization of seismic ground intensity by peak ground acceleration and ordinates of response spectra provides insufficient details about the time histories of ground shaking for constructing accu-

rate fragilities. Probabilities of structures exceeding limit responses subjected to ground motions with the same peak ground accelerations or response spectral ordinates can differ significantly. Fragility curves are calculated by ground motion selection using a target response spectrum and by incremental dynamic analysis and are compared with fragility curves calculated by using all ground motion records available. Both methods produce accurate fragility curves for the single-degree-of-freedom linear systems but they fail to produce consistent fragility curves for multi-degree-of-freedom and non-linear systems.

The second part of this chapter proposes a novel method for selecting ground motion records for dynamic analysis. The new method is based on stochastic reduced order models (SROM). Unlike the selection method based on the conditional spectrum, the SROM-based method selects records in an optimal way such that they match the probability law of the ground motion process, rather than matching a response spectrum. Fragility curves calculated using records selected in this manner give satisfactory results for non-linear systems and consistent with fragility curves calculated using all records available.

CHAPTER 5

STRUCTURAL PERFORMANCE BY FRAGILITY SURFACES FOR SIMPLE SYSTEMS UNDER NON-GAUSSIAN INPUT

5.1 Introduction

Seismic fragility is commonly used to measure seismic performance of structures and estimates the probability of reaching or exceeding different states of damage for a given level of ground shaking [40]. Fragility curves are graphical representations of seismic fragility and they describe the relationship between earthquake hazard and the structural response. Traditionally, fragility curves are used in performance seismic design as functions of scalar seismic intensity measures. Peak ground acceleration [40, 67, 64, 14, 21, 66] and pseudo-spectral acceleration [23, 49, 17, 51, 44] are among the most widely-used intensity measures in fragility analysis.

Generally, fragility curves are constructed by scaling ground motion records and by selecting samples of ground motions for increasing intensity levels from existing databases. The most popular approach, known as incremental dynamic analysis, involves repeated scaling of seismic ground motions to increasing intensity measures until the specified damage state is reached [73, 75, 26]. The other method for calculating fragility curves, known as multiple stripes analysis [50, 6], uses selected ground motion records from a large dataset consistent with the level of a spectral value of the response [54, 5]. The log-normal cumulative distribution function is commonly used as a parametric model for fragility curves [68, 4, 41]. This model is also adopted by the Federal Emergency Management Agency (FEMA) through ATC-58 [57, 3]. Various methods have been

proposed to estimate the parameters of the log-normal distribution from data [45, 6].

Constructing fragility curves may be attractively simple, but they have limitations. Recent studies have shown that fragilities viewed as functions of a scalar seismic iinensity measure ca be unsatisfactory. It was shown in [34] that response statistics calculated for a nonlinear system subjected to different ground motion processes, indistinguishable with respect to their peak ground accelerations or by ordinates of response spectra, can yield significant differences. Moreover, scaling ground motions is conceptually simple but may yield unsatisfactory fragilities [44] for certain nonlinear systems. Scaling only changes the intensity of the ground motions, and the ground motions used to construct fragilities have the same frequency content irrespective of their intensity [30]. Alternative vector-valued seismic intensity measures were proposed in [9, 7, 70]. Plots of seismic fragilities calculated for ground motions characterized by two or more intensity measures are called fragility surfaces. Fragility surfaces provide the same information as fragility curves, that is, they are graphical representations of seismic fragilities, but are calculated as functions of two-dimensional vector-valued intensity measures [22]. For example, fragility surfaces have been constructed as functions of the peak ground displacement and peak ground acceleration [65], or spectral displacement ordinates at two distinct periods [24].

In the first part of this chapter, we propose a vector intensity measure with components the moment magnitude m and source-to-site distance r for fragility analysis [44]. The analysis is performed for ground motion records characterized by (m, r). Since the number of available records at a site is insufficient to

calculate values of the fragility surface at each (m, r) coordinate, we use simulated ground motion records. A regional seismological model which uses the specific barrier model [37] allows the simulation of ground motion samples as a function of (m, r). A Bayesian method was proposed in [62] to update the model with site records, in order to allow simulation of site-specific ground motion samples. Calculating fragility surfaces is computationally expensive, since it is based on response analyses of structures subjected to seismic ground motions characterized by various values of (m, r). To overcome this drawback, we propose efficient methods for calculating fragility surfaces based on stochastic reduced order models [61, 28]. The stochastic reduced order model (SROM) resembles the Monte-Carlo method. Like Monte-Carlo, the method calculates structural responses to samples of the ground-motion process. Unlike Monte-Carlo, which uses a large number of samples selected at random, the proposed method uses a small number of samples selected in an optimal way. Similarly to the method adopted by the ATC-58 in which a log-normal distribution function is adopted as a model for fragility curves, a parametric bi-variate log-normal cumulative distribution function is used as a parametric model for fragility surfaces. Fragility surfaces are essential tools in performance-based seismic design and are used to estimate the life-cycle damage and cost of structures subjected to seismic loads.

The second part of this study proposes a framework for estimating probability distributions of metrics which characterize the performance of structures under seismic loads. Metrics such as life-cycle cost and downtime are used to evaluate the life-cycle performance of structures. Distributions of these metrics are obtained by Monte Carlo simulations of seismic hazard scenarios for the life-cycle of the structure. Parametric models are assumed for the cost functions

and a damage model constructed as a regenerative processes under several assumptions are used in the development of this framework.

Numerical results are presented for fragility surfaces calculated for simple linear and non-linear systems at a site in Southern California. The seismic performance of systems is assessed through cost and damage estimates calculated by using simulated life-cycle scenarios. The method proposed allows the calculation of distribution of life-cycle estimates rather than just mean values, which gives important information used by governmental agencies, decision makers, (re)insurance industry etc.

5.2 Problem Definition

Our goal is to calculate life-cycle estimates for structures subjected to seismic loads. The seismic ground motion is assumed to be a stochastic process and linear and non-linear structural models are used to illustrate the methodology proposed for the evaluation of seismic performance of structures.

5.2.1 Seismic ground motion

We define the seismic ground motion records at a site, produced by a seismic event with magnitude m and source-to-site distance r as samples of a stochastic process $A(t)$. Statistics of actual ground motion records show that strong ground motion part of the seismic ground acceleration records has kurtosis coefficient greater than 4 [43]. Since the kurtosis coefficient for Gaussian processes is 3, we assume that the ground motion process $A(t)$ is a zero-mean, non-stationary,

non-Gaussian process given by

$$A(t) = h(t)Z(t),\ 0 \leq t \leq t_f, \tag{5.1}$$

where t_f is the duration of the record,

$$h(t) = \alpha t^{\beta} \exp\{-\gamma t\} \tag{5.2}$$

is a deterministic envelop function with constant parameters α, β and γ. The process $Z(t)$ is a zero-mean, stationary, non-Gaussian process with marginal distribution $F_Z(z) = \mathbb{P}(Z(t) \leq z)\ , \forall 0 \leq t \leq t_f$. It is assumed that the marginal density of $Z(t)$ is Student's t, defined by

$$f_Z(x) = \frac{\Gamma(\frac{n+1}{2})}{\Gamma(\frac{n}{2})\sigma\sqrt{\pi n}} \left(1 + \frac{1}{n}\left(\frac{x-\mu}{\sigma}\right)^2\right)^{-\frac{n+1}{2}} \tag{5.3}$$

is the probability density function for the Student's t distribution $T(\mu, \sigma, n)$ with mean μ, variance $n\sigma^2/(n-2)$ and n degrees of freedom. The three parameters μ, σ and n of this distribution are estimated from the (m, r)-dependent second moment properties and the kurtosis estimated from data.

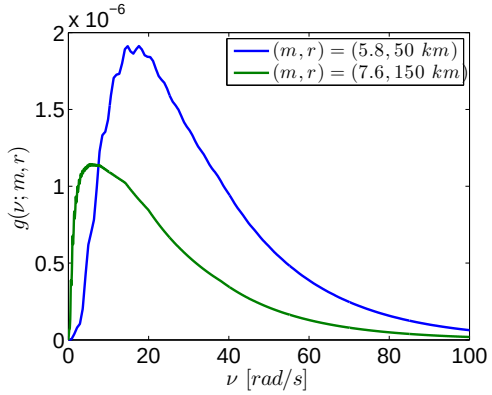

Figure 5.1: Power spectral density for $(m, r) = (5.8, 50\ km)$ and $(m, r) = (7.6, 150\ km)$.

The second-order moment properties of process $Z(t)$ are given by the one-sided spectral density function $g(\nu; m, r)$. Function $g(\nu; m, r)$ is given by the

specific barrier model [37] and depends on the parameters (m, r). Constants α, β, γ and the duration t_f in Eqs. (5.1) and (5.2) are also outputs of the specific barrier model. Figure 5.1 shows the power spectral density functions for $(m, r) = (5.8, 50\ km)$ and $(m, r) = (7.6, 150\ km)$, respectively. Important differences in the frequency content of the two processes are noticed as parameters (m, r) change. An average value of 5.67 for the kurtosis coefficient has been estimated by the United States Geological Survey estimated for ground motion records for a class-B soil, i.e., general rock with a shear velocity $v_{30} = 620\ m/s$ in the top $30\ m$ of soil [43].

We propose to generate samples of the process $Z(t)$ by using a monotonic memoryless transformation model ([27], Section 3.1) of the form

$$Z(t) = F_Z^{-1} \circ \Phi(G(t)) \tag{5.4}$$

where (1) F_Z^{-1} denotes the inverse of the marginal distribution function F_Z, (2) $\Phi(x) = \int_{-\infty}^{x} \phi(y)dy$ is the standard Gaussian marginal distribution, with the probability density $\phi(x) = \left(\sqrt{2\pi}\right)^{-1} \exp\{-x^2/2\}$ and (3) $G(t)$ is the zero-mean, unit-variance, stationary Gaussian image of $Z(t)$ with spectral density function $g(\nu; m, r)/\sigma^2$, where $\sigma^2 = \int_0^{\infty} g(\nu; m, r)d\nu$. The approximation that the spectral density of $G(t)$ is just a scaled version of $g(\nu; m, r)$ is based on the observation that the differences between the correlation in the non-Gaussian space and the corresponding on the Gaussian space are not significant for a broad range of values ([27], Section 3.1). Note that processes $Z(t)$ and $G(t)$ depend on (m, r), but the indication of (m, r) is not carried along for the simplicity of notation.

Let $Z_G(t)$ be the Gaussian image of $Z(t)$ with the same second-order moment properties given by $g(\nu; m, r)$. Even though processes $Z(t)$ and $Z_G(t)$ have the same second-order moment properties, the differences provided by

considering the kurtosis from data in $Z(t)$ may be significant. Figure 5.2(a) shows a samples of $Z(t)$ and its correspondence in the Gaussian space $Z_G(t)$ for $(m, r) = (5.8, 50\ km)$. Higher peaks are present in the $Z(t)$ sample, which are consistent with the tail distributions of $Z(t)$ and $Z_G(t)$ shown in Figure 5.2(b).

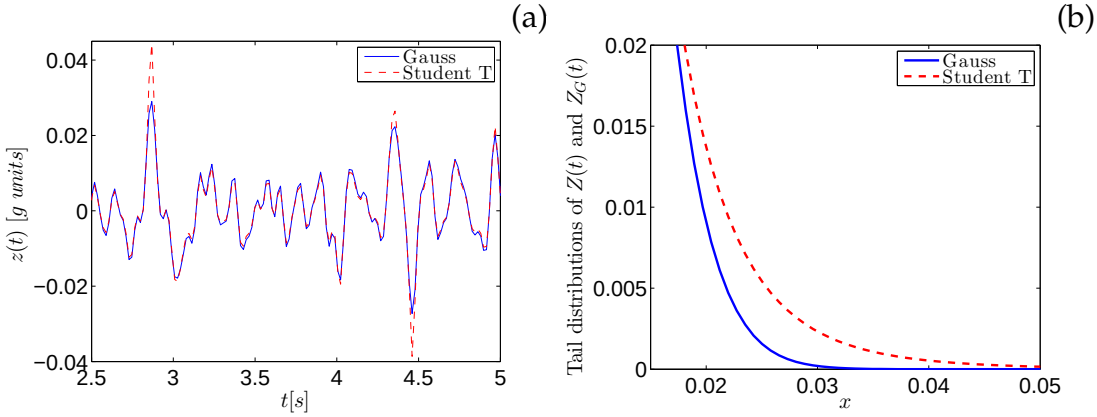

Figure 5.2: (a) Comparison between a sample $z(t)$ from the Student's t distributed process and its Gaussian image, (b) Marginal distribution functions for process $Z(t)$ and its Gaussian image $G(t)$.

Further more, we calculate the mean crossing rates $\eta_Z(z)$ and $\eta_G(z)$ at which processes $|Z(t)|$ and $|Z_G(t)|$ exceed value z, respectively ([69], Section 7.3).

$$\eta_Z(z) = \frac{\dot{\sigma}}{2\pi\sigma} \exp\left\{-\frac{1}{2}\left[\Phi^{-1} \circ F_Z(z)\right]\right\} \tag{5.5}$$

$$\eta_G(z) = 2\frac{\dot{\sigma}}{\sigma\sqrt{2\pi}}\phi\left(\frac{z}{\sigma}\right), \tag{5.6}$$

where $\sigma^2 = \int_{\nu\geq 0} g(\nu; m, r)d\nu$ and $\dot{\sigma}^2 = \int_{\nu\geq 0} \nu^2 g(\nu; m, r)d\nu$ are the variances for processes $Z_G(t)$ and $dZ_G(t)/dt$, respectively. Figure 5.3 shows the mean crossing rates $\eta_Z(z)$ and $\eta_G(z)$ for processes $Z(t)$ and $Z_G(t)$, respectively, for $(m, r) = (5.8, 50\ km)$. The graph indicates that the two processes have almost identical rates of crossing low values of z, but the mean crossing rate of process $Z(t)$ is higher as z increases, which is explains the high peaks shown in Figure 5.2(a).

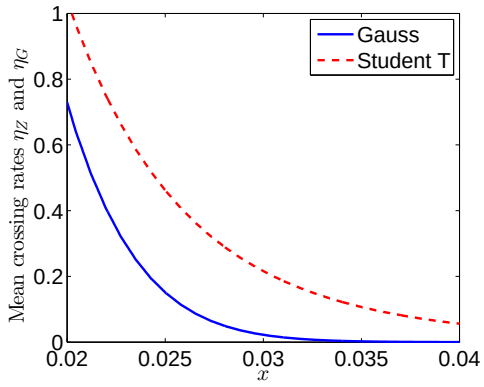

Figure 5.3: Mean crossing rates for processes the Student's t-distributed process $Z(t)$ and its Gauss image $G(t)$, for $(m, r) = (5.8, 50\,km)$.

Finally, Figure 5.4 shows two samples of the ground motion process $A(t)$ in Eq. (5.1) for the two spectral densities shown in Figure 5.1.

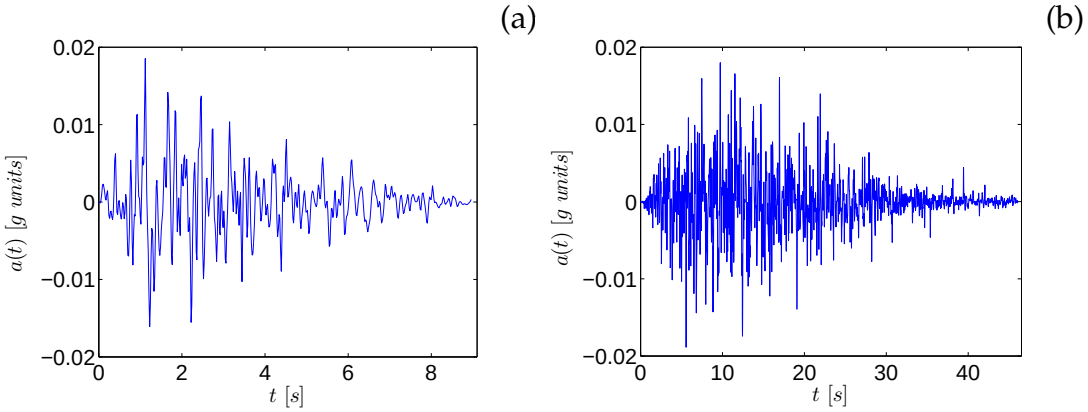

Figure 5.4: Samples of the ground motion process $A(t)$ for (a) $(m, r) = (5.8, 50\,km)$ and (b) $(m, r) = (7.6, 150\,km)$.

5.2.2 Structural systems

Let $X(t)$ be the relative displacement of a single-degree-of-freedom system subjected to the seismic ground acceleration $A(t)$. For the linear and the Bouc-Wen

systems, $X(t)$ satisfies the following equations respectively:

$$\ddot{X}(t) + 2\zeta_0\nu_0\dot{X}(T) + \nu_0^2 X(t) = -A(t) \tag{5.7}$$

$$\ddot{X}(t) + 2\zeta_0\nu_0\dot{X}(T) + \nu_0^2(\rho X(t) + (1-\rho)W(t)) = -A(t)$$

$$\dot{W}(t) = \gamma\dot{X}(t) - \alpha|\dot{X}(t)||W(t)|^{n-1}W(t) - \beta\dot{X}(t)|W(t)|^n, \tag{5.8}$$

where $\nu_0,\ \zeta_0,\ \rho,\ \alpha,\ \beta,\ \gamma,\ n$ are system parameters and $W(t)$ in Eq. (5.8) is the hysteretic displacement. Numerical results are shown for $\nu_0 = 2\pi\ rad/s$, $\zeta_0 = 0.02$, $\rho = 0.15$, $\alpha = 0.001$, $\beta = 2$, $\gamma = 4$ and $n = 1$. Note that for $\rho = 1$, the Bouc-Wen system becomes identical with the linear system.

The behaviors of the two systems in Eqs. (5.7) and (5.8) are shown in Figures 5.5 (a) and (b), in which the restoring force $\nu_0^2 X(t)$ and the hysteretic restoring force $\nu_0^2 W(t)$ are plotted for a sample $a(t)$ of $A(t)$.

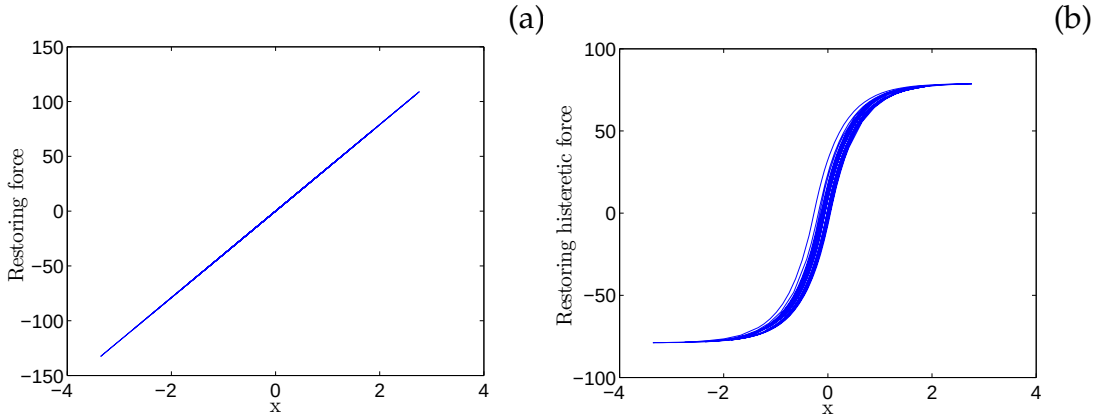

Figure 5.5: Dynamic behavior (backbone curve) for (a) the linear and (b) the Bouc-Wen structural systems subjected to a sample of $A(t)$.

5.3 Fragility Surfaces

Fragility surfaces $P_f(m,r)$ are graphical representations of probabilities $P_f(m,r) = \mathbb{P}\left(\max_{0\leq t\leq t_f}|X(t)| > x_{cr}\right)$ that a structural response $X(t)$ reaches or exceeds a critical limit under a seismic ground motion $A(t)$ corresponding to moment magnitude m and source-to-site distance r. Monte-Carlo (MC) is the only general method for calculating response statistics. The following algorithm can be used to calculate fragility surfaces for a structural system.

(1) Generate N samples $a_i(t),\ i = 1, ..., N$ of the seismic ground motion process $A(t)$ in Eq. (5.1) for fixed (m,r);

(2) Calculate samples of response $x_i(t),\ i = 1, ..., N$ for the structural system in Eq. (5.7) or (5.8) subjected to $a_i(t)$;

(3) Calculate the value of the fragility surface at coordinates (m,r) for a specified critical limit for the displacement x_{cr}

$$P_f(m,r) = \frac{1}{N}\sum_{i=1}^{N}\mathbb{1}\{\max_{0\leq t\leq t_f}|x_i(t)| > x_{cr}\}, \tag{5.9}$$

where $\mathbb{1}$ is the indicator function, i.e. $\mathbb{1}\{x > x_0\} = 1$ if $x > x_0$ and zero otherwise.

The algorithm described above gives a method to construct fragility surfaces for the maximum displacement of a simple single-degree-of-freedom system. The same procedure is applicable to any other system for any desired engineering design parameter (e.g. inter-storey drift, angle of rotation etc.). Figures 5.6 (a)-(d) show fragility surfaces calculated for the Bouc-Wen system in Eq.(5.8) for increasing demand $x_{cr} = \{0.5, 1, 2, 8\}\ cm$.

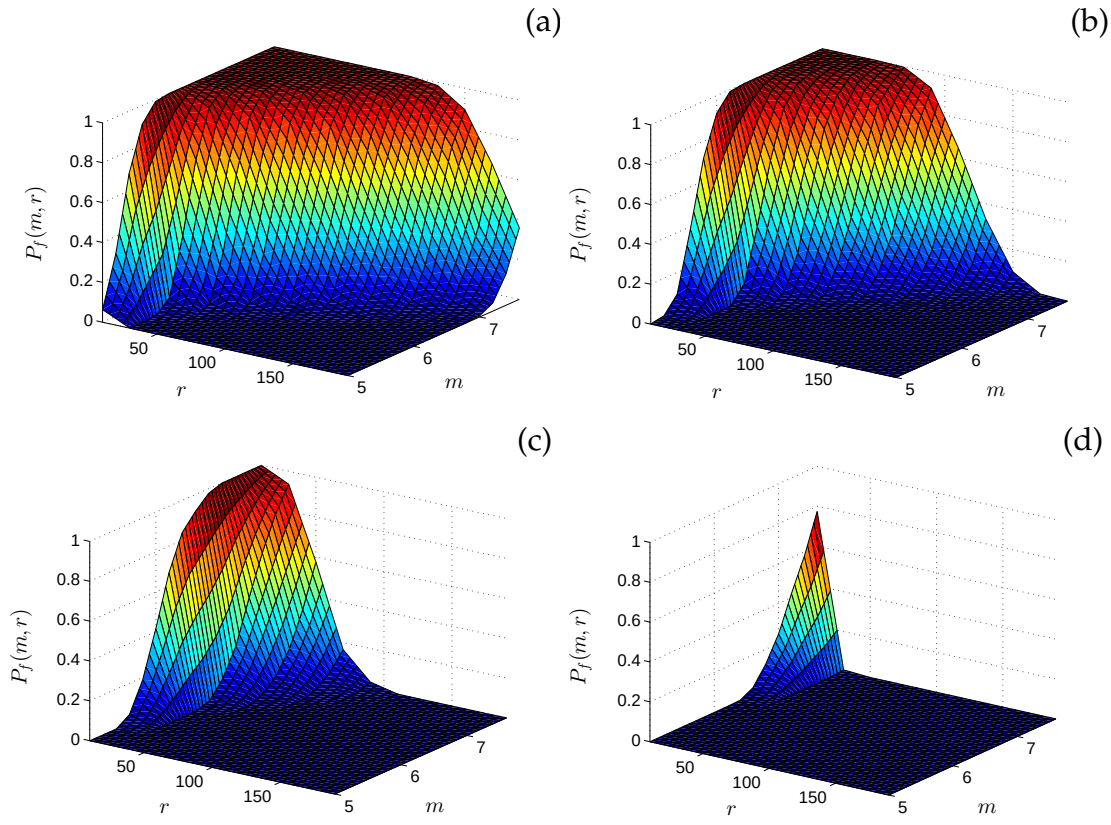

Figure 5.6: Evolution of fragility surfaces with increasing demand: (a)$x_{cr} = 0.5\ cm$, (b)$x_{cr} = 1\ cm$, (c)$x_{cr} = 2\ cm$, (d)$x_{cr} = 8\ cm$.

Monte-Carlo simulation usually requires a large number N of samples for the analysis. Since fragility surfaces are calculated by response analyses, their construction could be computationally expensive for complex structural systems. A more efficient, accurate method to calculate fragility surfaces is presented in the next section.

5.3.1 Fragility surfaces by stochastic reduced order models

A new, highly efficient and non-intrusive method based on stochastic reduced order models (SROM) [28] is proposed for calculating response statistics. The

stochastic reduced order model can be viewed as a smart Monte Carlo method. Like Monte Carlo, the method uses random samples of the seismic ground motion process to characterize the structural response. Unlike Monte-Carlo, which uses a large number N of samples at random, SROM uses only a small number of samples $\tilde{N} << N$ selected in an optimal way.

Our goal is to construct SROMs for the process $A(t)$ for each (m, r) and use them to calculate fragility surfaces. A stochastic reduced order model $\tilde{A}(t)$ for $A(t)$ is a stochastic process with $\tilde{N}$ samples $\{a_i(t),\ i = 1, ..., \tilde{N}\}$ of $A(t)$. Usually the samples of $\tilde{A}(t)$ are not equally likely and are weighed by some probabilities $\mathbf{p} = \{p_i \geq 0,\ i = 1, ..., \tilde{N}\}$ such that $\sum_{i=1}^{\tilde{N}} p_i = 1$. The pairs of samples and their probabilities $(a_i(t), p_i)$ define completely the probability law of $\tilde{A}(t)$.

To construct $\tilde{A}(t)$ we select sets of $\tilde{N}$ samples of $A(t)$ and select their corresponding probabilities $p_i,\ i = 1, ..., \tilde{N}$ such that the discrepancy between the probability laws of $A(t)$ and $\tilde{A}(t)$ is minimized. Consider the metric

$$\varphi(\mathbf{p}) = w_1\varphi_1(\mathbf{p}) + w_2\varphi_2(\mathbf{p}) + w_3\varphi_3(\mathbf{p}), \tag{5.10}$$

where $\varphi_1,\ \varphi_2$, and φ_3 are functions which account for the differences between the marginal distributions, the moments and the correlation functions of $A(t)$ and $\tilde{A}(t)$. The weights $\{w_i > 0,\ i = 1, 2, 3\}$ can be used to focus on certain properties of the two processes. For each set of $\tilde{N}$ samples we calculate an optimal probability vector $\mathbf{p^{opt}}$ of $\mathbf{p}$ by minimizing $\varphi(\mathbf{p})$, such that $p_i^{opt} > 0,\ i = 1, ..., \tilde{N}$

and $\sum_{i=1}^{\tilde{N}} p_i^{opt} = 1$. Functions $\varphi_k(\mathbf{p}),\ k = 1, 2, 3$ have the expressions

$$\varphi_1(\mathbf{p}) = \int_{-\infty}^{\infty} \int_0^{t_f} \left(\tilde{F}(x,t) - F(x,t) \right)^2 dt dx, \tag{5.11}$$

$$\varphi_2(\mathbf{p}) = \sum_{q=1}^{n_q} \int_0^{t_f} \left(\tilde{\mu}(t;q) - \mu(t;q) \right)^2 dt, \tag{5.12}$$

$$\varphi_3(\mathbf{p}) = \int_0^{t_f} \int_0^{t_f} \left(\tilde{c}(t,s) - c(t,s) \right)^2 dt ds, \tag{5.13}$$

where $\tilde{F}(x,t),\ F(x,t)$ are marginal distribution functions, $\tilde{\mu}(x,t),\ \mu(x,t)$ are moments and $\tilde{c}(t,s),\ c(t,s)$ are correlation functions for $\tilde{A}(t)$ and $A(t)$, respectively and n_q is the order of the higher moment considered. Functions $F(x,t),\ \mu(x,t)$ and $c(t,s)$ can be calculated from samples of $A(t)$ or directly from its distribution. Properties for the SROM $\tilde{A}(t)$ are estimated as follows

$$\tilde{F}(x,t) = \mathbb{P}\{\tilde{A}(t) \leq x\} = \sum_{i=1}^{\tilde{N}} p_i \mathbb{1}\{a_i(t) \leq x\} \tag{5.14}$$

$$\tilde{\mu}(t;q) = \mathbb{E}\left[\tilde{A}(t)^q\right] = \sum_{i=1}^{\tilde{N}} p_i a_i(t)^q \tag{5.15}$$

$$\tilde{c}(t,s) = \mathbb{E}\left[\tilde{A}(t)\tilde{A}(s)\right] = \sum_{i=1}^{\tilde{N}} p_i a_i(t) a_i(s). \tag{5.16}$$

The set of $\tilde{N}$ samples which provides the minimum value for the metric $\varphi(\mathbf{p^{opt}})$ defines the SROM $\tilde{A}(t)$. The range of $\tilde{A}(t)$ is suboptimal because we use a relatively small number of distinct sets of $\tilde{N}$ samples of $A(t)$ to select the samples for the SROM.

$$P_f(m,r) = \frac{1}{\tilde{N}} \sum_{i=1}^{\tilde{N}} p_i \mathbb{1}\{\max_{0 \leq t \leq t_f} |\tilde{x}_i(t)| > x_{cr}\} \tag{5.17}$$

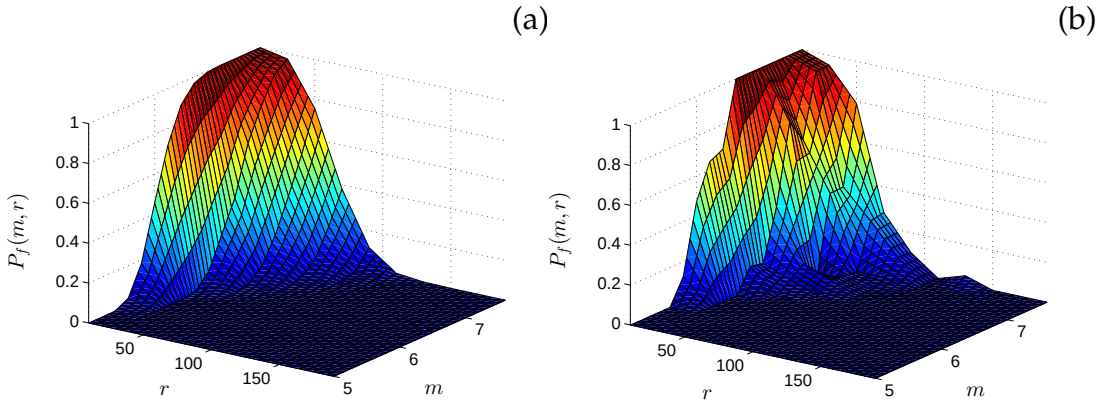

Figure 5.7: Fragility surface for a linear system obtained by (a) MC ($n = 1000/\text{cell}$) and (b) SROM ($\tilde{n} = 20/\text{cell}$)

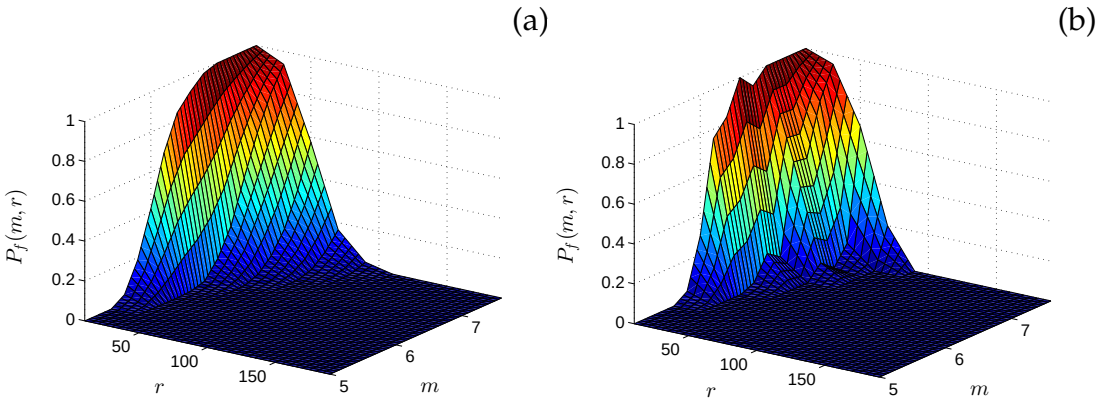

Figure 5.8: Fragility surface for a Bouc-Wen system obtained by (a) MC ($n = 1000/\text{cell}$) and (b) SROM ($\tilde{n} = 20/\text{cell}$)

5.3.2 Bi-variate log-normal model

Similar to the common approach of using a log-normal cumulative distribution function as a model for fragility curves, we propose a bi-variate log-normal cumulative distribution function as a model for fragility surfaces.

The bi-variate log-normal distribution function $F_{LN}(m, r; \mu_1, \sigma_1, \mu_2, \sigma_2, \rho)$ is completely defined by its five parameters $\{\mu_1, \sigma_1, \mu_2, \sigma_2, \rho\}$ and has the follow-

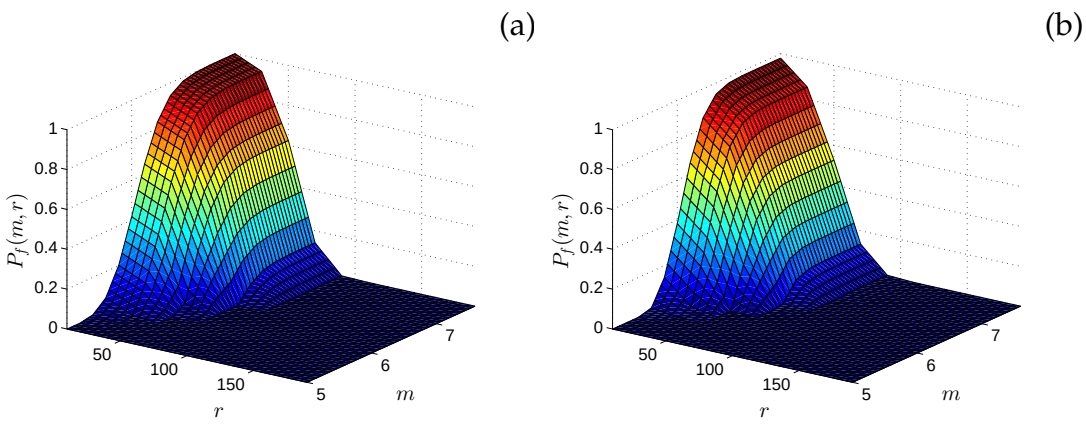

Figure 5.9: Bi-variate log-normal model for the fragility surface for a Bouc-Wen system obtained by (a) MC and (b) SROM

ing form

$$F_{LN}(m,r;\mu_1,\sigma_1,\mu_2,\sigma_2,\rho) = \int_0^m \int_0^r f_{LN}(\xi,\eta;\mu_1,\sigma_1,\mu_2,\sigma_2,\rho)d\xi d\eta, \tag{5.18}$$

where

$$f_{LN}(m,r) = \frac{1}{2\pi\sigma_1\sigma_2\sqrt{1-\rho^2}mr}\exp\left(-\frac{f'}{2(1-\rho^2)}\right) \tag{5.19}$$

$$f' = \left(\frac{\ln m-\mu_1}{\sigma_1}\right)^2 - 2\rho\left(\frac{\ln m-\mu_1}{\sigma_1}\right)\left(\frac{\ln r-\mu_2}{\sigma_2}\right) + \left(\frac{\ln r-\mu_2}{\sigma_2}\right)^2,$$

is the the two-dimensional probability density function for the log-normal distribution.

The fragility surface calculated in Eqs. (5.9) and (5.17) are used to estimate the values of the bi-variate log-normal distribution parameters. These parameters will define the parametric model in Eq.(5.18) for the fragility surface for any m and r. Figures 5.9 (a) and (b) show the parametric model for the fragility surfaces calculated for the Bouc-Wen system using MC and SROM methods and shown in Figure 5.8, respectively.

Table 5.1 summarizes the parameters estimated for the fragility surfaces calculated for the Bouc-Wen system shown in Figure 5.9. The two surfaces fitted to

Table 5.1: Parameters for the parametric fragility surface for the Bouc-Wen system

Method	μ_1	σ_1	μ_2	σ_2	ρ
MC	1.803	0.055	4.979	0.103	-0.997
SROM	1.805	0.046	5.003	0.122	-0.999

the MC and SROM data are essentially the same, since the parameters estimated for the two differ by at most 16% and the mean average error between the two surfaces is under 5%.

5.4 Life-cycle Analysis

Life-cycle analysis assesses the impacts of the seismic catastrophe events on different aspects of a structure during its entire life, usually defined as a large time window τ. In this section we propose a methodology for estimating seismic-performance metrics of structures, such as damage, downtime and cost. Downtime is important for insurance companies since they cover, in addition to building/content damages, losses caused by business interruptions. Our main goal is to estimate distributions rather than just mean values for these metrics to characterize structural performance and resilience since they provide superior resolution. For example, if the repair costs for two structures designed for the same seismic loads have the same mean but different distributions, the performances of these structures are indistinguishable based on the average repair cost, but can differ significantly if based on the probability that repair cost exceeds a specified value [34].

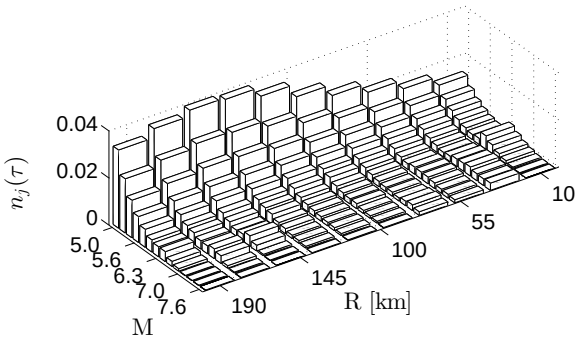

Figure 5.10: Seismic activity matrix for Los Angeles

The United States Geological Survey provides mean annual rates of occurrence $\lambda_{m,r}$ for earthquakes with parameters (m, r), at each site in the United States. We assume that the number of seismic events $N(\tau)$ during the life-time of a structure has a Poisson distribution with mean $\lambda = \sum_{\forall(m,r)} \lambda_{m,r}$ in τ years. We also define the probability of occurrence of earthquakes with parameters (m, r) as $p_{m,r} = \lambda_{m,r}/\lambda$. The graphical representation of $p_{m,r}$ in coordinates (m, r) is a two-dimensional histogram and we call it the seismic activity matrix. Figure 5.10 shows an example of a seismic activity matrix for a site in Los Angeles. By thinning the Poisson process $N(\tau)$, the number of seismic events with parameters (m, r) is $N_{m,r}(\tau) = p_{m,r}\lambda$. Figures 5.14 (a) and (b) show two samples of the number of events at a Los Angeles site for $\tau = 100\ years$ and $\lambda = 0.6668$ and Figures 5.14 (c) and (d) show the events located on the time scale. Note that the inter-arrival times between consecutive events are exponentially distributed with mean $1/\lambda$.

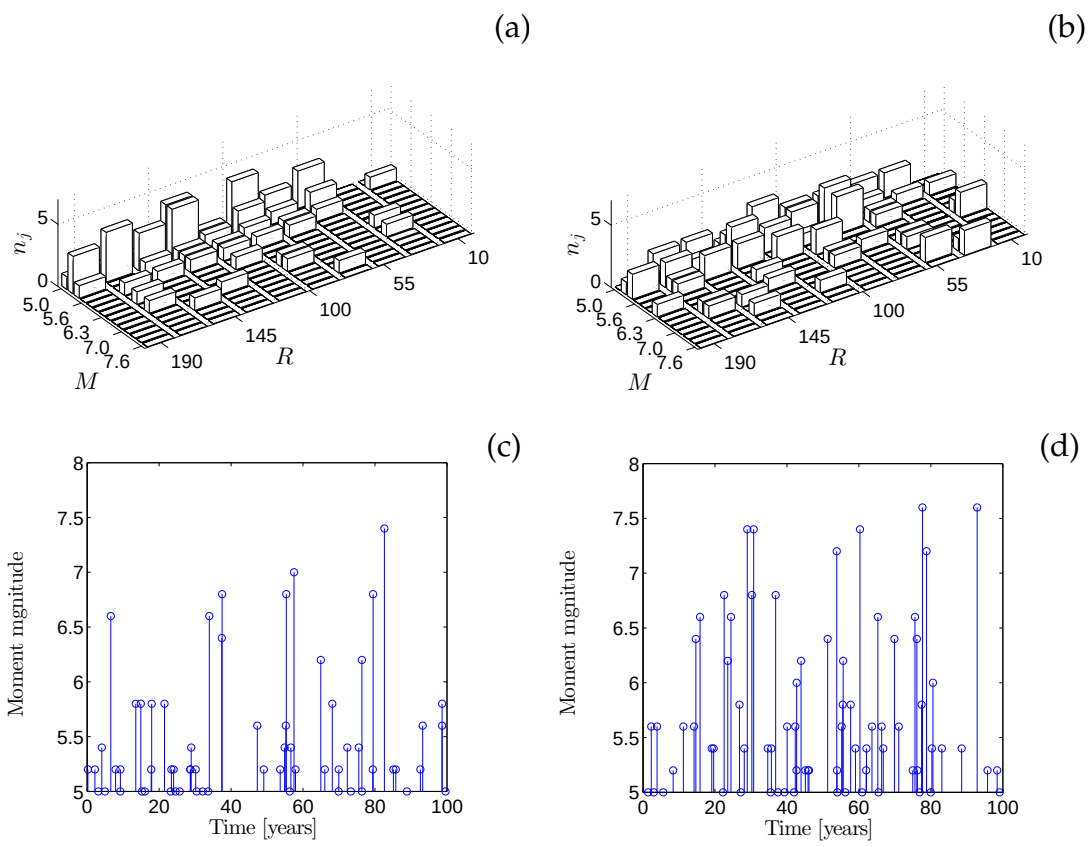

Figure 5.11: Life-cycle events by (a), (b) the samples of the number of records with parameters (m, r) for a life time $\tau = 100\ years$ and (c), (d) the corresponding magnitudes on the time scale.

5.4.1 Damage Model Description

We define the damage state $W(t)$ of a structure at time t to take values within range $0 \leq W(t) \leq 1$, zero representing no-damage state and one representing failure. The damage function $W(t)$ is defined as a regenerative process with the following form

$$W(t) = \max\left(0, d_0 + \sum_{\forall(m,r)} \sum_{i=1}^{N_{m,r}(t)} D_{m,r}(t_i) - \int_0^t \xi(s)ds\right), \tag{5.20}$$

where d_0 is the initial damage, $N_{m,r}(t)$ is the number of seismic events with parameters (m, r) up to time t, $D_{m,r}(t_i)$ is the level of damage produced by the

event i-th (m, r) event at time t_i and $\xi(s)$ is the damage-recovery rate. For our framework we assume that damage $D_{m,r}(t)$ generated by an earthquake with parameters (m, r) at time t to a structure that is already at damage state $W(t)$ is

$$D_{m,r} = \eta_D P_f^d(m, r; W(t)), \tag{5.21}$$

where $0 \leq \eta_D \leq 1$ is a constant parameter and $P_f^d(m, r; W(t))$ is the fragility surface for a structure at damage state $W(t)$. Fragility surfaces $P_f(m, r)$ calculated in the previous section in Eqs. (5.9) and (5.17) assume structural properties at full capacity, i.e. $W(t) = 0,\ \forall t > 0$. However, fragility surfaces change for damaged structures. We propose two parametric models for the fragility surfaces $P_f^d(m, r; W(t))$ under damage level $W(t)$ at time $0 \leq t \leq \tau$.

Model 1 The first model for the fragility surface for a structure under the damage level $W(t)$ is

$$P_f^d(m, r; W(t)) = \left[P_f(m, r) + (1 - P_f(m, r)) \left(1 - e^{-\psi W(t)}\right)\right]^{1 - W(t)^\eta}, \tag{5.22}$$

where $\psi > 0$ and $\eta > 0$ are some constant parameters. Figure 5.12 shows fragility surfaces, under Model 1 with parameters $\psi = 0.30$ and $\eta = 1$, for a damaged structure under three level of damage of $20\%,\ 50\%$ and 80%, respectively.

Model 2 The second model is also a parametric model of the form

$$P_f^d(m, r; W(t)) = F_{LN}(m, r; \Theta(\Psi))^{1 - W(t)^\eta} \tag{5.23}$$

(a) (b) (c)

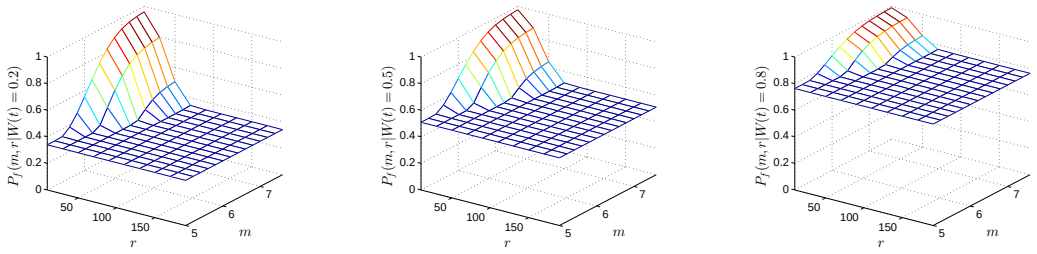

Figure 5.12: Evolution of fragility surfaces with increasing demand: (a) $W(t) = 0.2$, (b) $W(t) = 0.5$, (c) $W(t) = 0.8$.

where

$$\Theta(\Psi) = \begin{pmatrix} (1 - \psi_1 W(t))\mu_1 \\ \sigma_1^{1-\psi_2 W(t)} \\ (1 - \psi_3 W(t))\mu_2 \\ \sigma_2^{1-\psi_4 W(t)} \\ \rho^{\psi_5} \end{pmatrix}, \tag{5.24}$$

where $W(t)$ is the current damage state, F is the bi-variate log-normal cumulative distribution function with parameters $(\mu_1, \sigma_1, \mu_2, \sigma_2, \rho)$ estimated in the previous section and $\Psi = \{\psi_i, i = 0, ..., 5\}$ is a vector of scalar parameters. Parameters for both models are usually estimated from historical data recorded at past damaging events for various types of structures. Figure 5.13 shows fragility surfaces, under Model 2 with parameters $\psi_1 = \psi_2 = 0.15$, $\psi_3 = 0.30$, $\psi_4 = 0.93$, $\psi_5 = 1$ and $\eta = 1$ for a damaged structure under three level of damage of 20%, 50% and 80%, respectively.

Figure 5.14 (a) shows a sample of the damage process $W(t)$ for which we assume (1) Model 2 for $P_f^d(m, r; W(t))$ as defined previously, (2) $\eta_D = 0.7$, (3) no-damage state $W(t) = 0$ can be reached from any damage state $W(t) < 1$ and

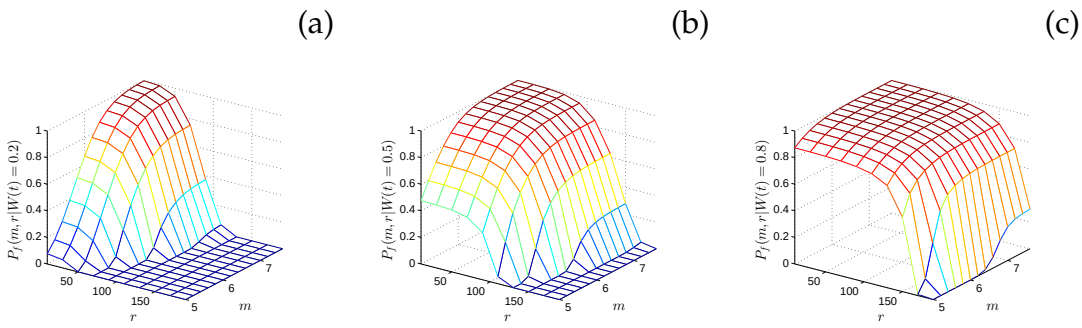

Figure 5.13: Evolution of fragility surfaces with increasing demand: (a) $W(t) = 0.2$, (b) $W(t) = 0.5$, (c) $W(t) = 0.8$.

(4) a constant damage-recovery rate of $\xi = 0.25$, that is, the full damage state can be completely recovered in 4 years. For a clearer view, Figure 5.14 (b) shows a zoomed-in image of part of the sample of $W(t)$ in part (a) of the figure.

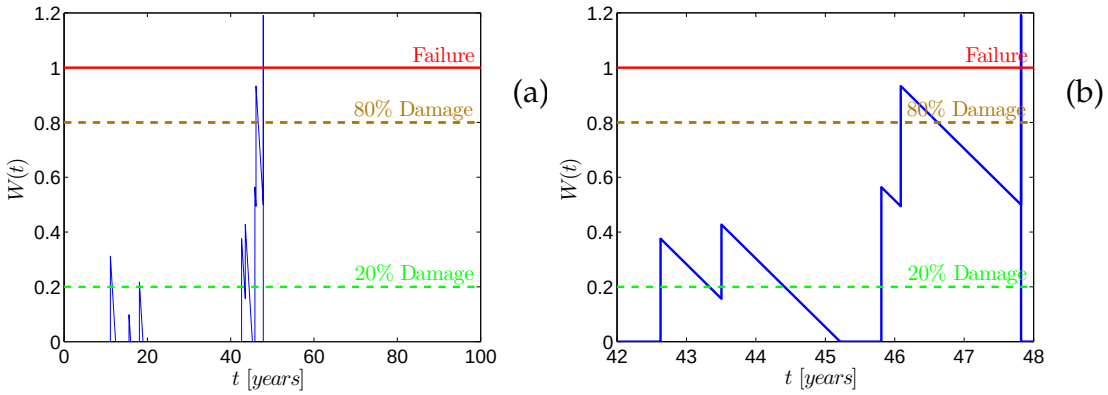

Figure 5.14: Sample of $W(t)$ (a) for $\tau = 100$ years and (b) close-up on part of the sample in (a).

We define three damage states of interest for the current framework (1) low damage state for $W(t) < 0.2$, at which we assume that the building is functional, (2) moderate damage state for $0.2 \leq W(t) < 0.8$ and (3) severe damage state for $W(t) \geq 0.8$. Note that once failure is reached, no recovery is allowed for that structure. According to the three damage states defined, downtime is calculated

as the time interval during which the structure is in moderate or severe damage states. Downtime is an important parameter for insurance markets since, it represents the business-interruption time for that structure, which could be covered by insurance.

Formally, we can define the time interval in which the structure is in a damage state larger than a value $w \in (0, 1)$ as $\Delta T_w = [t_i, t_j]$ for which $W(t) \geq w,\ \forall t \in [t_i, t_j]$ and $W(t_i - \epsilon),\ W(t_j + \epsilon) < w,\ \forall \epsilon > 0$. For example, $\Delta T_{0.2}$ and $\Delta T_{0.8}$ represent the time intervals in which the structure is under moderate and severe damage, respectively. Probability distributions of $\Delta T_{0.2}$ and $\Delta T_{0.8}$ are calculated by Monte-Carlo simulation. Since we assumed that the activities in the building are interrupted for $w > 0.2$, then $\Delta T_{0.2}$ is also the downtime.

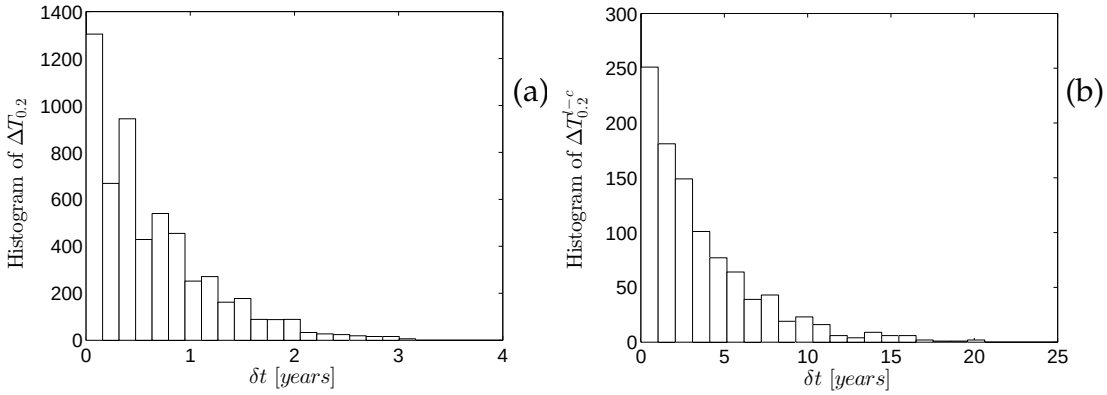

Figure 5.15: Histograms for (a) $\Delta T_{0.2}$ and (b) life-cycle times $\Delta T_{0.2}^{l-c}$.

Figure 5.15 shows histograms of (a) downtime $\Delta T_{0.2}$ and (b) life-cycle downtime $\Delta T_{0.2}^{l-c}$, that is, the downtime of a structure during its entire life-time τ. Figure 5.16 shows the tail distributions for (a) ΔT_w and (b) ΔT_w^{l-c}, for $w = 0.2,\ 0.8$, that is, the probability of exceeding a value δt, $\mathbb{P}(\Delta T_w > \delta t)$ and $\mathbb{P}(\Delta T_w^{l-c} > \delta t)$, respectively.

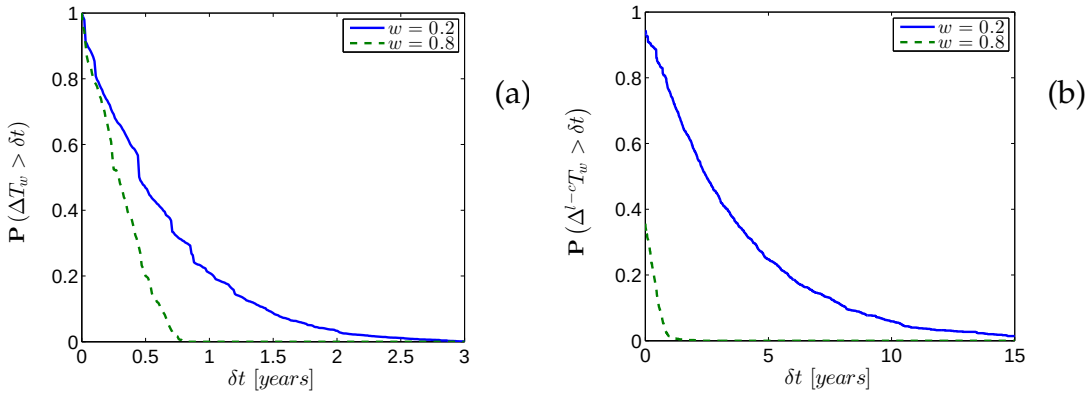

Figure 5.16: Tail distributions for (a) $\Delta T_w,\ w = 0.2,\ 0.8$ and (b) life-cycle times $\Delta T_w^{l-c},\ w = 0.2,\ 0.8$.

5.4.2 Cost Model

For the cost associated with loss due to earthquakes we consider just the cost of repairs, goods lost and insurance claims associated with material losses, down-time and casualties. The cost $C_{m,r}$ associated with a seismic event with parameters (m, r) is related to the corresponding damage $D_{m,r}$. In order to show the importance of considering the cost distribution rather than the mean values, we assume two cost functions for $C_{m,r}$, that follow a Gamma distribution with the same mean $D_{m,r}$ but different parameters $a_i, b_i > 0,\ i = 1, 2$. The cost generated by an event with (m, r) is governed by the probability density function

$$f_{C,i}(x; m, r) = \frac{1}{\Gamma(a_i) b_i^{a_i}} x^{a_i - 1} e^{-\frac{x}{b_i}}, \tag{5.25}$$

where Γ is the Gamma function. The two sets of parameters defining the distribution of cost $C_{m,r}$ are associated with two values of the coefficient of variation $c_{v,i},\ i = 1, 2$. From the properties of Gamma distribution we can find the values of the two parameters as $a_i = 1/c_{v,i}^2$ and $b_i(m, r) = D_{m,r}/a_i$. Figure 5.17 shows the two probability density functions for the cost random variables $C_{m,r}$ with mean $D_{m,r} = 0.5$, associated to $c_{v,1} = 0.5$ and $c_{v,2} = 2$, respectively. The two

distributions have the same mean, but are essentially different.

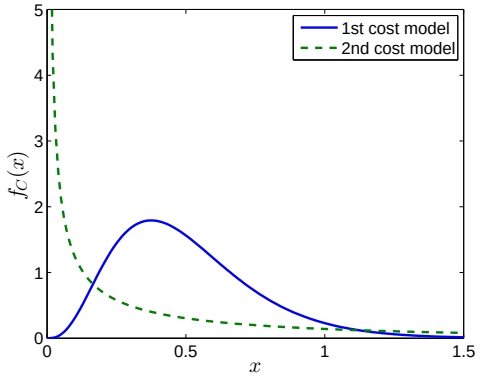

Figure 5.17: Probability density functions for the two models for $C_{m,r}$ with the same mean $D_{m,r} = 0.5$, and coefficients of variation $c_{v,1} = 0.5$ and $c_{v,2} = 2$.

The life-cycle cost $U(\tau)$ will be calculated as the summation of the costs generated by each individual event during the life-time τ of the structure

$$U(\tau) = \sum_{\forall(m,r)} \sum_{i=1}^{N_{m,r}(\tau)} C_{(m,r),i}, \tag{5.26}$$

where $C_{(m,r),i}$ is the cost associated with the i-th event with parameters (m, r). Figure 5.18 shows the tail distribution for the life-cycle cost, that is, the probability $\mathbb{P}(U(\tau) > u)$ that the life-cycle cost $U(\tau)$ exceeds a value u.

Even though the cost functions for the events $C_{m,r}$ are indistinguishable with respect to their means, the tail distributions differ significantly. The second model corresponding to a coefficient of variation $c_{v,2} = 2$ leads to a life-cycle cost with heavier tails. Tail risk is an important instrument for reinsurance markets which cover the claims of highly unlikely events which generate very large costs.

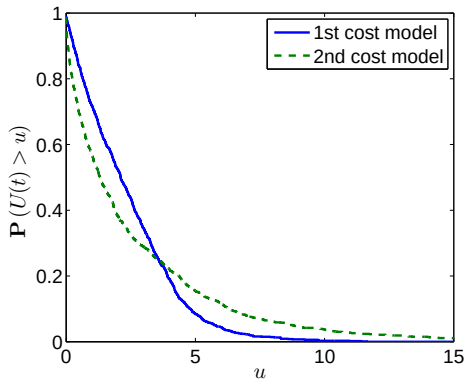

Figure 5.18: Tail distribution function for the life-cycle cost $\mathbb{P}(U(t) > u)$.

5.5 Conclusions

This chapter presents a complete framework for the evaluation of seismic performance of structures. This goal was achieved through (1) accurate fragility analyses of structural systems and (2) probability distribution estimates for metrics which describe structural performance. The ground motion process is assumed to be a non-Gaussian stochastic process with second order moment properties given by a seismological model in the form of a spectral density function of moment magnitude m and source-to site distance r. A t-student distribution is chosen for the ground motion process to account for high peaks. Fragility surfaces in coordinates (m, r) consistent with the ground-motion model are proposed in the current analysis. Stochastic reduced order models are used as an efficient way to calculate fragility surfaces and results match well fragility surfaces produced by Monte Carlo. A bi-variate log-normal distribution is proposed as a fucntional form for fragility surfaces, similar to the model addopted by ATC-58 for fragility curves.

The second part of the paper develops probabilistic models for damage and

cost functions used to evaluate life-cycle cost of structural systems. A regenerative model is proposed for damage under a set of assumptions and parametric models for fragility surfaces for damaged structures are proposed. Life-cycle estimates are calculated by Monte Carlo simulations of seismic hazard scenarios for the entire life of the structure. It is shown that estimating the entire distribution for evaluating seismic performance of structures provides valuable information which could otherwise be omitted. Two different cost models could lead to comparable average values of the life-cost but have considerable discrepancies in their tails.

BIBLIOGRAPHY

[1] N. Abrahamson, G. Atkinson, D. Boore, Y. Bozorgnia, K. Campbell, B. Chiou, I.M. Idriss, W. Silva, and R. Youngs. Comparisons of the nga ground-motion rzelations. *Earthquake Spectra*, 24(1):45–66, 2008.

[2] N.A. Abrahamson. State of the practice of the seismic hazard evaluation. *GeoEng 2000*, (1):659–685, 2000.

[3] ATC-58 Applied Technology Council. Seismic performance assessment of buildings - methodology. *Federal Emergency Management Agency*, 1, 2012.

[4] J.W. Baker. Probabilistic structural response assessment using vector-valued intensity measures. *Earthquake Engineering and Structural Dynamics*, 36:1861–1883, 2007.

[5] J.W. Baker. Conditional mean spectrum: Tool for ground motion selection. *Journal of Structural Engineering*, 137(3):322–331, 2011.

[6] J.W. Baker. Efficient analytical fragility function fitting using dynamic structural analysis. *Earthquake Spectra*, page (in print), 2014.

[7] J.W. Baker and C.A. Cornell. A vector-valued ground motion intensity measure consisting of spectral acceleration and epsilon. *Earthquake Engineering and Structural Dynamics*, 34:1193–1217, 2005.

[8] J.W. Baker and C.A. Cornell. Correlation of response spectral values for multicomponent ground motions. *Bulletin of the Seismological Society of America*, 96(1):215–227, 2006.

[9] J.W. Baker and C.A. Cornell. Spectral shape, epsilon and record selection. *Earthquake Engineering and Structural Dynamics*, 35:1077–1095, 2006.

[10] J.W. Baker and N. Jayaram. Correlation of spectral acceleration values from nga ground motion models. *Earthquake Spectra*, 24(1):299–317, 2008.

[11] P. Bazzurro and C.A. Cornell. Disaggregation of seismic hazard. *Bulletin of the Seismological Society of America*, 89(2):501–520, 1999.

[12] K.W. Campbell and Y. Bozorgnia. Nga ground motion model for the geometric mean horizontal component of pga, pgv, pgd and 5% damped linear

elastic response spectra for periods ranging from 0.01 to 10 s. *Earthquake Spectra*, 24(1):139–171, 2008.

[13] A. Chatterjee. An introduction to the proper orthogonal decomposition. *Current Science*, 78(7):808–817, 2000.

[14] Y.S. Choun and A.S. Elnashai. A simplified framework for probabilistic earthquake loss estimation. *Probabilistic Engineering Mechanics*, 25:355–364, 2010.

[15] J. Douglas. Strong-motion records selection for structural testing. In *First European Conference on Earthquake Engineering and Seismology*, Geneva, Switzerland, September 2006.

[16] J. Douglas and H. Aochi. A survey of techniques for predicting earthquake ground motions for engineering purposes. *Surveys in Geophysics*, 29:187–220, 2008.

[17] B.R. Ellingwood, O.C. Celik, and Kinali K. Fragility assessment of building structural systems in mid-america. *Earthquake Engineering and Structural Dynamics*, 36:1935–1952, 2007.

[18] K. M. Foster, B. Halldorsson, Russell A. G., and M. C. Chapman. Calibration of the specific barrier model to the nga dataset. *Seismological Research Letters*, 83(3):566–574, 2012.

[19] A.D. Frankel, M.D. Petersen, C.S. Mueller, K.M. Haller, R.L. Wheeler, E.V. Levendecker, R.L. Wesson, S.C. Harmsen, C.H. Cramer, D.M. Perkins, and K.S. Rukstales. Documentation for the 2002 update of the national seismic hazard maps. *USGS Open-File Report 02-420*, 2002.

[20] F.N. Fritsch and R.E. Carlson. Monotone piecewise cubic interpolation. *SIAM Journal on Numerical Analysis*, 17(2):238–246, 1980.

[21] D.L. Garcia and T.T. Soong. Sliding fragility of block-type non-structural components. part 2: Restrained components. *Earthquake Engineering and Structural Dynamics*, 32:131–149, 2003.

[22] P. Gardoni, A.D. Kiureghian, and Mosalam K.M. Probabilistic capacity models and fragility estimates for reinforced concrete columns based on experimental observations. *Journal of Engineering Mechanics*, 128(10):1024–1038, 2002.

[23] P. Gardoni and D. Rosowski. Seismic fragility increment functions for deteriorating reinforced concrete bridges. *Structure and Infrastructure Engineering*, 1:1–11, 2009.

[24] P. Gehl, S. Serigne, and D. Seyedi. Developing fragility surfaces for more accurate seismic vulnerability assessment of masonry buildings. *Proceedings of the Conference on Computational Methods in Structural Methods in Structural Dynamics and Earthquake Engineering, Corfu, Greece*, 2011.

[25] A. Gelman, J.B. Carlin, H.S. Stern, and D.B Rubin. *Bayesian data analysis*. Chapman and Hall CRC, Florida, USA, 2nd edition, 2003.

[26] C.A. Goulet, C.B. Haselton, J. Mitrani-Reiser, J.L. Beck, G.G. Deierlein, K.A. Porter, and J.P. Stewart. Assessment of probability of collapse and design for collapse safety. *Earthquake Engineering and Structural Dynamics*, 36:19731997, 2007.

[27] M. Grigoriu. *Applied non-Gaussian processes: examples, theory, simulation, linear random vibration, and MATLAB solutions*. PTR Prentice Hall, New Jersey, 1995.

[28] M. Grigoriu. Reduced order models for random functions. application to stochastic problems. *Applied Mathematical Modelling*, 33:161–175, 2009.

[29] M. Grigoriu. Linear random vibration by stochastic reduced order models. *International Journal for Numerical Methods in Engineering*, 82:1537–1559, 2010.

[30] M. Grigoriu. To scale or not to scale seismic ground accceleration records. *Journal of Engineering Mechanics*, 137(4):284–293, 2011.

[31] M. Grigoriu. A method for solving stochastic equations by reduced order models and local approximations. *Journal of Computational Physics*, 231(19):64956513, 2012.

[32] M. Grigoriu. A new method for solving random vibration problems. *Proceedings of The Eleventh International Conference on Computational Structural Technology*, 2012.

[33] M. Grigoriu. *Stochastic systems. Uncertainty quantification and propagation.* Springer-Verlag Ltd, London, UK, 2012.

[34] M. Grigoriu, A. Radu, and C. Kafali. Seismic performance by fragility surfaces. *Proceedings of the 10th U.S. National Conference on Earthquake Engineering*, 2014.

[35] M. Grigoriu, S.E. Ruiz, and E. Rosenblueth. The mexico earthquake of september 19, 1985 - nonstationary models of seismic ground acceleration. *Journal of Computational Physics*, 4(3):551–568, 1988.

[36] Baker Research Group. A computationally efficient ground motion selection algorithm for matching a target response spectrum mean and variance. last checked on 02/12/2013. *URL http://www.stanford.edu/b̃akerjw/gm_selection.html*.

[37] B. Halldorsson and A.S. Papageorgiou. Calibration of the specific barrier model to earthquake of different tectonic regions. *Bulletin of Seismological Society of America*, 95(4):1276–1300, 2005.

[38] B. Halldorsson and A.S. Papageorgiou. Variations of the specific barrier model - part i: effect of subevent size distributions. *Bulletin of Earthquake Engineering*, 10:1299–1319, 2012.

[39] B. Halldorsson and A.S. Papageorgiou. Variations of the specific barrier model - part ii: effect of isochron distributions. *Bulletin of Earthquake Engineering*, 10:1321–1337, 2012.

[40] Hazus-MH. Multi-hazard loss estimation methodology: earthquake model. *Technical Manual, Hazus-MH MR5*, Department of Homeland Security, Federal Emergency Management Agency, Washington, DC.

[41] F. Jalayer, P. Franchin, and P.E. Pinto. A scalar damage measure for seismic reliability analysis of rc frames. *Earthquake Engineering and Structural Dynamics*, 36:2059–2079, 2007.

[42] N. Jayaram, T. Lin, and J.W. Baker. A computationally efficient ground-motion selection algorithm for matching a target response spectrum mean and variance. *Earthquake Spectra*, 27(3):797–815, 2011.

[43] C. Kafali. System performance under multihazard environment. *PhD Thesis*, 2008.

[44] C. Kafali and M. Grigoriu. Seismic fragility analysis: Application to simple

linear and nonlinear systems. *Earthquake Engineering and Structural Dynamics*, 36(13):1885–1900, 2010.

[45] P.S. Koutsourelakis. Assessing structural vulnerability against earthquakes using multi-dimensional fragility surfaces: A bayesian framework. *Probabilistic Engineering Mechanics*, 25:49–60, 2010.

[46] S. Kullback and R.A. Leibler. On information and sufficiency. *The Annals of Mathematical Statistics*, 22(1):79–86, 1951.

[47] L. Le Cam. On some assymptotic properties of maximum likelihood estimates and related bayesian estimates. *University of California Publications in Statistics*, 1(11):238–246, 1953.

[48] J Li and J. Chen. *Stochastic dynamics of structures*. John Wiley Sons, Singapore, 2009.

[49] A. Liel, C.B. Haselton, G.G. Deierlein, and J.W. Baker. Incorporating modeling uncertainties in the assessment of seismic collapse risk of buildings. *Structural Safety*, 31:197–211, 2009.

[50] T. Lin, C.B. Haselton, and J.W. Baker. Conditional spectrum-based ground motion selection. part i: Hazard consistency for risk-based assessments. *Earthquake Engineering and Structural Dynamics*, 42(12):1847–1865, 2013.

[51] T. Lin, C.B. Haselton, and J.W. Baker. Conditional spectrum-based ground motion selection. part ii: Intensity-based assessments and evaluation of alternative target spectra. *Earthquake Engineering and Structural Dynamics*, 42(12):1867–1884, 2013.

[52] T. Lin, C.H. Stephen, J.W. Baker, and N. Luco. Conditional spectrum computation incorporating multiple causal earthquakes and ground-motion prediction models. *Bulletin of the Seismological Society of America*, 103(2A):1103–1116, 2013.

[53] R. K. McGuire. Probabilistic seismic hazard analysis and design earthquakes: closing the loop. *Bulletin of the Seismological Society of America*, 85(5):1275–1284, 1995.

[54] B. Ozer and S. Akkar. A procedure on ground motion selection and scaling for nonlinear response of simple structural systems. *Earthquake Engineering and Structural Dynamics*, 41:1693–1707, 2012.

[55] A.S. Papageorgiou and K. Aki. A specific barrier model for the quantitative description of inhomoeneous faulting and the prediction of strong ground motion. applications of the model. *Bulletin of Seismological Society of America*, 73(4):953–978, 1983.

[56] A.S. Papageorgiou and K. Aki. A specific barrier model for the quantitative description of inhomoeneous faulting and the prediction of strong ground motion. description of the model. *Bulletin of Seismological Society of America*, 73(3):693–722, 1983.

[57] K. Porter, R. Kennedy, and R. Bachman. Developing fragility functions for building components for atc-58. *Applied Technology Council*, 2006.

[58] G. Pousse, L.F. Bonilla, F. Cotton, and L. Margerin. Nonstationary stochastic simulation of strong ground motion time histories including natural variability: Application to the k-net japanese database. *Bulletin of the Seismological Society of America*, 96(6):2103–2117, 2006.

[59] A. Radu and M. Grigoriu. Bayesian updating of the ground motion specific barrier model. *Proceedings of the 11th International Conference on Structural Safety & Reliability*, 2013.

[60] A. Radu and M. Grigoriu. A site-specific seismological model within a bayesian updating framework. *Proceedings of the 10th International Conference on Urban Earthquake Engineering*, 2013.

[61] A. Radu and M. Grigoriu. An efficient apoproach on dynamic-response analyses for structural systems. *Proceedings of the 10th U.S. National Conference on Earthquake Engineering*, 2014.

[62] A. Radu and M. Grigoriu. A site-specific seismological model for seismic hazard. *Bulletin of the Seismological Society of America*, 104(6):(in print), 2014.

[63] S. Rezaeian and A.D. Kiureghian. Simulation of synthetic ground motions for specified earthquake and site characteristics. *Earthquake Engineering and Structural Dynamics*, 39(10):1155–1180, 2010.

[64] M. Sasani, Kiureghian A.D., and Bertero V.V. Seismic fragility of short period reinforced concrete structural walls under near-source ground motions. *Structural Safety*, 24:123–138, 2002.

[65] D.M. Seyedi, P. Gehl, J. Douglas, L. Davenne, Mezher N., and Ghavamian

S. Development of seismic fragility surfaces for reinforced concrete buildings by means of nonlinear time-history analysis. *Earthquake Engineering and Structural Dynamics*, 39:91–108, 2009.

[66] M. Shinozuka, M.Q. Feng, H. Kim, T. Uzawa, and T. Ueda. Statistical analysis of fragility curves. *Technical report MCEER: 106-E-7.3.5 and 106-E-7.6*, 2001.

[67] M. Shinozuka, J. Lee, and T Naganuma. Statistical analysis of fragility curves. *Journal of Engineering Mechanics (ASCE)*, 126(12):1224–1231, 2000.

[68] A. Singhal and A.S. Kiremidjian. Method for probabilistic evaluation of seismic structural damage. *Journal of Structural Engineering (ASCE)*, 122(12):1459–1467, 1996.

[69] T.T. Soong and M. Grigoriu. *Random vibration of mechanical and structural systems*. PTR Prentice - Hall, Inc, New Jersey, USA, 1993.

[70] P. Tothong and N. Luco. Probabilistic seismic demand analysis using advanced ground motion intensity measures. *Earthquake Engineering and Structural Dynamics*, 36:1837–1860, 2007.

[71] M. D. Trifunac. A method for synthesizing realistic strong ground moitons. *Bulletin of the Seismological Society of America*, 61(6):1739–1753, 1971.

[72] USGS. U.s. geological survey: 2008 interactive deaggregations. last checked on 02/12/2013. *URL https://geohazards.usgs.gov/deaggint/2008/*.

[73] D. Vamvatsikos and C.A. Cornell. Incremental dynamic analysis. *Earthquake Engineering and Structural Dynamics*, 31:491–514, 2002.

[74] J. Warner, M. Grigoriu, and W. Aquino. Stochastic reduced order models for random vectors. applications to random eigenvalue problems. *Probabilistic Engineering Mechanics*, 31:1–11, 2013.

[75] F. Zareian and H. Krawinkler. Assessment of probability of collapse and design for collapse safety. *Earthquake Engineering and Structural Dynamics*, 36:1901–1914, 2007.

[76] I. Zentner and F. Poirion. Enrichment of seismic ground motions databases using karhunen-loeve expasion. *Earthquake Engineering and Structural Dynamics*, 2012.

[77] A Zerva. *Spatial variation of seismic ground motions: Modeling and engineering applications*. Advances in engineering. CRC Press - Taylor Francis Group, LLC, 2009.